VELOCITY STUDIES IN THE DEEPWATER GULF OF MEXICO:

KEATHLEY CANYON AND WALKER RIDGE AREAS

A Dissertation Presented to

the Faculty of the Department of Earth and Atmospheric Sciences

University of Houston

In Partial Fulfillment

of the Requirements for the Degree

Doctor of Philosophy

By

Sharon Cornelius

May 2017

VELOCITY STUDIES IN THE DEEPWATER GULF OF MEXICO:

KEATHLEY CANYON AND WALKER RIDGE AREAS

Sharon Cornelius

APPROVED:

Dr. John P. Castagna, Chairman

Dr. Hua-wei Zhou, Department Chairman

Dr. Paul Mann

Dr. Fred Hilterman

Dr. Pete A. Emmet

Dr. Dan E. Wells, Dean,
College of Natural Sciences and Mathematics

ACKNOWLEDGEMENTS

My special thanks to Dr. John P. Castagna, Ph.D., for his guidance, time, and technical support throughout this endeavor, to Dr. Pete Emmet, Ph.D., for the many months he worked with me as together we built the 3D velocity model, and to Dr. Paul Mann, Ph.D., for his advice and access to the CBTH facilities and computer software. I especially wish to thank Dynamic Data Services for the use of their high-resolution seismic data, without which this academic study would not have been possible. Thanks also to Dr. Fred Hilterman for his very helpful advice. I would like to acknowledge IHS and CGG for their support of Kingdom and VelPro software licenses, respectively, at the University of Houston, and Neuralog for their software license donation specifically for this study. I wish to thank Maurice Slot, the creator of VelPro software, for checking the velocity model for technical accuracy. Another special thank you to Muhammad Nawaz Bugti for plotting the geothermal-gradient contours in Petrel.

VELOCITY STUDIES IN THE DEEPWATER GULF OF MEXICO:

KEATHLEY CANYON AND WALKER RIDGE AREAS

An Abstract of a Dissertation

Presented to

the Faculty of the Department of Earth and Atmospheric Sciences

University of Houston

In Partial Fulfillment

of the Requirements for the Degree

Doctor of Philosophy

By

Sharon Cornelius

May 2017

ABSTRACT

Two different, yet related, velocity studies were undertaken in and around the Keathley Canyon and Walker Ridge areas of the Gulf of Mexico. The first is a compilation of wellbore-salt-body interval velocities (V_{int}) from 55 wells exhibiting interval compressional-wave velocity variation from 13,966 ft/s to 18,535 ft/s with mean velocity of 14,920 ft/s and a standard deviation of 726 ft/s. The velocities vary significantly with latitude. Five different V_{int} zones have been identified with each having specific-associated mineralogies within a latitude range. In the mid-latitude zones, sylvite and small amounts of clastics, with traces of both anhydrite and gypsum, are found within the salt, yielding salt V_{int} variation from 14,388 ft/s to 14,965 ft/s. The salt V_{int} in the southern limits of the study area is higher than 15,000 ft/s and associated with more gypsum. The northern-most wells are anhydrite-rich and exhibit the highest velocities. The V_{int} are relatively uncorrelated to and insensitive to factors such as wellbore temperature, depth, and pressure. Composite medium modeling of the salt-body compositions shows that various mineral and lithologic inclusions within the salt body can explain the observed velocity variations.

The second study is a 3D velocity model constructed using high resolution 2D seismic data with 15 km offsets and 22 seconds (40 km or 130,000 ft) of record, constrained by sonic logs from 94 wells, 34 VSP or borehole seismic velocity surveys, and 38 calculated time versus depth tables derived from other borehole data. All forms of sonic information were transformed into V_{int} and loaded into the CGG VelPro velocity-modeling application. Comparison of the resultant 3D velocity model with available constraints shows that regional geological trends expressed in

the model faithfully reproduce the observed borehole V_{int} profiles at 18 locations where the seismic velocity control is in close proximity to measured borehole-velocity data. Zones of over-pressure and of Cenozoic limestone are discernible within the velocity model. The resultant 3D "cube" of V_{int} values covering Keathley Canyon, Walker Ridge, and a portion of Green Canyon evidences distinct details due to well control.

CONTENTS

1 Introduction

2 Latitudinal variation of salt-body interval velocities in the deepwater Gulf of Mexico: Keathley Canyon and Walker Ridge areas

LIST OF FIGURES

Keathley Canyon frontal ramp and the en echelon folds and faults along the Walker Ridge-Atwater Valley lateral ramp, prior to the Middle Miocene.

Figure 2.8b: shows the proposed direction of salt flow as it moves basinward over sediments deposited from NW to SE as suggested by Fort and Brun (2012). Base topographic map from GIS culture in 2014.

Figure 2.9: Seismic interval velocity vs. depth in feet for strike line 2800. Depth axis is from 0 to 70,000 ft and Vint from 5000 to 22,000 ft/s. Note that this seismic line crosses the Sigsbee Escarpment twice: once on the SW end and again on the NE end.

Figure 2.10a: Thrust advance of a salt canopy. During the Pliocene the salt may have advanced by extrusion, and if it did so, it moved basinward 4.2 miles or 6.8 km over 2 Ma.

Figure 2.10b: SEGY display of a walkaway VSP over Mad Dog Field along depositional dip of the Wilcox formation (NW to SE). The field is on the edge of the Sigsbee Escarpment. This image is truncated at 30,000 feet vertically but has the same 40 random-color colorbar as the other seismic-interval velocity displays.

Figure 2.11: Temperature and pressure effects on halite velocities under borehole conditions. After Yan et al., 2014 SEG annual meeting.

Figure 2.12a: shows a sample of halite and gypsum in ordinary light, both are white to clear and crystalline.

Figure 2.12b: is a similar sample under UV light and the gypsum exhibits a "pale or dull yellow" fluorescence, indicating a few percent (3% to 5%) gypsum present.

Figure 2.12c: exhibits a "bright yellow" fluorescence indicating about 10% to 20% gypsum present.

Figure 2.12d: shows a "strong yellow" fluorescence indicating 40% or more presence of gypsum (images from www.galleries.com/minerals /property/ fluorescence.htm). These are semi-quantitative measurements of percentage content because the amount or the intensity of fluorescence of gypsum can vary with temperature, as well as the subjective descriptions by the mudlogger. It is one of the minerals that exhibit a slight fluorescence at room temperature but that intensity will increase significantly as temperature decreases to -50°C (McDougall, 1952). One hopes that these mudlog observations were made over a relatively short time span not experiencing drastic temperature fluctuations, such that they are correct relative to each other. There is a way to quantify the fluorescence signal emitted that is used in molecular/cellular biology called fluorescent microscopy. However, it is used on microscopic-sized samples and hasn't been used in mudlogging, at least to my knowledge (http://faculty.jsd.claremont .edu.jarmstrong/fquant/).

Figure 2.13: Interval velocity with a scale of 5,000 ft/s (l1524 m/s) in light blue to 23,000 ft/s (7010 m/s) in light pink vs. well depth in feet along dip arbitrary line A-A' in central Keathley Canyon. The color range for halite V_{int} is orange on this scale.

LIST OF TABLES

Table 2.7: Mudlog description of components within salt Group 5 in the northern area. These wells have significant anhydrite as the secondary salt component with gypsum usually being the third component.

Table 2.8: Estimates of salt-body components for 44 wells based on mudlog descriptions. Salt-body V_{int} represent the whole salt column, except for wells marked with an asterisk. Those wells indicate that the velocity measurement did not penetrate the whole salt body and the stated velocity is representative only of the measured section. Column labeled "Clastics or other" includes pyrite, shale, siltstone, claystone, limestone, sand, marl, bitumen and tar. Note that the standard deviations and the mean values were calculated without the outlier well GC-955-002.

Table 2.9: Mineral chart with elastic constants used in mineral modeling calculations. An additional source consulted was Robertson et al, 1958, but decision was made to use more recently calibrated values for halite, anhydrite and gypsum.

Table 2.10: Calculated Hashin-Shtrikman bounds values and derived V_p for all study wells.

Table 2.11: Calculated proportional bounds based on volume fraction and derived $V_{\mathbf{p}}$ for all study wells.

Table 2.12: Bulk and shear moduli calculated using multicomponent Hashin-Shtrikman bounds and the velocities derived from them for the 23 wells having more than 2 components within salt.

Table 2.13: Mean absolute deviation (MAD) and mean-squared error (MSE) for the velocities from standard Hashin-Shtrikman bounds, proportional bounds and multicomponent Hashin-Shtrikman bounds compared to the measured salt Vint. The English velocity units are in ft/s (so the numbers are relatively large) and the metric velocity units are in m/s.

Table 2.14: Mean absolute deviation (MAD) and mean-squared error (MSE) for the velocities from standard H-S bounds, proportional bounds, multicomponent H-S bounds, Wyllie Time-Averages, and Backus Averages compared to the measured salt $V_{\mathbf{int}}$.

Table 2.15: Wyllie Time Average derived velocities and Backus Average derived velocities compared to the measured salt $V_{\mathbf{int}}$.

Table 2.16: . Borehole temperature gradients for 63 wells in the study area.

Table 2.17: Borehole (mud) pressure gradients for 66 wells in study area. Wells included in the salt study are color-coded as to their group in Tables 3-7. Not all of these wells were included in the full analysis due to missing information in part. Some wells are missing mudlogs for salt

composition and some wells are missing velocity information inside the salt.

1 Introduction

1.1 THE RELEVANCE OF THE DEEPWATER GULF OF MEXICO

The idea for this research was to explore practical geophysical applications that could aid industry in its pursuit of hydrocarbon reserves in the deepwater areas of the GoM. So much emphasis has been placed on improving seismic acquisition and processing techniques, there was an opportunity to work with velocity modeling. The goal was to develop a regional 3D velocity model based primarily on extensive well control, using the best seismic data available for academic research. How would this compare with a traditional 3D velocity model? In examining the well log data needed to build a deepwater GoM wellbore database, it soon became apparent how much salt there was both in thickness and areal extent within the study area. In some areas, the salt would be as much as 20-50% of the local 3D velocity model (in the Shenandoah sub-basin, salt is over 20,000 ft or 6096 m thick). How would that much salt affect the velocity model and the quality of subsalt imaging? That would require a detailed investigation into the salt itself, but without having any salt cores, it would require the extensive use of mudlogs.

The remainder of this chapter discusses the importance of the GoM as a petroleum province, the extension of exploration and production out into its ultra-deep waters, the development of technology that enabled this pursuit, and lastly, the emergence of the Wilcox trend as a viable oil and gas target zone. Chapter 2 introduces the discovery that the interval velocities of these deepwater salt-bodies vary latitudinally over the study area; and so an investigation was undertaken as to how this is possible. Chapter 3 discusses the building of a regional 3D-geological velocity model using high-resolution 2D seismic data in conjunction with all available wellbore data in the study area.

1.1.1 The Gulf of Mexico as an oil and gas province

As a regional area of continuing large oil and gas discoveries, the deepwater area of the Gulf of Mexico (GoM) is a premier petroleum province; in 2016 it supplied 17% of the total U.S. crude oil and 5% of the total U.S. dry gas production. “Over 45% of total U.S. petroleum refining capacity is located along the Gulf coast, as well as 51% of total U.S. natural gas processing plant capacity” (U.S. Energy Information Administration). Figure 1.1 is a map showing the geographic distribution of active leases in the GoM by water depth. Note that a lot of the shallow water leases offshore Texas have expired, meaning they are no longer held by active production.

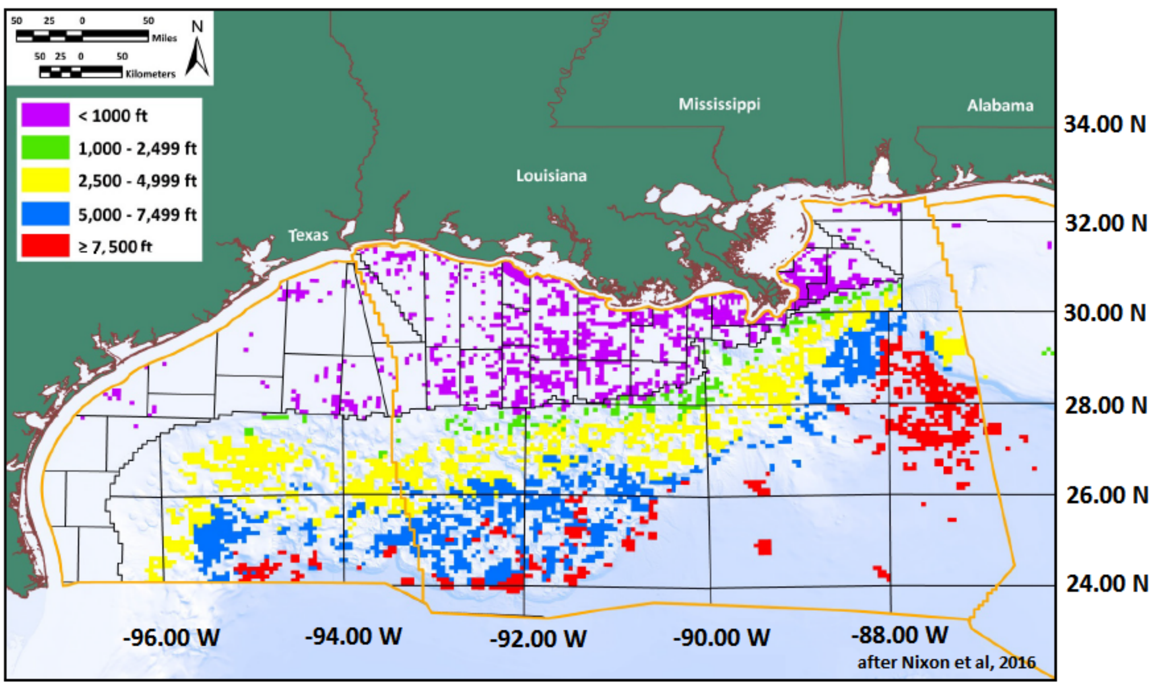

Figure 1.1 Geographic distribution of active leases in 2016 by water depth in the Gulf of Mexico.

1.1.2 A brief history of drilling in the deepwater GoM

A few highlights of deepwater milestones in the deepwater GoM include:

- 1988: The first subsea completion occurred in Ewing Banks block 999 for the GC029 Field in 1,462 ft of water.

- 1989: The first tension-leg platform (TLP) was installed in Green Canyon block 184 at the Jolliet Field in 1,760 ft of water.

- 1990: The first subsalt discovery in deepwater was drilled in Mississippi Canyon block 211 at the Mica Field in 4,356 ft of water.

- 1996: the first deepwater well to encounter Wilcox-equivalent, Lower Tertiary sediments was drilled in Alaminos Canyon block 600 at the Baha prospect in 7,260 ft of water.

- 1999: Deepwater oil production overtook that in the shallow water.

- 2003: The first semi-submersible was installed in Mississippi Canyon block 474 in 6,340 ft of water. The production platform collects gas from six different fields.

- 2007: The *Independence Hub* was installed in Mississippi Canyon block 920 in 7,920 ft of water, claiming the world water-depth record for a semi-submersible. The hub hosts production from 11 fields.

- 2009: The first floating production platform (FPU) was installed in Green Canyon block 237 in 2,200 ft of water, acting as a hub for the Boris and Phoenix Fields. The *Perdido Hub* was installed in Alaminos Canyon block 857 in 7,817 ft of water, claiming the world water-depth record for a spar, and hosting production from three fields.

- 2010: The Macondo discovery blowout and explosion aboard the Deepwater Horizon drilling rig causing oil to flow into the GoM for 87 days before the well was sealed.

- 2010: The first floating, drilling and production triple-column spar was installed in Mississippi Canyon block 941 in 4,050 ft of water, named the *Telemark Hub*, hosting production from three fields.

- 2011: The first floating production, storage, and offloading facility (FPSO) was used in Walker Ridge block 249 in 8,300 ft of water, claiming the water-depth record for a production facility in the GoM. The FPSO acts as a hub for the Cascade and Chinook Fields.

- 2011: The Bureau of Ocean Energy Management (BOEM) and the Bureau of Safety and Environmental Enforcement (BSEE) were created when the Minerals Management Service (MMS) was divided into three independent agencies.

- 2014: The largest ever semi-submersible was installed at Walker Ridge block 718 in 6,950 ft of water with the platform hosting production from the Jack and St. Malo Fields.

All of the above milestones were taken from OCS Report BOEM 2016-057 (Nixon et al., 2016).

1.1.3 Production history of the deepwater GoM

Table 1.1 is from www.data.bsee.gov, and shows deepwater GoM production from years 1985 through 2014. Note that the percentage of production for the deepwater area has grown during that same time span from 6% to ≈ 82% for the total GoM oil production and from <1% to ≈54% for the total GoM gas production. As the more recently discovered fields come online over the next few years, that percentage will continue to grow. The reason why: Exploration and development are so very expensive in the deepwater parts of the basin, especially for subsalt targets; the projected reservoir size must be enormous in order to cover the production costs and make a profit.

Figure 1.2 is a not a graphic representation of the numbers presented in Table 1.1 because the graph represents the whole U.S. federal area offshore in the GoM (not just the deepwater areas in Table 1.1) plus it contains additional data for years 2015 and 2016. In spite of the industry's economic downturn in the summer of 2014, the production continued to slowly increase through 2014, unlike oil production from some of the onshore unconventional plays, which were impacted more by the sudden drop in oil prices.

In the ultra-deepwater areas of the GoM such as Alaminos Canyon, Keathley Canyon, Walker Ridge, Garden Banks, and Mississippi Canyon, the time lapse between an initial discovery and first production averages about eight years. Figure1.3 is a graph showing the total number of deepwater wells drilled by year and by depth in the Gulf of Mexico. Note that the year 2001 was a year of major change, the number of wells drilled in the shallower part (between 1,000 ft to 2,499 ft, colored green) for the deepwater areas started to decline, while the number of wells drilled in the other three deeper-water categories all began to increase. In general, as the number of exploration prospects dwindled in the green water-depth zones, operators were forced to look for prospects in the deeper water areas.

Production Data by Year						
	Deepwater Production (WD > 1000 Ft)		Total GOM OCS Production		% of Total Production	
Year	Oil, STB	Gas, MCF	Oil, STB	Gas, MCF	Oil	Gas
1985	21,053,752	34,527,255	350,345,117	4,138,956,486	6.009	0.834
1986	19,077,066	37,639,373	355,542,244	4,124,326,693	5.365	0.912
1987	17,070,926	45,145,878	327,567,672	4,615,442,470	5.211	0.978
1988	12,984,552	38,994,103	301,206,145	4,669,062,881	4.310	0.835
1989	10,007,573	32,527,752	280,717,909	4,729,179,975	3.564	0.687
1990	12,141,988	31,113,841	274,588,473	5,006,062,619	4.421	0.621
1991	22,886,754	59,604,768	294,773,846	4,801,921,142	7.764	1.241
1992	37,295,127	89,003,675	304,865,294	4,743,703,591	12.23	1.876
1993	36,769,914	122,296,667	308,595,948	4,749,049,920	11.91	2.575
1994	41,803,238	162,666,899	314,095,928	4,920,343,747	13.30	3.306
1995	55,200,884	184,645,209	345,074,597	4,874,359,642	15.99	3.788
1996	72,213,069	283,806,147	368,869,292	5,178,550,641	19.57	5.480
1997	108,514,650	389,404,718	411,622,518	5,248,698,790	26.36	7.419
1998	159,232,680	567,567,774	444,286,882	5,110,552,769	35.84	11.10
1999	225,089,761	845,581,180	495,172,107	5,057,740,045	45.45	16.71
2000	271,144,316	998,859,653	523,029,835	4,958,172,377	51.84	20.14
2001	315,392,362	1,178,429,028	558,789,560	5,060,560,937	56.44	23.28
2002	348,566,124	1,286,974,486	567,877,774	4,526,471,813	61.38	28.43
2003	350,148,830	1,425,743,793	561,420,633	4,428,927,788	62.36	32.19
2004	347,953,910	1,396,314,335	535,355,490	4,005,739,765	64.99	34.85
2005	325,578,420	1,189,883,544	466,925,700	3,155,658,994	69.72	37.70
2006	341,354,260	1,093,965,240	472,077,444	2,922,176,102	72.30	37.43
2007	328,133,335	1,027,089,948	468,008,677	2,812,717,546	70.11	36.51
2008	312,730,034	999,057,060	423,420,227	2,329,950,762	73.85	42.87
2009	457,552,497	1,103,080,864	570,309,328	2,451,076,806	80.22	45.00
2010	460,656,533	1,065,123,954	566,628,373	2,250,413,436	81.29	47.33
2011	378,436,854	854,651,703	481,702,084	1,826,618,802	78.56	46.78
2012	367,563,906	725,113,422	464,796,010	1,535,904,630	79.08	47.21
2013	361,761,808	637,949,079	459,012,835	1,328,177,848	78.81	48.03
2014	416,390,514	687,867,968	510,491,334	1,276,519,753	81.56	53.88

Table 1.1 Gulf of Mexico deepwater production between 1985 and 2014 from www.bsee.gov. Note the steady increase in the percentage of the total production from the GoM by the deepwater fields. The abbreviation STB is for “stock tank barrels of oil” and the abbreviation MCF is for “million cubic feet”.

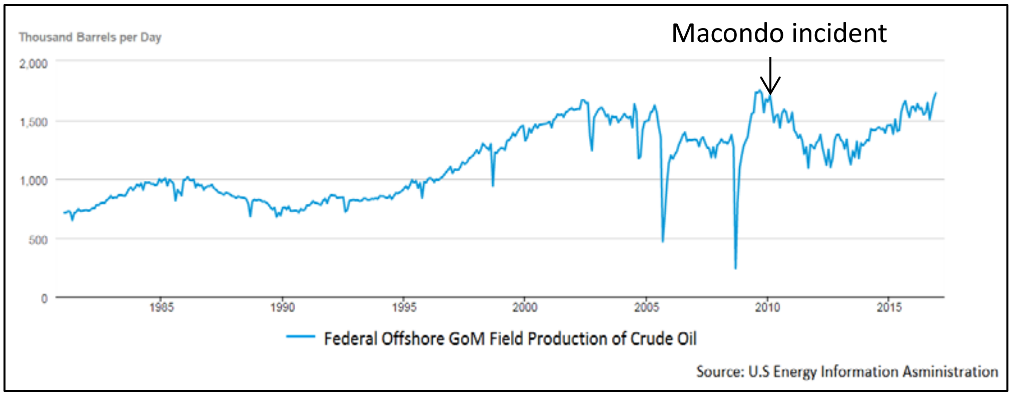

Figure 1.2. Federal offshore GoM field production of crude oil between 1981 and 2016.

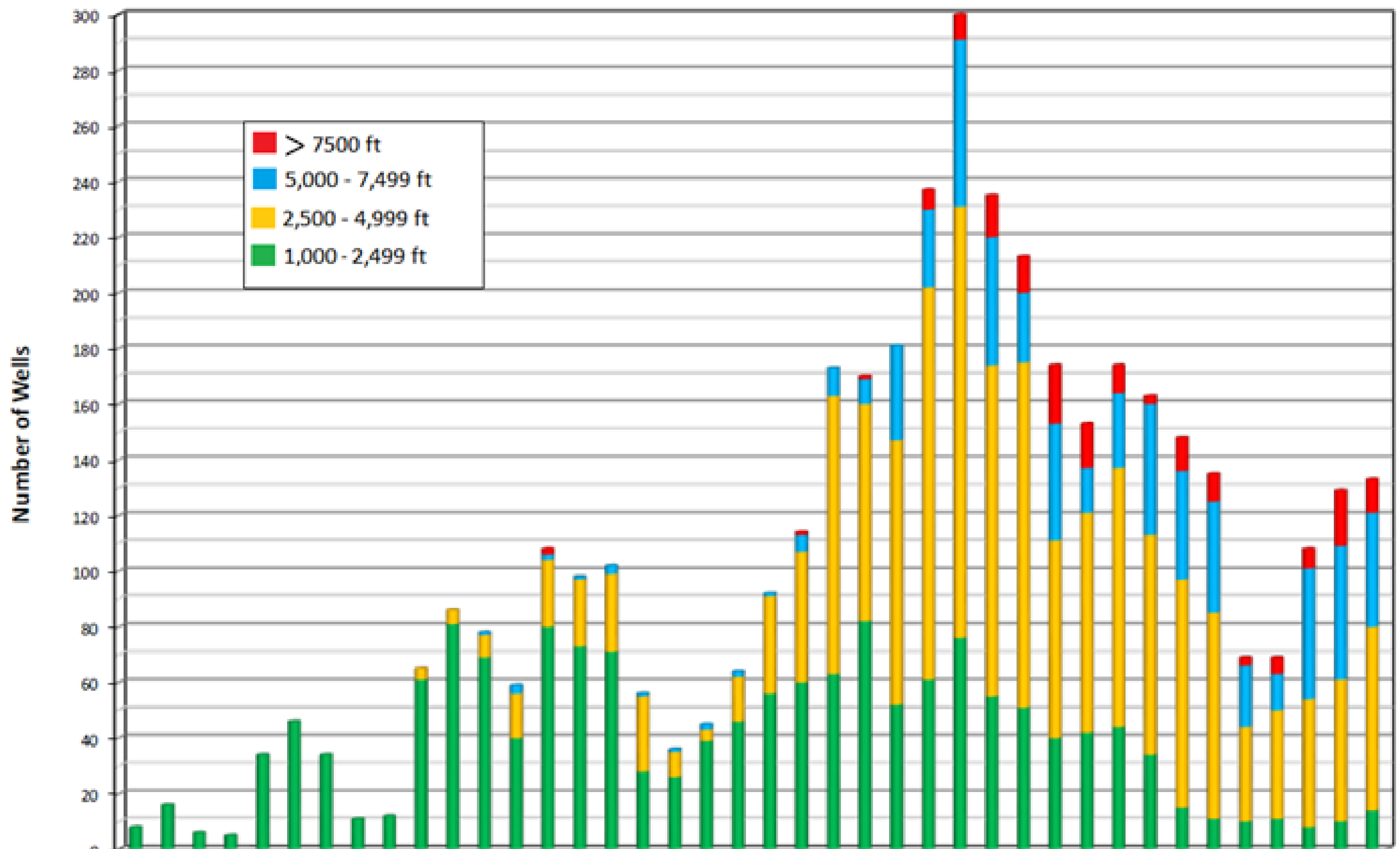

1975	1976	1977	1978	1979	1980	1981	1982	1983	1984	1985	1986	1987	1988	1989	1990	1991	1992	1993	1994	1995
													2							
											1	3	2	1	3	1	1	2	2	1
									4	5	8	16	24	24	28	27	9	4	16	35
8	16	6	5	34	46	34	11	12	61	81	69	40	80	73	71	28	26	39	46	56

1996	1997	1998	1999	2000	2001	2002	2003	2004	2005	2006	2007	2008	2009	2010	2011	2012	2013	2014
1		1		7	9	15	13	21	16	10	3	12	10	3	6	7	20	12
6	10	9	34	28	60	46	25	42	16	27	47	39	40	22	13	47	48	41
47	100	78	95	141	155	119	124	71	79	93	79	82	74	34	39	46	51	66
60	63	82	52	61	76	55	51	40	42	44	34	15	11	10	11	8	10	14

Year

after Nixon et al., 2015

Figure 1.3. Total number of deepwater wells drill by year and by water depth in the GoM.

During the past 10 years, the most concentrated drilling activities and most of the discoveries have been made in the Keathley Canyon and Walker Ridge areas. Hence, these two areas were selected to be the research study area. Figure 1.4 shows the estimated reserves for the deepwater areas of the GoM with Keathley Canyon (on the left) and Walker Ridge (on the right) inside the red-boxed area. New fields have come on stream and several large discoveries have been made in Garden Banks, Green Canyon, Keathley Canyon, and Walker Ridge since 2014, but do not show on this map.

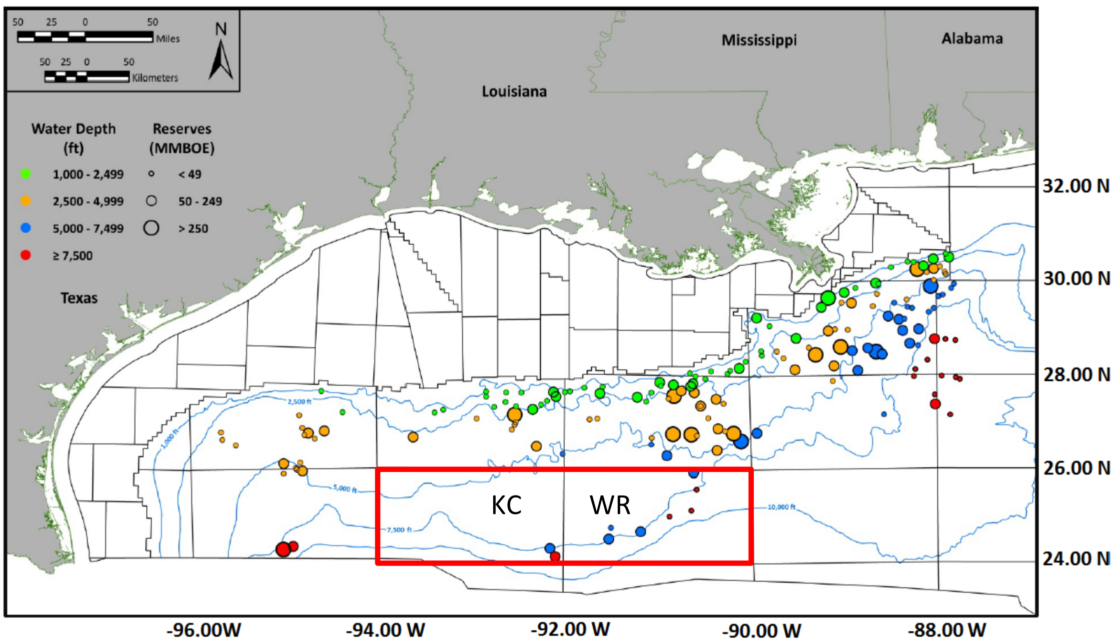

after Nixon et al., 2016

Figure 1.4 Estimated reserves for Gulf of Mexico deepwater fields as of December 31, 2014. MMBOE = Million barrels oil equivalent.

1.2 ADVANCES IN TECHNOLOGY IMPROVE THE DRILLING SUCCESS RATE IN DEEPWATER

In the last 20 years, exploration and production in the GoM have focused on Plio-Pleistocene and Miocene mini-basins, ultra-deepwater (>5,000 ft water depth) Lower Tertiary subsalt prospects, and Lower Miocene reservoirs in the deep Shelf areas (see Figure 1.9). In order to offset some of the high risks accompanying these difficult exploration targets and field developments, many technological advances have been required to facilitate successful ventures in these geologic settings, while expanded infrastructure has been created to support the delivery of oil and natural gas to market (Herbst, 2009). For these upstream endeavors in difficult- to- define subsalt reservoirs, new techniques in acquiring and processing seismic data, along with the wireline-log data being collected in high-temperature-high pressure depths required new technology.

1.2.1 Advances in seismic data

Until the mid-1980s, all marine seismic surveys were mainly 2D with only a few of the much more expensive 3D surveys being acquired. However, during the 1990s it became apparent as the drilling cost increased substantially with increased water depth, that the need for more precise imaging of the subsurface was crucial for drilling success. In 2006, the first non-exclusive, wide-azimuth seismic survey was acquired in the deepwater area. Imaging below salt is difficult due to its higher sonic velocity, its thickness, and the rugosity of allochthonous Louann Salt. Depth migration improved subsalt imaging over its time migration predecessor; but still subsalt imaging problems such as poor signal-to-noise ratio and inadequate reservoir illumination persisted. A small part of the improvement in subsalt imaging was due to advances in velocity model-building technology that incorporated beam-based interactive imaging to refine salt geometry (Wang et al, 2008). Even so, it soon became apparent that another approach to seismic imaging was needed, other than the standard narrow azimuth (NAZ) techniques. A new seismic imaging method would have to have the potential to produce higher quality seismic images in the ultra-deep water environment. “Complex-azimuth” seismic surveys considerably improved the illumination in complicated subsalt environments and also provided natural attenuation of some multiples. Figure 1.5 schematically describes the various types of seismic acquisition geometries that have been tried in the deep-water GoM arrayed chronologically from left to right and with the cost of acquisition also rising from left to right (Nixon et al, 2016).

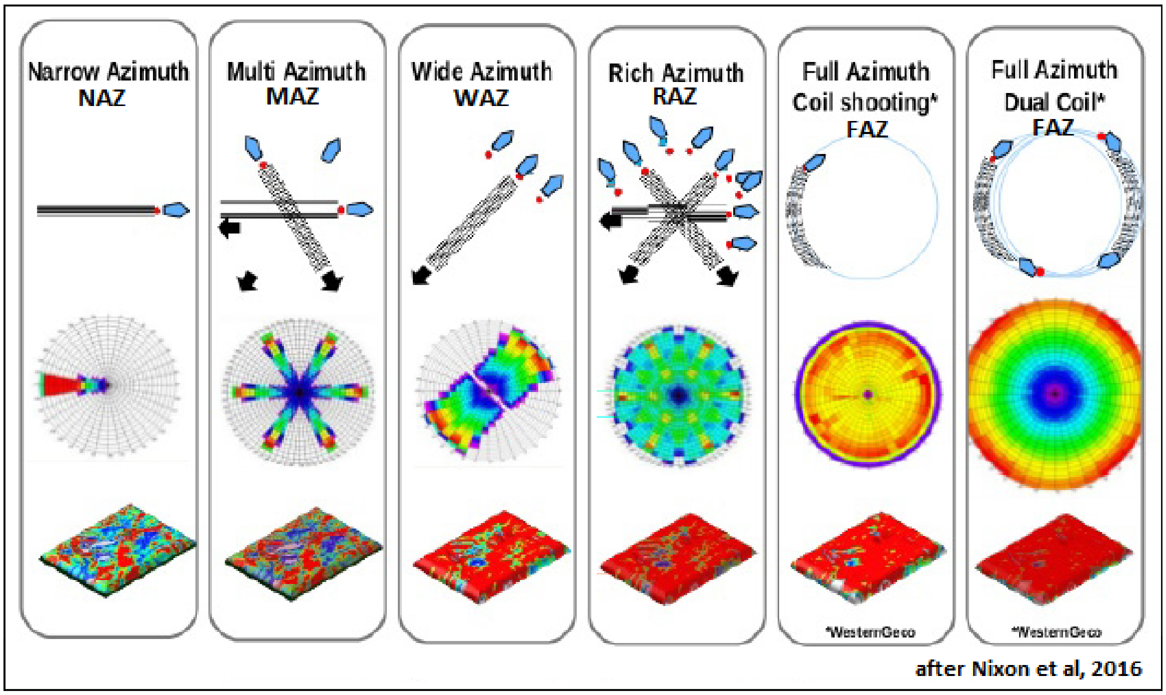

Figure 1.5 Seismic acquisition geometries resulting in azimuth ranges from 0° to 360°, and planar view illumination. Offset corresponds to the distance from center of each rose diagram and azimuth corresponds to the angle within each rose diagram. Colors represent the number of traces recorded for each offset-azimuth combination, with purple and blue for a low number of traces, to green to yellow and then red, for a high number of traces. Coil surveys are a proprietary acquisition technique of Schlumberger (formerly Western Geco).

Some operators will choose to use nodes or cables placed directly on the seafloor over a single field. This is usually done either in the development phase or in the production mode to continuously monitor the drawdown of the reservoirs. The different types of seismic data coverage acquired for the GoM are shown in Figure 1.6. Note that the most expensive and the highest quality surveys (FAZ) have been utilized in the deep-water areas, where the salt canopy is the most prevalent.

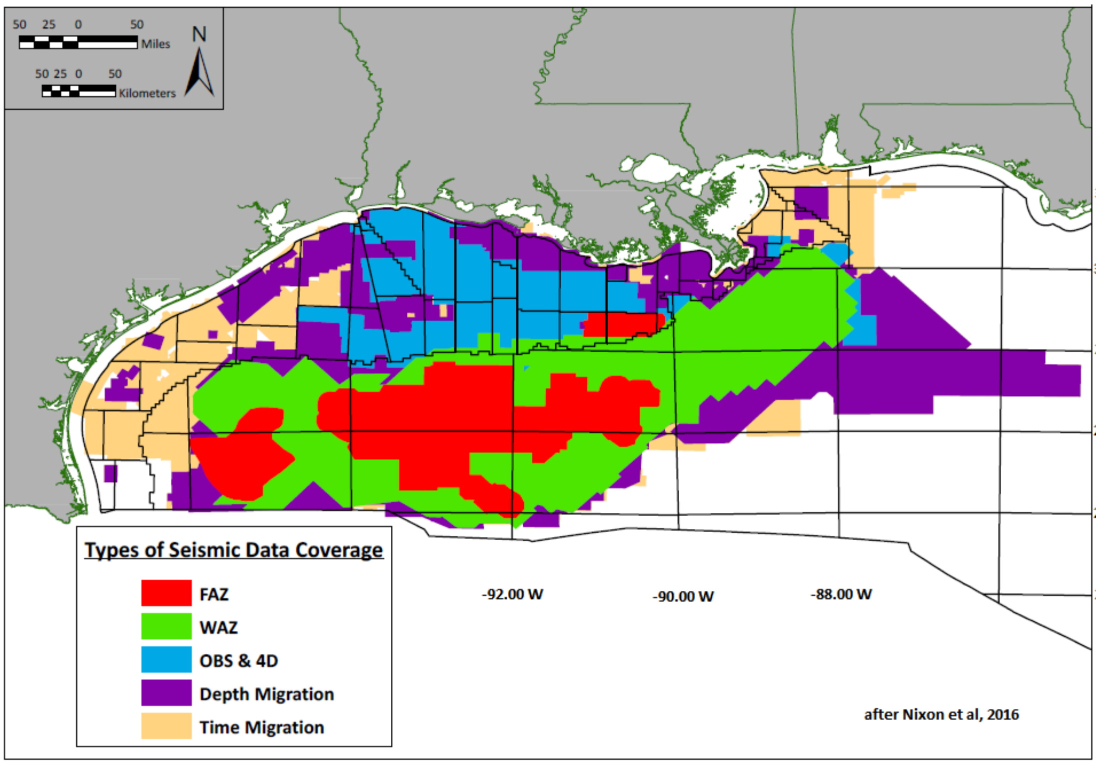

Figure 1.6 Different types of seismic data coverage obtained by BOEM through the end of 2014. Operators are required to submit copies of both seismic and well data to the government regulatory agency. Seismic data will not be released to the public until it is 20 years old.

Creation of new algorithms used in seismic processing are another important advancement for seismic data quality. Utilization of reverse-time migration (RTM) in seismic processing has greatly increased the quality of the subsalt imaging (as well as the cost) and with that, the success rate in drilling. Various other forms of sophisticated depth migration have been tried as the economic demands for drilling success increase in proportion to the added cost of computer time for these more precise processing solutions.

1.2.2 Advances in collecting well log data

The big increase in drilling activity for the Keathley Canyon and Walker Ridge areas began in 2007, as shown by the well log data acquired from the government website www.bsee.gov. A search on that same website showed that there were 362 exploration and development plans approved for the Keathley Canyon area between January 1, 2007 and March 22, 2017, where only 93 permits were approved in the preceding 12 years. Similarly, for the Walker Ridge area, there were 354 exploration and development plans approved between January 1, 2007 and March 22, 2017, where only 183 were approved in the preceding 12 years.

This significant increase in drilling activity has created a vast database of wireline logs, mudlogs, deviation surveys, paleontological reports, and velocity surveys from these two prolific deepwater areas. As the demand for increased quality in seismic data has risen, so has the demand for improvement in well log data variability and dependability. In response to deepwater drilling worldwide, manufacturers of logging equipment have had to design for the likelihood of encountering both high-temperature (HT) and high-pressure (HP) at the bottom of the hole. Wells with undisturbed bottomhole temperatures above 150°C (302°F) are classified as high-temperature. Those wells with a downhole pore-pressure gradient exceeding 0.8 psi/ft (18 KPa/m) are considered high-pressure. HTHP wells are growing in number as deepwater exploration expands not only in the GoM but worldwide; and so the requirement for logging tools to function under these conditions demands new technologies to avoid both mechanical and electronic failure (Baird et al., 1998).

However, it is rare for the drilling operator to log the whole borehole in the deepwater GoM; it is common practice to only log below salt, or in some cases, only the targeted exploration zone. Not logging the whole borehole to obtain critical geological information does not make any scientific sense; and it is not the actual cost of logging that makes this virtually prohibitive. It is the daily-rig-rental charge and the time required to lower and raise the logging tools, especially for multiple logging runs with different types of logging tools, as well as the risk that such logging runs will encounter problems that may jeopardize the entire borehole. The current cost to drill a deepwater subsalt well in the GoM is $250 MM and the development cost to bring a deepwater field to production status can cost minimally a minimum of several billion dollars (Sullivan, 2017). Nevertheless, the size of the typical Wilcox turbiditic reservoir is so large; the initial cost of discovery and development can be recovered within the first few years of production, leaving the remainder of the field's production over time as mostly profit, less daily-operating costs.

1.3 THE WILCOX FORMATON IN THE DEEPWATER GULF OF MEXICO

Figure 1.7 shows a stratigraphic column for the Gulf of Mexico. In Keathley Canyon and Walker Ridge, the primary exploration target is the Lower Tertiary Wilcox Formation with the possibility of extra pay zones either in the Miocene or Pliocene. Lucius Field in the southeastern corner of Keathley Canyon produces from the shallower Pliocene-aged sands, even though the field is surrounded by other fields having the deeper Wilcox sand reservoirs. See Figure 1.8, which shows a map of all the current Wilcox discoveries in the GoM basin. Figure 1.9 is a map showing the depositional extent of offshore Wilcox sands and the location of Pleistocene, Pliocene, and Miocene sub-basins mentioned in section 1.2. Paleogene sediment sourcing for the Wilcox formation is not limited to the United States; there were several rivers along the Mexican east coast that also contributed to the Mexican equivalent of the Wilcox deposition in the western-most parts of the GoM (Colmenares and Hustedt, 2015). Figure 1.10 shows sediment sourcing

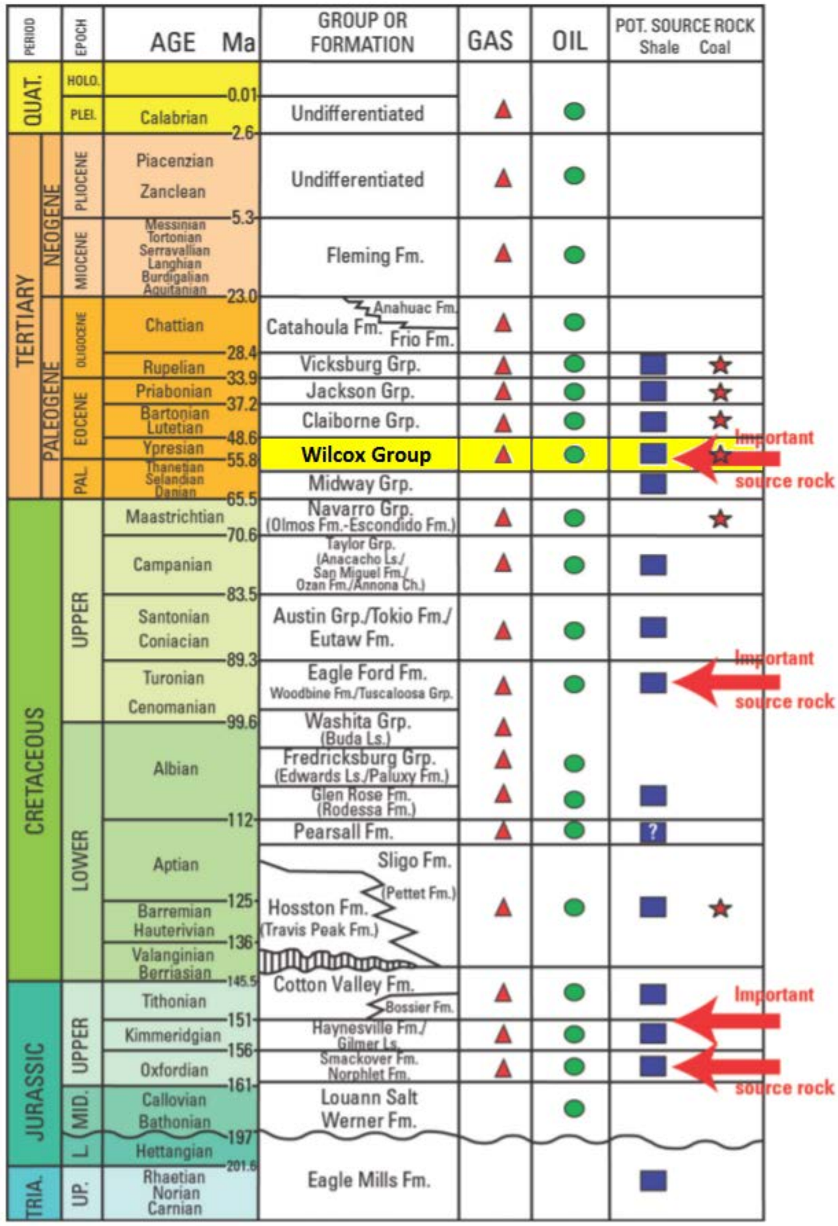

Figure 1.7 Geological stratigraphic column for the Gulf of Mexico showing units from the Upper Jurassic to the Cenozoic that are proven reservoir rocks. After USGS report 2012-1144.

for the Wilcox from the Mexican point of view, which is biased towards its western GoM contributions. Note that in Figure 1.10, the Wilcox is more prominent offshore Mexico. Likewise, Figure 1.11 shows sediment sourcing for the Wilcox from the American point of view, which is also biased, but towards contributions made in the central GoM. Only when drilling commences in the recently acquired Mexican deepwater blocks will the truth be determined.

The Mexican government offered offshore deepwater blocks in these potential Wilcox reservoir areas (inside red-marked area in Figure 1.10). Round 1 bidding for these blocks was held in 2015, culminating with eight blocks in this area being awarded in December, 2016 (Zborowski, 2016). What we do know from extensive geological analysis of the Wilcox formation on the American side (Meyer, Zarra and Yun, 2007) and (Lewis and Zarra, 2007) is that the grain size of the Wilcox sands diminishes from west to east, so that the Mexican side has a higher potential for reservoir quality sands. This is confirmed by the porosity and permeability in Wilcox sands plotted versus geographic location as seen in Figures 1.12 and 1.13 compiled by the BOEM. The porosity plot in Figure 1.12 and the permeability plot in Figure 1.13 both show that the Wilcox sands in Alaminos Canyon (the western part of the GoM) are more favorable to oil and gas production; and by inference the Mexican Wilcox sands should be better still.

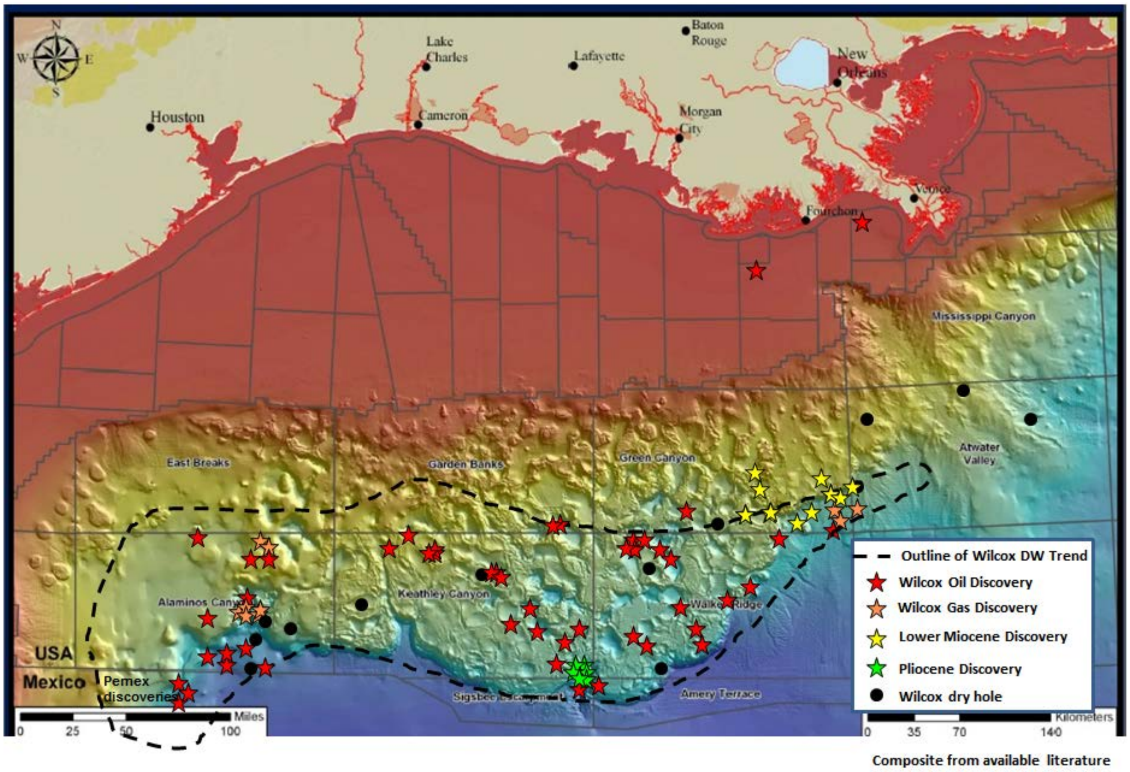

Figure 1.8. Current Wilcox discoveries in the Gulf of Mexico basin including some on the Mexican side of the international boundary. The underlying map is from 2014 GIS culture.

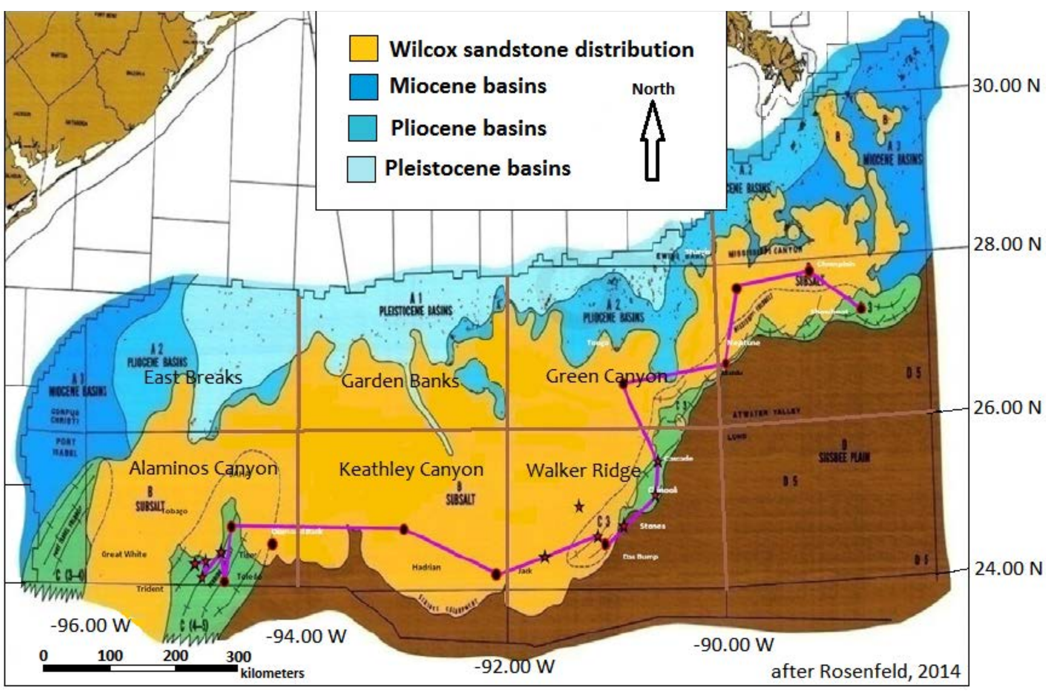

Figure 1.9. Wilcox sandstone distribution and location of Pleistocene, Pliocene, and Miocene sub-basins. Light brown designates onshore areas and dark brown locates the abyssal plain.

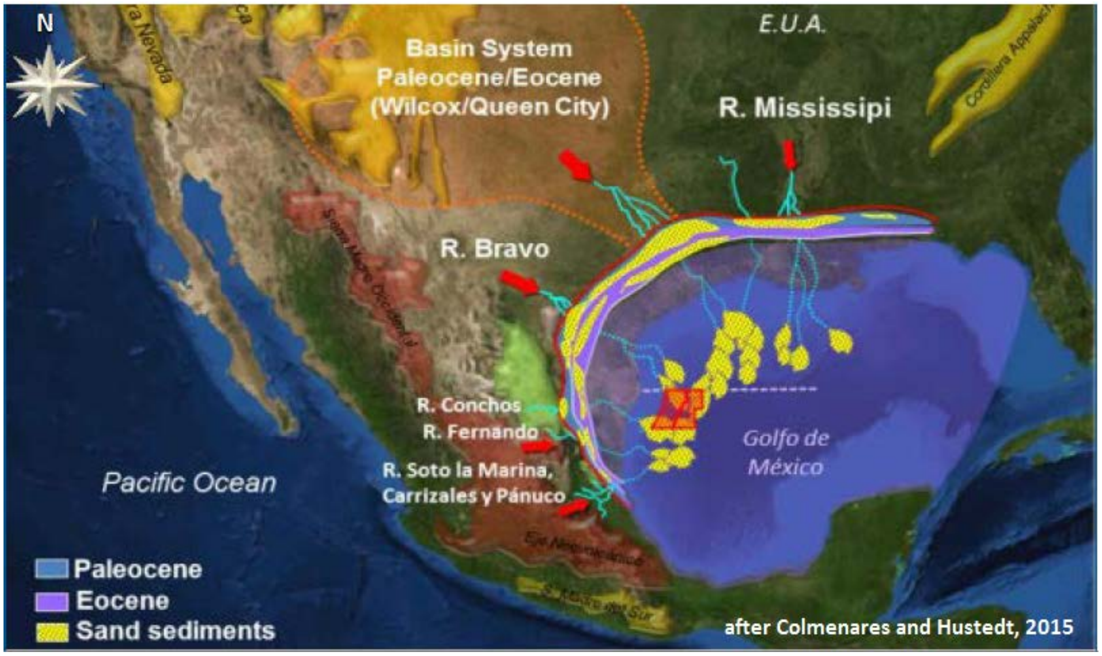

Figure 1.10. Sediment sourcing for the offshore Wilcox formation from a Mexican perspective. The yellow units represent slope fans in the Wilcox formation.

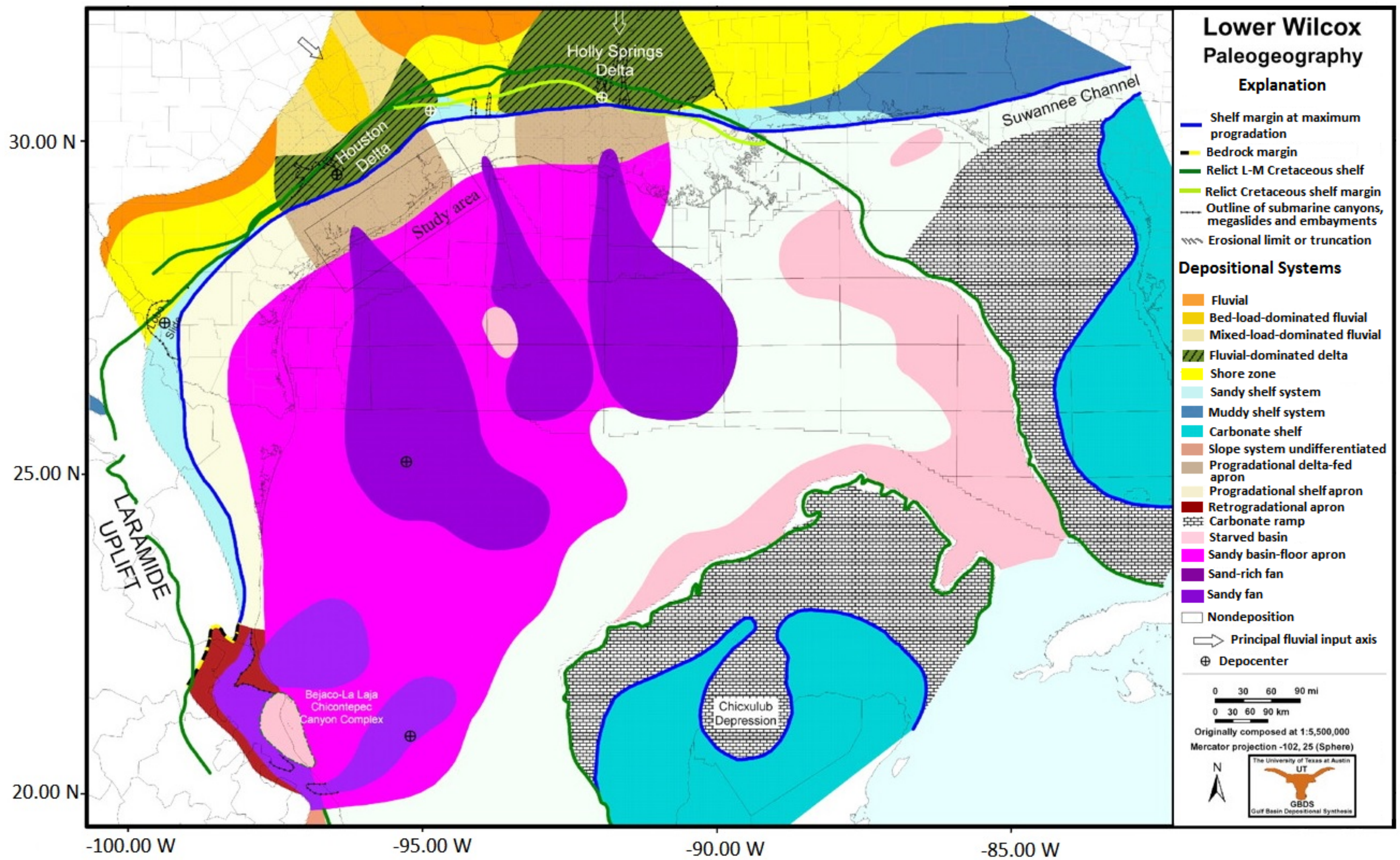

Figure 1.11. Wilcox sediment sourcing for the deepwater GoM from the American viewpoint (after the University of Texas at Austin Gulf Basin Depositional Synthesis, Institute for Geophysics). The dark purple units represent sandy slope fans in the Wilcox formation.

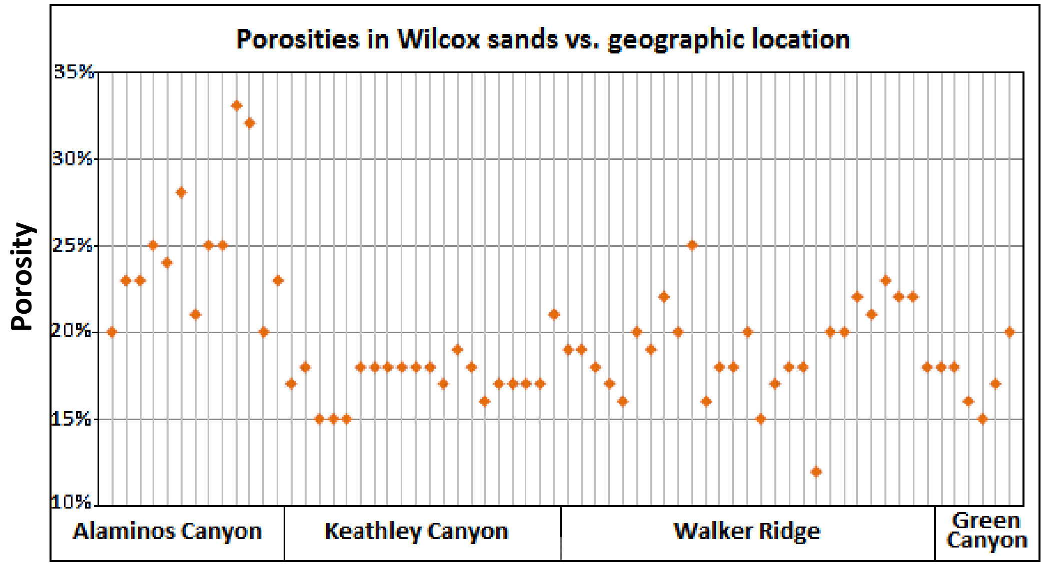

Figure 1.12 Plot of Lower Tertiary Wilcox sand porosities as a function of geographic location (after Nixon et al, 2016, p.35).

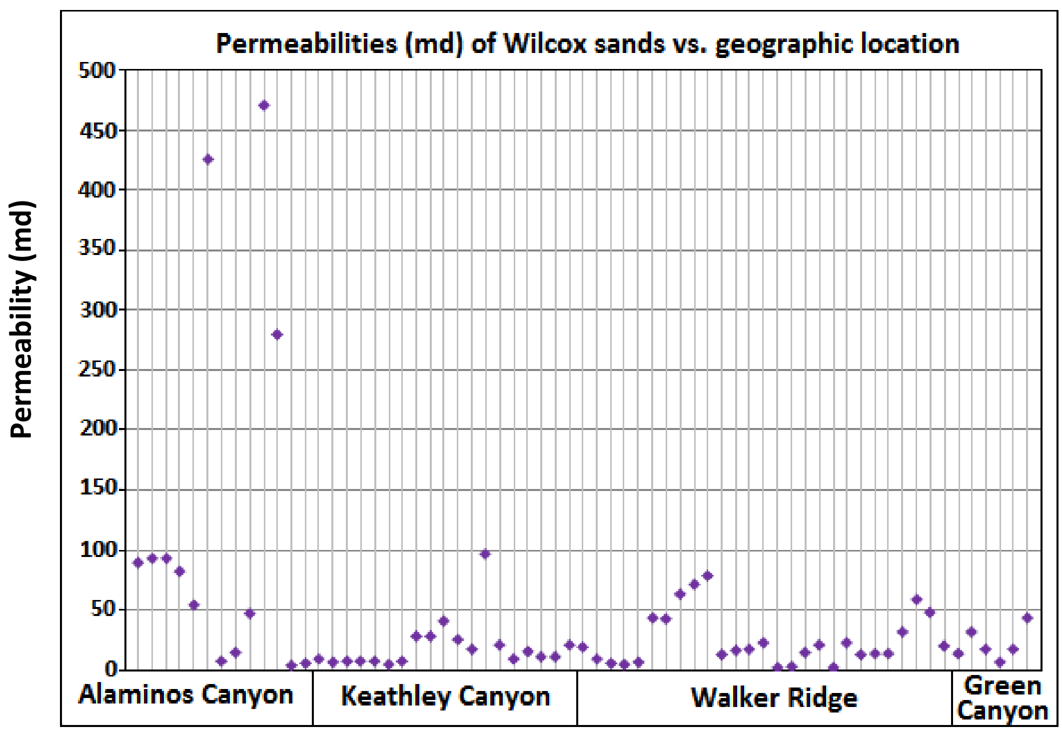

Figure 1.13 Plot of Lower Tertiary Wilcox sand permeabilities as a function of geographic location (after Nixon et al, 2016, p.35)

1.4 CHOICE OF RESEARCH TOPIC ALIGNED WITH CURRENT INDUSTRY INTEREST IN THE DEEPWATER GULF OF MEXICO

Accurate velocity measurements in deepwater salt and sediments are helpful in interpreting lithology, determining fluid content, and in creating velocity models for seismic processing. Most deepwater government leases are very expensive, consequently operators bid on single blocks or a small group of 2-3 blocks. During the exploration phase, these lease holders focus most of their efforts only on the immediate area surrounding their own lease(s); and as a result don't necessarily develop regional trends. Another reason for this is that high-quality 3D seismic surveys are usually contracted in multiclient surveys to help offset the exorbitant costs. The resulting seismic product is somewhat limited in geographical coverage, thereby limiting the scope of any regional investigation. Depending on the location of the lease(s), there could be wells nearby, or not. Currently, there are large expanses of deepwater territory without any drilled wells, so if the leased area does not happen to have nearby wells to confirm seismic interpretation, there could be difficulty in predicting reservoir rock physics properties, defining the structural trap, and/or in accurately locating the target. Figure 1.13 is a map of drilled wells in the study area showing their relative "pattern" geographically, along with the large open areas having no wells. All of these wells form the well log data base created for this study.

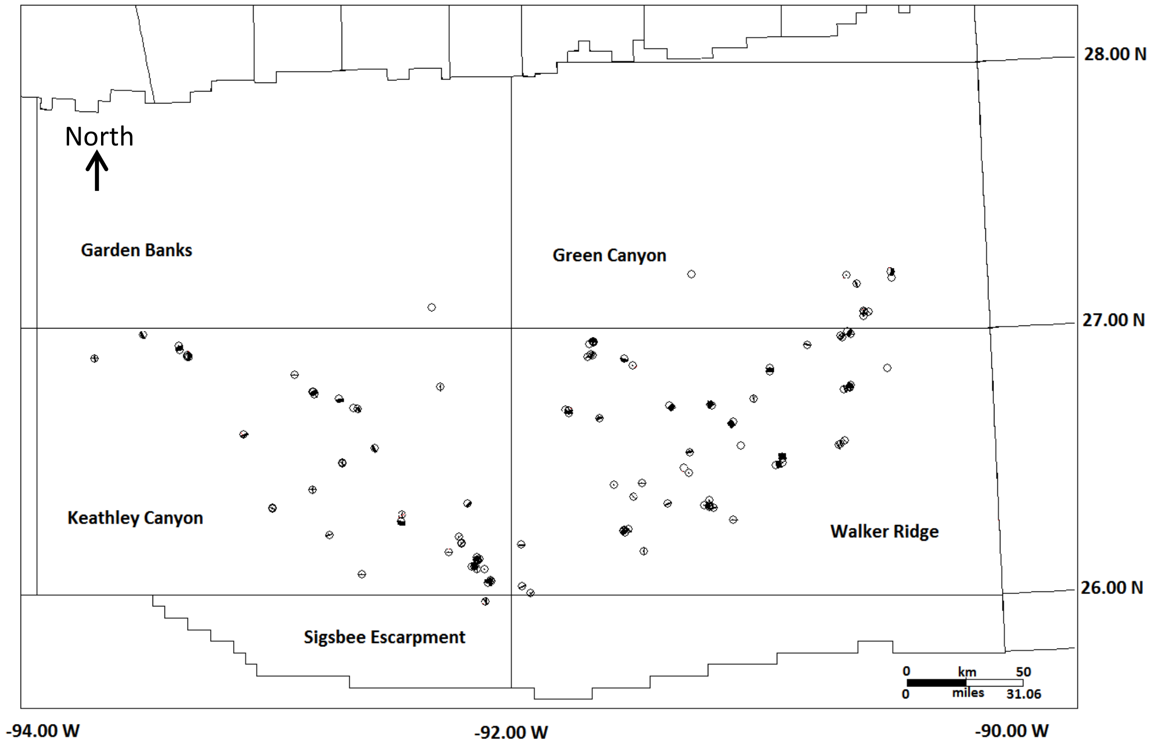

Figure 1.14 Wells drilled in the deepwater GoM research study area. Only the wells included in the study area are posted for Garden Banks and Green Canyon. The well log database has data for all wells posted on this map. Clear circles indicate a straight vertical well and the others show the well deviation in map view.

1.5 REFERENCES

Baird, T., et al, 1998, High–pressure, high–temperature well logging, perforating and testing, Oilfield Review, Summer edition, 50-68.

Colmenares, M. and Hustedt, J., 2015, Overview of the deepwater geology of the Mexican Gulf of Mexico—Round 1 of Bidding in the Energy Reform, Presented at Sixth Annual AAPG Deepwater and Shelf Reservoirs, Geosciences Technology Workshop.

Herbst, L., 2009, New batch of discoveries in deepwater keeping Gulf at forefront of U.S. production, American Oil & Gas Reporter magazine, April issue. (author was director of the U.S. Minerals Management Service Gulf of Mexico Region at the time).

Lewis, J. and Zarra, L., 2007, Exploration and Appraisal Challenges in the Gulf of Mexico Deep-Water Wilcox: Part 1—Exploration Overview, Reservoir Quality, and Seismic Imaging, GCSSEPM Annual Meeting Papers, 398-415.

Meyer, D., Zarra, L. and Yun, J., 2007, From Baha to Jack, Evolution of the Lower Tertiary Wilcox

Trend in the Deepwater Gulf of Mexico, The Sedimentary Record, **5**, no.3, 4-9.

Nixon, L., et al, 2016, Deepwater Gulf of Mexico December 31, 2014, OCS Report BOEM 2016-057, 1-99.

Rosenfeld, J. H. 2014, Paleocene-Eocene drawdown and refill of the Gulf of Mexico---Concept history and status, 27th Annual GCSSEPM Conference Proceedings, 330-350.

Sullivan, M., 2017, Relationship between reservoir quality, facies, and depositional environments working toward a predictive model for the deepwater Wilcox, Presented at Houston Geological Society on 6 March 2017.

U.S. Energy Information Administration, Gulf of Mexico Fact Sheet, https://www.eia.gov/special/gulf_of_mexico/, accessed 21 March 2017

USGS, https://energy.usgs.gov/OilGas/AssessmentsData/NationalOilGasAssessment/USBasinSummaries.aspx?provcode=5047, accessed 7 April 2017.

USGS, U.S. Geological Survey Open-File Report 2012-1144, https://pubs.usgs.gov/of/2012/1144/pdf/OFR2012_1144.pdf, accessed 24 April 2017.

Wang, B, et al, 2008, Advances in velocity model-building technology for subsalt imaging, Geophysics, **5**, no.5, VE173-VE183.

www.data.bsee.gov/homepg/data_center/production/summary.asp, accessed 20 March 2017.

www.eia.gov/dnav/pet/hist/LeafHandler.ashx?n=PET&s=MCRFP3FM2&f=M, accessed 21 March 2017.

Zborowski, M., 2016, BHP, CNOOC, European majors among winners for Mexican deepwater blocks, Oil & Gas Journal, 5 December 2016.

2 Latitudinal variation of salt-body interval velocities in the deepwater Gulf of Mexico: Keathley Canyon and Walker Ridge areas

2.1 INTRODUCTION

For many years, it has both been demonstrated and assumed that the mid-Jurassic Louann Salt was relatively uniform throughout the Gulf of Mexico (GoM) basin. Papers published by Fredrich (2007) and Zong (2016) show that Louann Salt is approximately 97-98% halite both from onshore salt domes and from offshore- continental shelf- allochthonous salt cuttings taken from boreholes. Consequently, most GoM 3D velocity models assume a constant interval velocity for salt where encountered. However, with the onset of intense drilling activity in the deepwater Gulf of Mexico beginning in 2007, data have been accumulating that suggest there is much more variability in the Louann allochthonous salt in the deepwater provinces (Jones, 2014).

The objective of this study is to synthesize a variety of salt-body interval velocity (V_{int}) measurements from the deep-water GoM to assess and understand any areal variability. The term “salt-body” refers to the composite intrusive formation penetrated by the borehole, which is primarily composed of halite, but includes all lithologies contained therein such as other evaporitic deposits and/or incorporated country rock. The rationale is to help guide the construction of velocity models for depth imaging, in which case the interval velocity of the entire salt-body is of interest, not just the halite component. The study was concentrated on the Keathley Canyon and Walker Ridge areas, where I had access to long-offset 2D seismic lines as well as well log information obtained from the www.bsee.gov website that I digitized.

Observations made in this area may be relevant to other parts of the deep-water GoM.

2.2 DATA USED IN THE STUDY

Well log data were purchased from the www.bsee.gov website, and then digitized for data entry loading into the IHS Kingdom software application for data registration in 3D space. A base map showing the well locations and seven 2D seismic lines and one 2D VSP line (for Green Canyon area) in the study area is shown in Figure 2.1. Fourteen wells in the study area did not encounter salt and they do not appear in Figure 2.1; however, they are a part of the database.

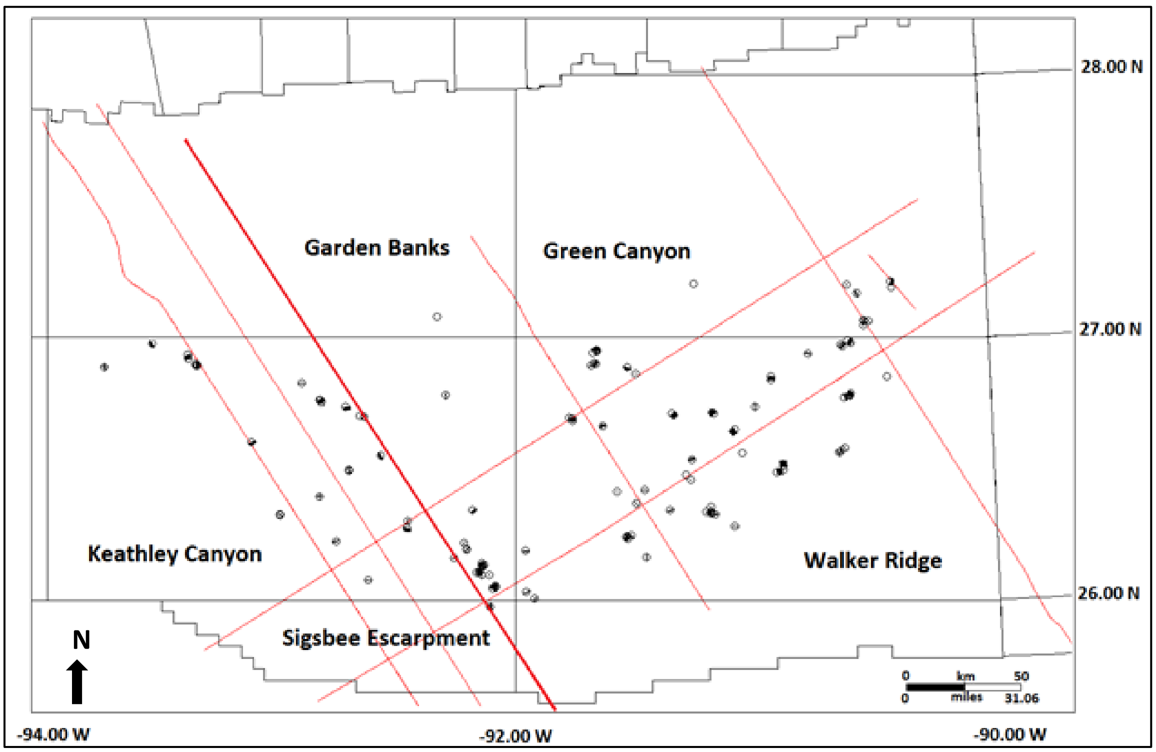

Figure 2.1. Study area base map displaying all wells containing salt and the seismic line locations shown by the red lines. Dip line 4250 is highlighted.

2.2.1 Seismic data

The seismic data used in this project were acquired in 2011-2012 by Dynamic Data Services employing an ultra-long cable of 15 km, towed about 60 ft below the sea surface using a special source of 9,100 cubic inches (twice the normal energy source). The resulting seismic data (Figure 2.2a), having 15 km offsets, are high-quality with 22 seconds of record. The Prestack Depth Migrated (PSDM) version of these profiles displays a vertical record of 130,000 ft (or roughly 40 km). The original seismic time processing assumed a salt velocity of 14,763 ft/s (4,500 m/s) in the Kirchhoff depth migration. This was a good estimate as in most cases the seismic salt-body interval velocities (V_{int}) match the well V_{int} within 3% for the 18 wells close to the seismic data, except at the southern and northern extremes of the study area where the velocities are significantly higher. The salt-body V_{int}, as used within this study, refers to the interval velocity of the entire salt-body penetrated by the borehole. The PSDM version of seismic dip line 4250 (Figure 2.2a) is highlighted in Figure 2.1 and the seismic interval velocity model (vertical axis in depth and velocities keyed to colors) that was used for processing is shown in Figure 2.2b. The irregularly-shaped features colored dark green are the allochthonous salt-bodies.

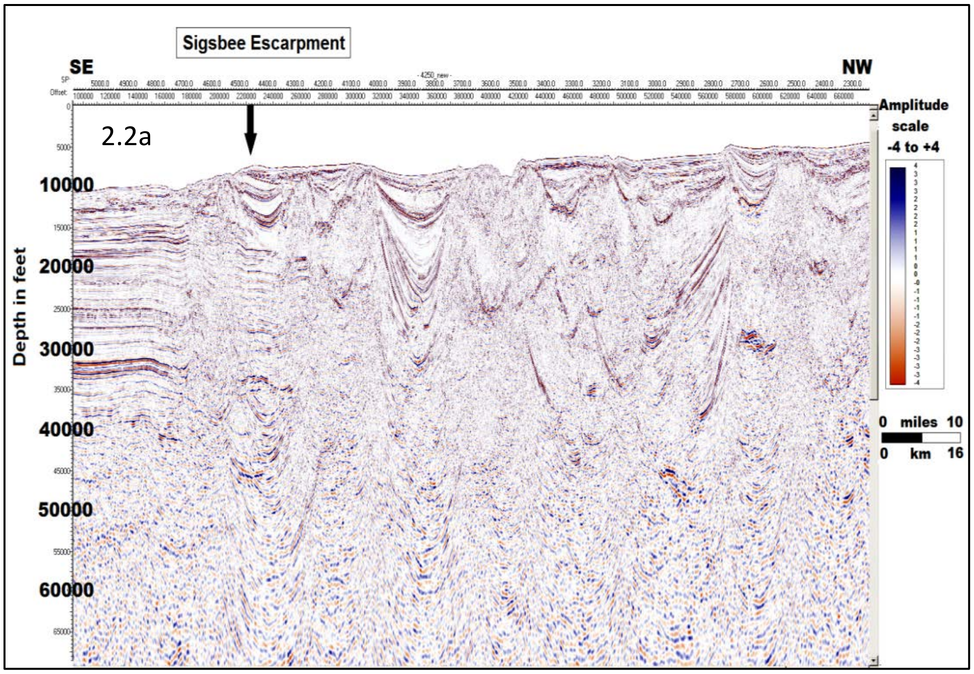

Figure 2.2a. Seismic dip line 4250 Kirchhoff PSDM.

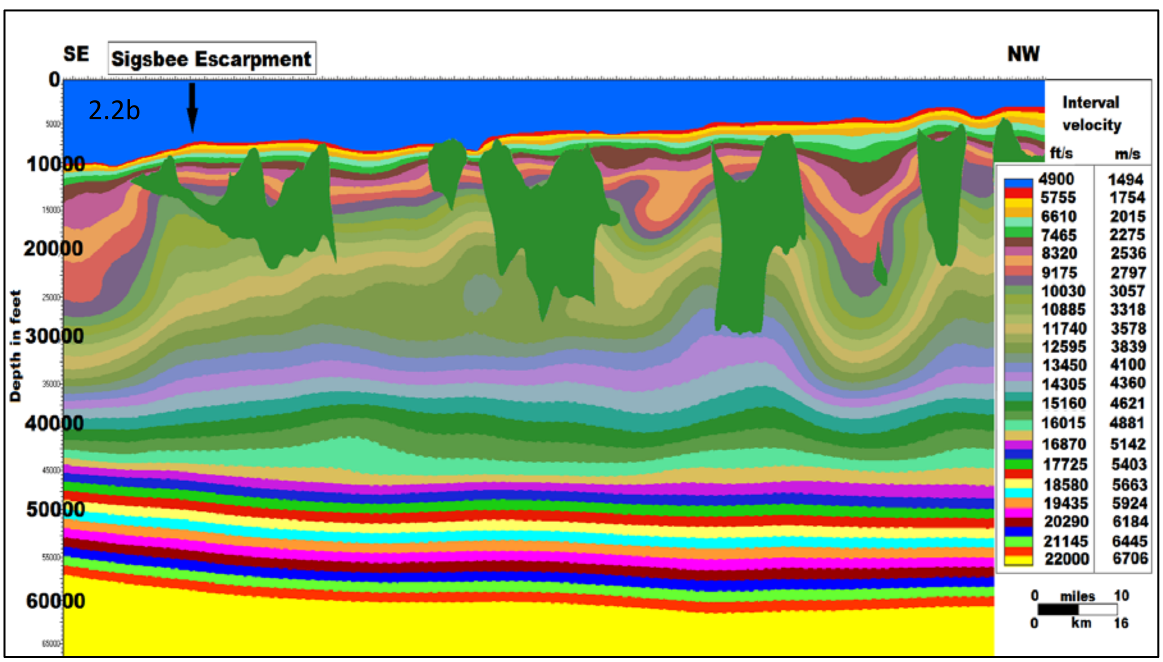

Figure 2.2b. Seismic interval velocity model (processing velocities) with allochthonous salt shown in dark green color. The interval velocity representation is derived from seismic processing velocities.

2.2.2 Well log data

Over 300 well logs were digitized from 110 wells within the study area; also included in the well data base are 78 mudlogs, 31 velocity surveys, 20 paleontological reports, numerous final well reports and a few initial drilling plans. Only 44 wells had both a mudlog and some form of sonic measurement through salt, or at least a partial sonic log measurement in salt. Table 2.1 gives the basic statistics for the 44 wells used in the study plus seven additional wells with checkshot velocity surveys through salt but lacking a mudlog to determine the mineralogy of the salt contents. The variability is striking in all categories.

Statistic:	Standard deviation	Mean value	Maximum value	Minimum value
Salt V_{int} in ft/s	744.8	15056	18535	14388
Salt V_{int} m/s	227	4583	5650	4386
Salt thickness in feet	5294	10947	21233	2270
Salt thickness in meters	1614	3337	6472	692
Halite %	12.85	89.54	100.00	42.51
Anhydrite %	19.47	15.03	57.49	0.07
Gypsum %	8.18	4.68	33.89	0.01
Sylvite %	7.99	9.27	22.13	0.02
Clastics or other %	1.00	0.78	3.62	0.02

Table 2.1. Statistics for salt velocities and salt thicknesses in 51 wells and the percentage of salt components in 44 wells.

2.3 SALT INTERVAL VELOCITIES vs. LATITUDE

In this chapter the term “surface-seismic” is used repeatedly and is meant to distinguish between seismic data acquired on the surface (sea level in this case) as opposed to borehole seismic acquisition. Near wells, I computed the surface-seismic interval velocities between the top and base of salt, using Kirchhoff pre-stack, time-migrated (PSTM) seismic-interval transit times, projected to borehole locations where the corresponding depths are known. These interval velocities are paired with the borehole salt-body V_{int}, also measured between the top and base of salt, using checkshot surveys, a VSP, or integrated sonic logs.

2.3.1. Surface seismic salt-body interval velocities versus interval velocities determined in boreholes

These velocities for the 18 wells close to a seismic line are shown in Table 2.2. Unfortunately, the data did not include both sonic log and borehole seismic velocities through the salt in the same well. Thus, there was no direct indication of dispersion between sonic and seismic frequencies. A crossplot of surface-seismic interval velocities vs. borehole seismic or sonic log interval velocities (Figure2.3) shows no obvious dispersion. The overall match between surface-seismic salt V_{int} and borehole salt V_{int} is reasonably good: less than 2% difference for ten wells, less than 4.8% difference for another five wells, two wells show ≈6% difference, and the one outlier well has a 15.43% difference. The outlier well is Mission Deep Field GC-955-002 that has a large amount of anhydrite at the base of its salt column, resulting in a VSP-measured salt-body interval velocity of 18,535 ft/s (5650 m/s). It is tempting to attribute the higher average wellbore measurements to body-wave dispersion; however, this is not a satisfying explanation because the difference between surface-seismic and wellbore velocities is similar for seismic frequency and sonic frequency borehole-velocity measurements. Although dispersion cannot be entirely ruled out as a possible explanation for this difference. Other factors, such as inexact picking of the top and base of salt on the surface-seismic, errors in projection, lateral variations from wellbore to seismic line, biases in seismic-processing velocities, geometric effects etc., could account for the discrepancy. For example, if the surface seismic ray-path length is not the same as the depth interval in the well, this could result in an extended travel-time in the salt-body, and thus a lower velocity. What is more significant is the areal variation in velocity as seen in Table 2.1, but especially when considering the wells close to seismic data (see Table2.2).

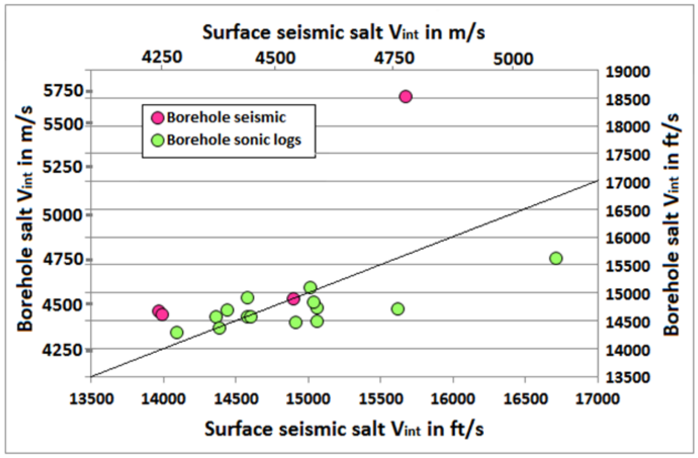

Figure 2.3. A crossplot of surface seismic interval velocities vs. borehole seismic or sonic-log interval velocities. The black line indicates borehole interval velocity equal to surface-seismic interval velocity.

Well name	API- UVI	Seismic top of salt (sec) TWT	Well top salt (ft) SRD	Seismic base of salt (sec) TWT	Well base salt (ft) SRD	Seismic salt V_{int} (ft/s)	Seismic salt V_{int} (m/s)	Well salt V_{int} (ft/s)	Well salt V_{int} (m/s)	% Difference
Green Canyon area										
GC-821-001	608114044800	1.7709	5024	3.3502	16052	**13966**	**4257**	**14669**	**4471**	**4.79**
GC 955-001	608114027100	4.2770	13136	4.3055	13341	**14362**	**4378**	**14582**	**4445**	**1.51**
GC-955-002	608114047700	4.9628	16238	5.3296	19113	**15675**	**4778**	**18535**	**5650**	**15.43**
Keathley Canyon area										
KC-57-001-ST1	608084004101	3.0740	7934	5.5090	26264	**15055**	**4589**	**14751**	**4496**	**-2.06**
KC 102-001	608084001500	3.1090	8410	5.3220	24905	**14907**	**4544**	**14475**	**4412**	**-2.98**
KC-292-001-ST2	608084001104	3.8123	10225	5.7797	24564	**14577**	**4443**	**14586**	**4446**	**0.06**
KC-292-001-BP1	608084001101	3.8123	10225	5.7797	24564	**14577**	**4443**	**14925**	**4549**	**2.33**
KC-292-002	608084001102	3.8134	10229	5.7742	24539	**14596**	**4449**	**14586**	**4446**	**-0.07**
KC-470-001	608054001900	4.8980	14695	5.9770	22795	**15014**	**4576**	**15107**	**4605**	**0.62**
KC-470-001	608054001900	5.9600	23275	6.0452	23875	**14085**	**4293**	**14292**	**4356**	**1.45**
KC-736-001	608084002200	3.0984	7808	5.0172	21608	**14384**	**4384**	**14384**	**4384**	**0.00**
KC-872-001	608084001600	3.2622	8216	4.7376	19306	**15033**	**4582**	**14850**	**4526**	**-1.23**
Sigsbee Escarpment area										
SE-39-001-BP2	608094000102	4.4400	9607	4.7547	12236	**16707**	**5092**	**15634**	**4765**	**-6.86**
Walker Ridge area										
WR-143-003	608124008900	4.0370	11383	5.8630	25128	**15054**	**4589**	**14493**	**4418**	**-3.87**
WR-316-001	608124003700	2.7380	6858	5.4830	25946	**13989**	**4264**	**14617**	**4455**	**4.30**
WR-543-001-BP	608124004501	3.7580	9614	5.8340	24602	**14439**	**4401**	**14706**	**4482**	**1.82**
WR-544-001	608124002100	3.6676	9816	5.5061	23510	**14897**	**4541**	**14893**	**4539**	**-0.03**
WR-627-001	608124002400	3.7876	10585	5.2174	21748	**15615**	**4760**	**14731**	**4490**	**-6.00**
standard deviation		0.9192	4011	0.7032	4315	**663.6**	**311.3**	**202.3**	**94.9**	**3.22**
mean value		3.7933	10738	5.3103	21894	**14780**	**4505**	**14722**	**4487**	**-0.37**

Table 2.2. Measurements of seismic salt-body V_{int} compared to borehole salt V_{int} and the percent differences. A positive percent difference means the borehole velocity is faster. The green color for well salt V_{int} indicates these are borehole seismic velocity measurements while

no color in this column indicates sonic log measurements. The outlier well (GC-955-002) was excluded in the calculations for standard deviation and mean value.

Figure 2.4 shows the quality of seismic in determining the seismic top and base of salt for the measurements gathered for Table 2.2. The line shown is strike line 2600 and the well measured for time at the top and base of salt is WR-143-003 (on the left). The neighboring well on the right, WR-143-001, stops at the top of salt.

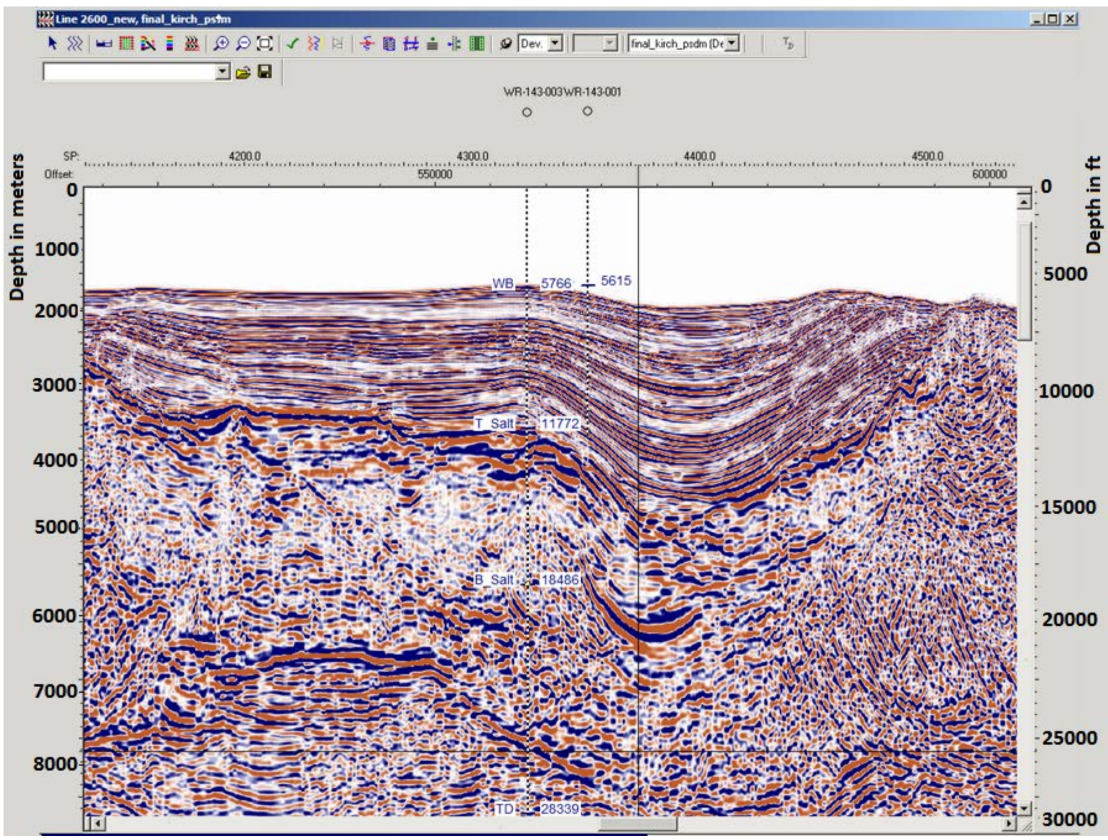

Figure 2.4. Two wells projected into seismic strike line 2600: WR-143-001 well TDs at top of salt (on the right) and the WR-143-003 well (on the left) penetrates the whole salt-body and ends in sediments below.

2.3.2 Salt-body interval velocity versus latitude

In the study area, there appears to be a general trend from south to north of decreasing salt-body interval velocity measured in wellbores with some important exceptions. Figure 2.5a shows the initial plot of the velocity information from the 18 wells and accompanying seismic data in Table 2.1 versus decimal latitude. The salt V_{int} starts on the left at the lowest latitude with Anadarko's Sigsbee Escarpment well SE-39-001-BP2 and goes to the furthest northern well in the study area, BP Exploration & Production's Green Canyon well GC-821-001. These 18 wells in the study area are close enough to the seismic data to be projected onto the seismic lines for the creation of synthetic seismograms. Where the symbol for the seismic salt V_{int} is not visible, it means that it coincides with the well data salt V_{int} to less than 0.4% difference. Based upon the suggestive trend in Figure 2.5a, the question became "What happens if all the measured salt-body interval velocities are added to the plot?" Those results are displayed in Figure 2.5b.

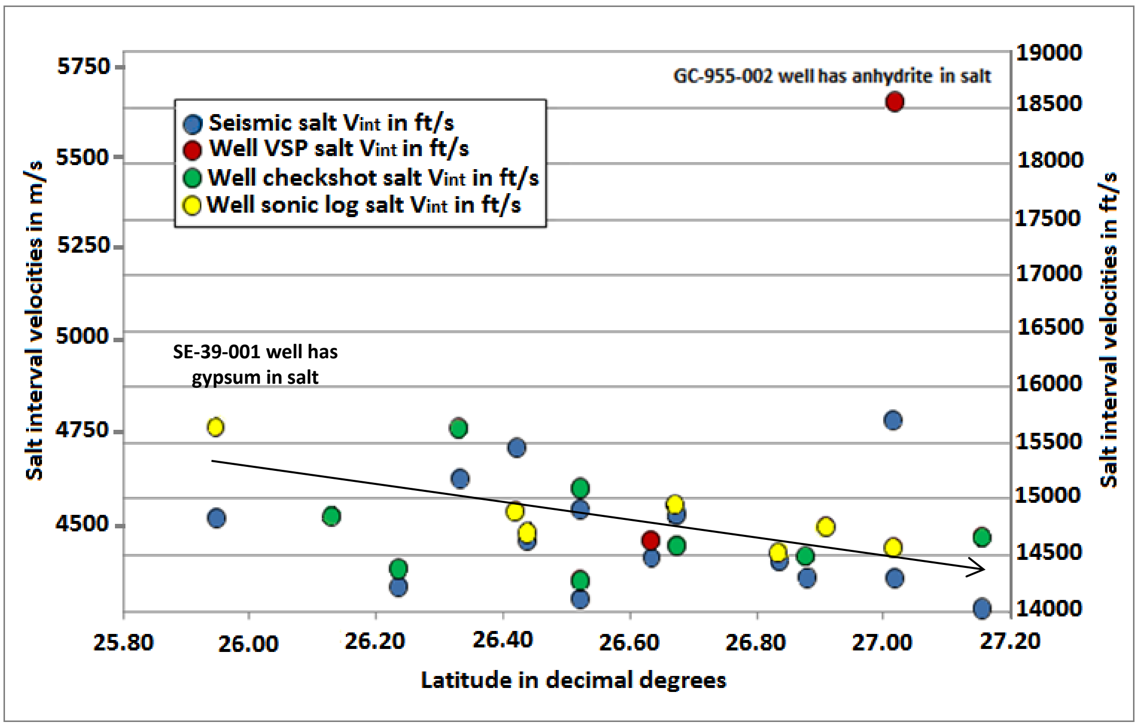

Figure 2.5a. Surface-seismic salt-body interval velocities and 18 borehole-derived salt-body interval velocities versus latitude in decimal degrees. There is a noticeable trend indicating decreasing V_{int} from south to north.

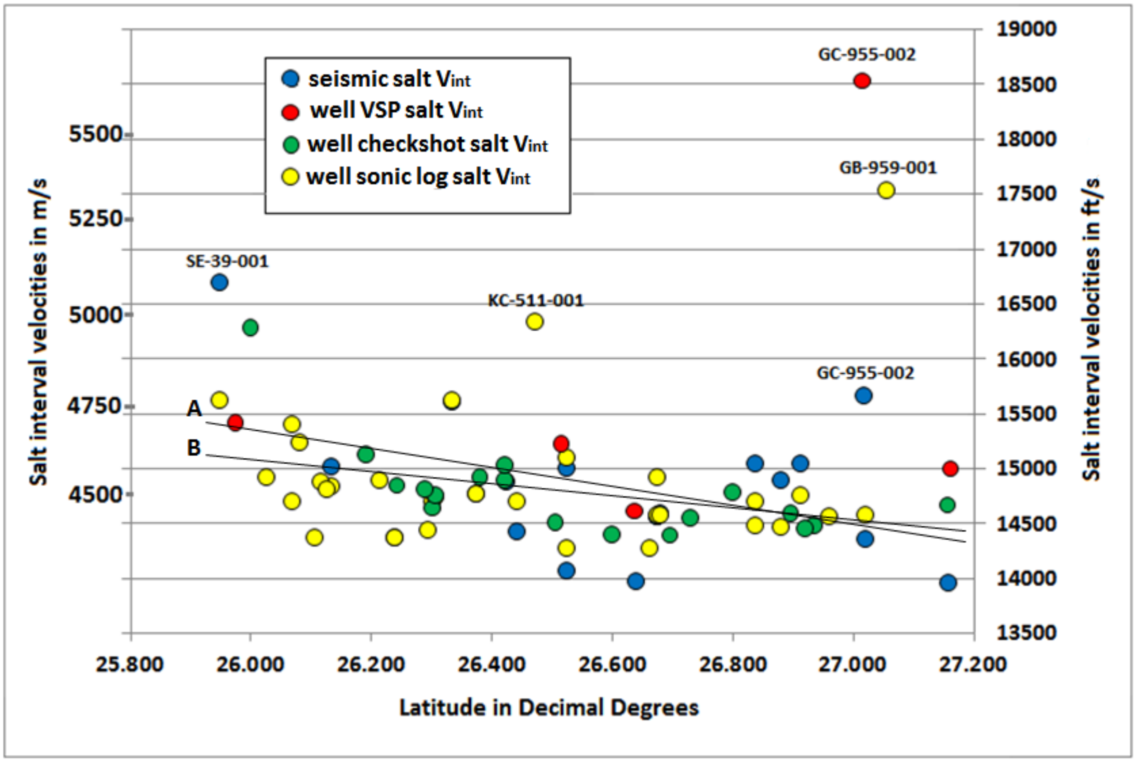

Figure 2.5b. Surface-seismic and borehole salt-body interval velocities in the study area vs. latitude in decimal degrees. The plot starts on the left at the lowest latitude with the Sigsbee Escarpment well SE-39-001-BP2 and goes to the furthest northern well in the study area, Green Canyon well GC-821-001. Well names are provided for outlier points. Regression line A is for surface-seismic velocities only and regression line B is for borehole velocities only. Both trends were computed less two outlier points: GC-955-002 and GB-959-001 where high velocities are associated with large amounts of anhydrite.

To understand why there is an overall trend of decreasing velocity with increasing latitude; and to understand the deviations from this trend, both the lithological and environmental factors that could influence the salt-body velocities must be considered. In other words, can the mineralogical variations within the salt matrix (or intercalated with halite) in the salt-body explain the velocity variations? In search of an answer the following questions arise: (1) What is the areal compositional variation of the salt-bodies?; (2) Can this observed compositional variation explain the variation in velocity?; and (3) Can other factors, such as depth, pressure, and temperature account for the variation? Each of these questions will be systematically investigated later in this chapter.

2.4 DISCUSSION OF LOUANN SALT

Table 2.1 showed the spread in variability of the salt-body velocities within the deepwater study area, so now I will investigate possible causes of this variability beginning with the first possibility of the salt composition itself...perhaps the composition of these salt-bodies is more complicated than simple halite in more than just a few already noted cases. Leg 96 of the Deepsea Drilling Program (DSDP) cored-salt samples in the deepwater GoM on this scientific expedition in 1983. Some core samples were distributed to various oil companies for evaluation and others were archived for future work. A brief attempt at trying to find out which oil companies had received samples from these salt cores for analysis did not produce any definitive answers. Samples were collected from ten different sites (DSDP web reference: http://www.deepseadrilling.org/96/dsdp_toc.htm).

2.4.1 Initial deposition of the Louann Salt

An important observation to keep in mind is that these interval velocities were measured in present-day allochthonous salt, not the original "in place" autochthonous salt. The time interval within which the Louann Salt was deposited is restricted to between 163 and 161 Ma (Hudec et al., 2013) and (Pindell and Kennan, 2007). See Figure 2.6a, which is a paleo reconstruction showing the limit of Louann Salt deposition and the position of the Yucatan block during the Middle Jurassic time period. The pink color denoting salt also denotes deposition on continental crust. Compare this to Figure 2.6b that shows deposition of parautochthonous salt shown in orange, deposited on transitional crust just before seafloor spreading began at 155 Ma, along with the separation of the salt into two units, one to the north and the other to the south. Figure 2.6c shows present day Louann Salt locations, relative to its original deposition, as far as location of the autochthonous salt. The location of present-day Louann Salt is better demonstrated in Figure 2.7 that illustrates the resultant basinward movement of the allochthonous salt over time.

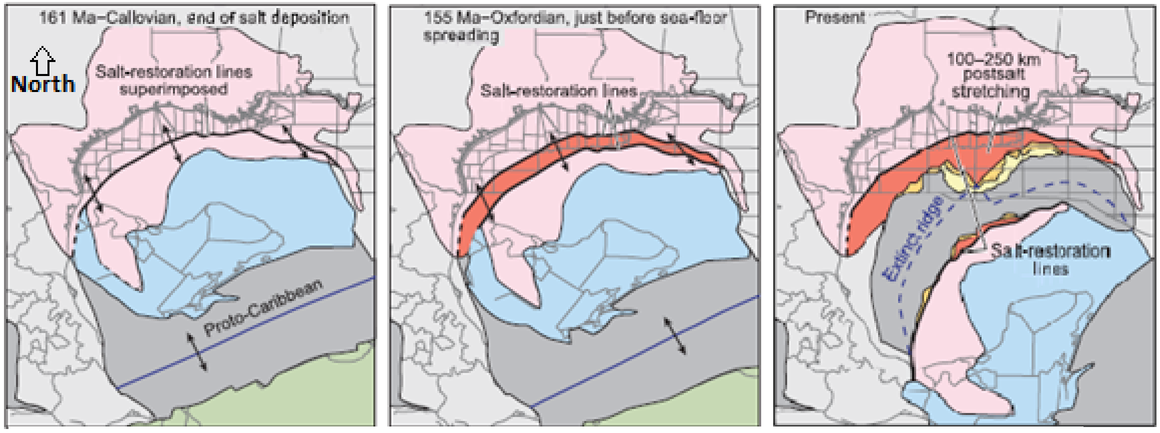

Figure 2.6a. Figure 2.6b. Figure 2.6c.

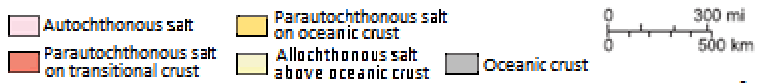

after Hudec, et al., 2013

Figure 2.6a. End of Louann Salt deposition, Figure 2.6b. Splitting of autochthonous salt and location of parautochthonous (shifted) salt after seafloor spreading initiated at 155 Ma, and Figure 2.6c. Present-day location of autochthonous salt.

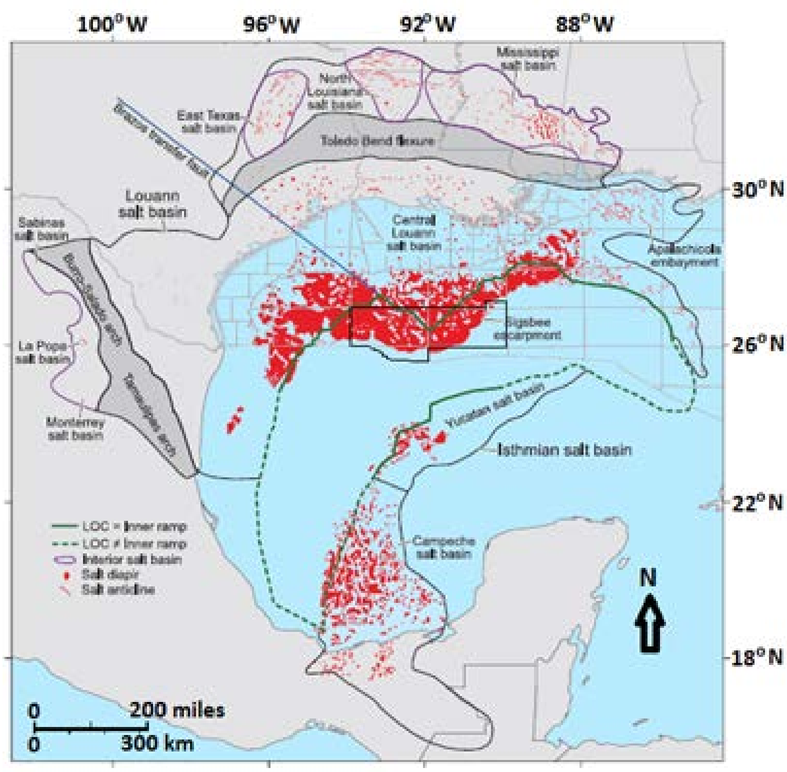

after Hudec et al., 2013

Figure 2.7. Present-day location of offshore allochthonous Louann Salt as it moves toward the center of the basin. Study area in Keathley Canyon, Walker Ridge, SE Green Canyon, and Sigsbee Escarpment is outlined with a black border. After Hudec et al., 2013.

2.4.2 Movement of Louann Salt basinward

The Louann salt has been moving ever since sediment loading commenced in the late Jurassic (Hunsdale, 2009), (Allwart, 2009), and (Hudec and Jackson, 2011). Crustal stretching and basin-center rifting began ca 155 Ma, splitting the Louann Salt basin into a northern component and a southern component as seen in Figure 2.6c. The cooling of the newly formed oceanic crust and exhumed upper mantle in the center of the basin caused a density increase that in turn caused the basin floor to sink. This basinward tilt allowed the severed salt blocks to flow towards the center of the basin, while simultaneously, sediments began to cover the new oceanic crust, ahead of the spreading salt. This sedimentation forced the base of the spreading salt to climb over the accumulating sediments and in the process build a basinward-climbing wedge of allochthonous salt at the end of the Jurassic and into the early Cretaceous. The wedge formed a fringe of salt at least 30 to 40 km wide during the Late Oligocene to Miocene beneath the Sigsbee Escarpment, between what are now the Mississippi Canyon and Keathley Canyon areas (Dribus et al., 2008) and (Rowan, 1995).

This was the first of several salt-sheet emplacements in the Gulf of Mexico basin. However, a more recent publication claims that in the northern Gulf of Mexico margin, salt has been flowing towards the southwest since the Cretaceous; and contrary to previous interpretations that invoked sedimentary loading as the main driving force of salt movement, analysis of salt flow on a regional basis indicates salt movement (or flow) is predominantly controlled by gliding perpendicularly over the Paleogene margin dip, which trends from northwest to southeast (Fort and Brun, 2012). See Figures 2.8a and 2.8b.

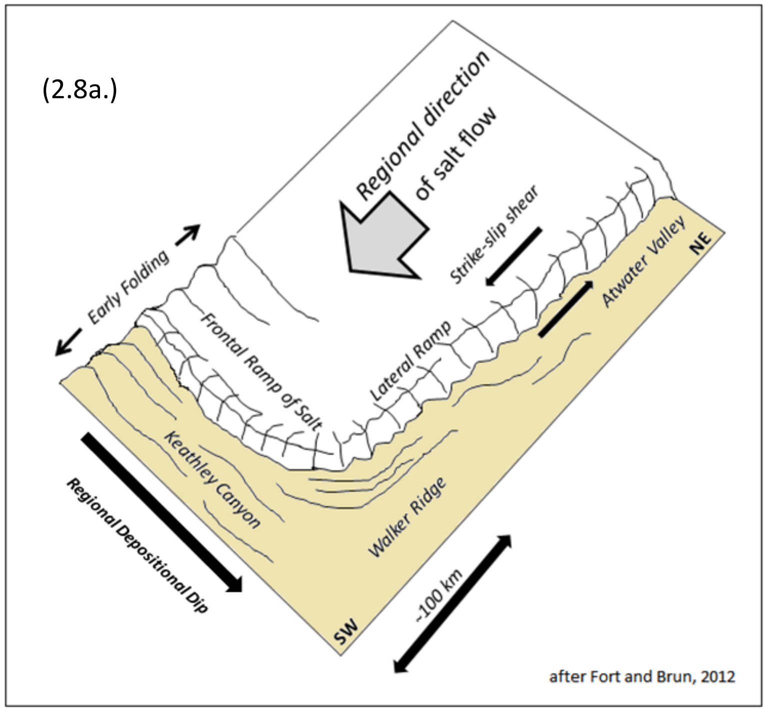

Figure 2.8a. A sketch diagram showing the relationship between contractions related to the Keathley Canyon frontal ramp and the en echelon folds and faults along the Walker Ridge-Atwater Valley lateral ramp, prior to the Middle Miocene.

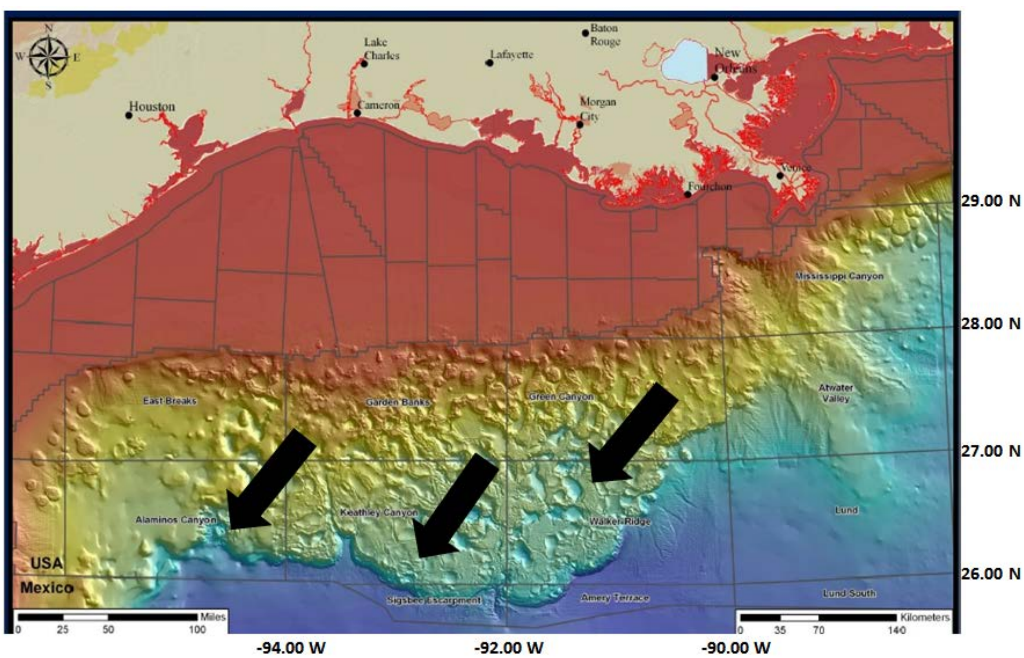

Figure 2.8b shows the proposed direction of salt flow as it moves basinward over sediments deposited from NW to SE (Fort and Brun, 2012). Base topographic map from GIS culture in 2014.

During the Cenozoic, the lower continental slope experienced folding driven by gravitationally-induced compression caused by the basinward slope of the seafloor. The Perdido fold belt in the Alaminos Canyon area formed on top of thick allochthonous salt in the Late Oligocene to Early Miocene. Further to the east, the Mississippi Fan fold belt formed on the deep wedge of allochthonous salt in the Atwater Valley area during the Late Miocene. In the area between these two fold belts, from Keathley Canyon to Walker Ridge, deep fold belts have not been observed because they are below the deepest part of the basin (Dribus et al., 2008). Seismic imaging, until recently, hasn't been able to adequately image below salt at such depths.

From the Miocene to the present, vast salt sheets spread laterally in all directions wherever salt supplies from the autochthonous base below were sufficient to feed their expansion. These sheets then coalesced to form shallow salt canopies. This massive spreading of salt was variable depending on the thickness of the local supply. In eastern Mississippi Canyon area, where the autochthonous salt was thin, only a few scattered small salt sheets were formed. In the Green Canyon area, where the autochthonous salt was much thicker, most salt diapirs merged into thick canopies. Further west from Walker Ridge to Alaminos Canyon, **where the basal salt was the thickest**, massive diapiric walls of salt fed a single giant canopy that spread southward for many tens of kilometers (Dribus, et al., 2008). A slightly different perspective is offered by Shaker (2010) due to his differentiation between "clean" versus "dirty" salt: he states a clean salt mass (pure halite) is usually driven downdip by gravitational buoyancy whereas dirty salt (halite with mineralogical or sediment intrusions) is pushed downdip by sediment influx, in addition to gravitational buoyancy. Occasionally, sediments intrude into the salt mass and are carried within as rafted blocks (Moore et al., 1995). Figure 2.8 shows strike line 2800 trending from southwest on the left to northeast on the right, beginning at the southwestern edge of the Sigsbee Escarpment and crossing diagonally through Walker Ridge to the northeasterly edge of the Sigsbee Escarpment. Note the apparent small floating "islands" of salt on either end at the edge of the escarpment. Both of them probably have a dip component not seen in this strike view. The study area is literally in the area of thickest allochthonous salt. The Sigsbee Escarpment is the largest exposed salt structure in the world, reaching a height of 4100 feet (1250 m) and has an exposed horizontal expanse of about 350 miles (560 km). The buried part of the Sigsbee Escarpment has a length of more than 620 miles (1000 km). Today the salt canopies continue to advance basinward over about 60% of the escarpment, gradually obscuring much of the subsalt geology (Dribus, et al., 2008). The autochthonous Louann Salt is currently at ≈40,000 feet as shown in Figure 2.9 where the dark green color (V_{int} ≈15,000 ft/s) also represents the shallower salt canopy at depths from 10,000 to 35,000 ft.

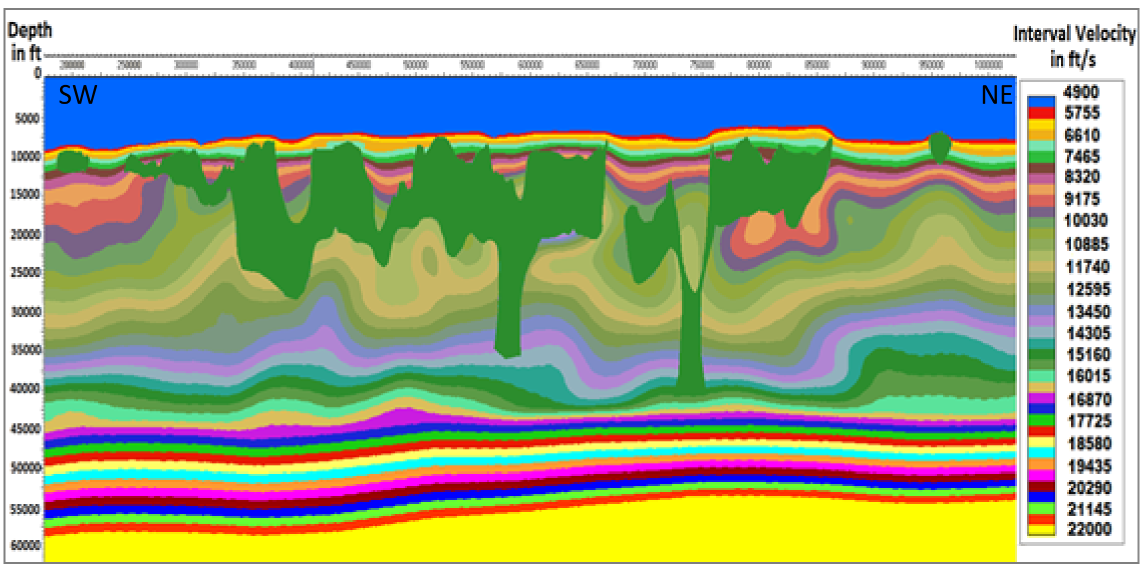

Figure 2.9. Seismic interval velocity vs. depth in feet for strike line 2800. Depth axis is from 0 to 65,000 ft and Vint from 4900 to 22,000 ft/s. This seismic line crosses the Sigsbee Escarpment twice: once on the SW end and again on the NE end.

It is difficult to estimate the rate of salt movement over geologic time due to various events that effect gravity sliding of the salt basinward. A geologically recent rate of basinward movement has been suggested by Hudec and Jackson (2011) and demonstrated in Figure 2.10a for the Mad Dog Field area in Green Canyon, block 825. They estimate that the salt has moved basinward 4.2 miles (6.8 km) over the past 2 million years. Note that Mad Dog Field is currently at the edge of the Sigsbee Escarpment as shown in the walkway VSP in Figure 2.10b.

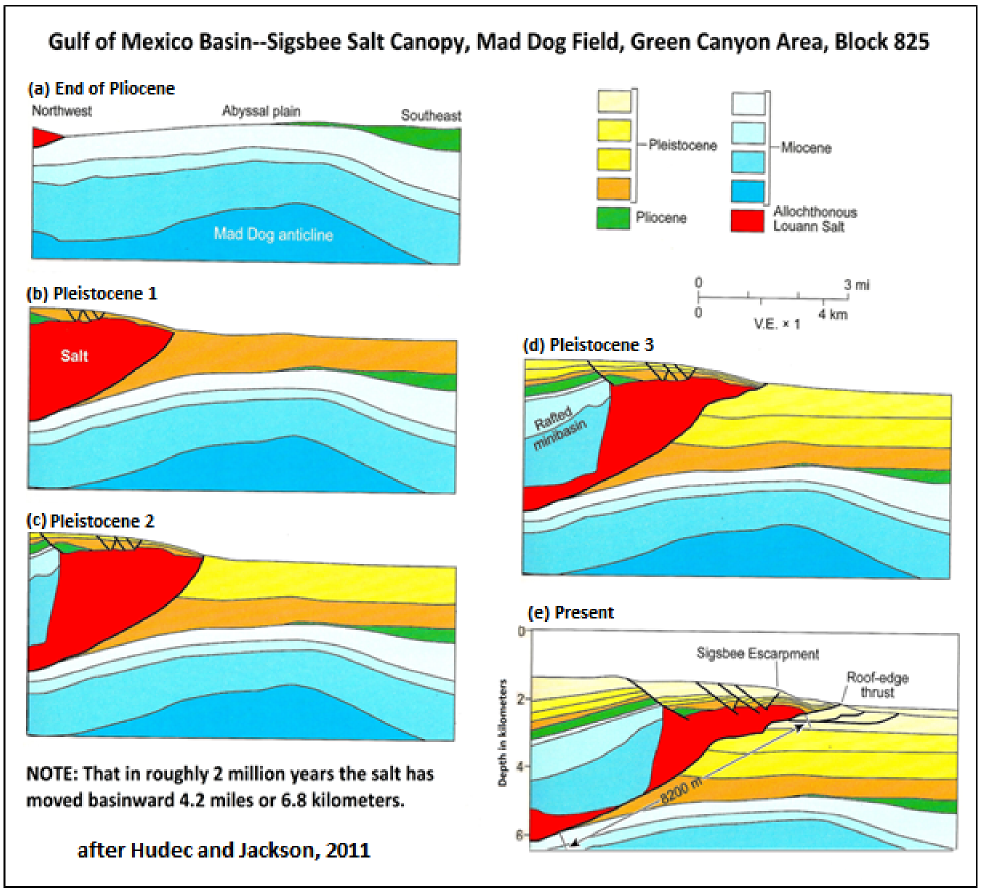

Figure 2.10a. Thrust advance of a salt canopy. During the Pliocene the salt may have advanced by extrusion, and if it did so, it moved basinward 4.2 miles or 6.8 km over 2 Ma.

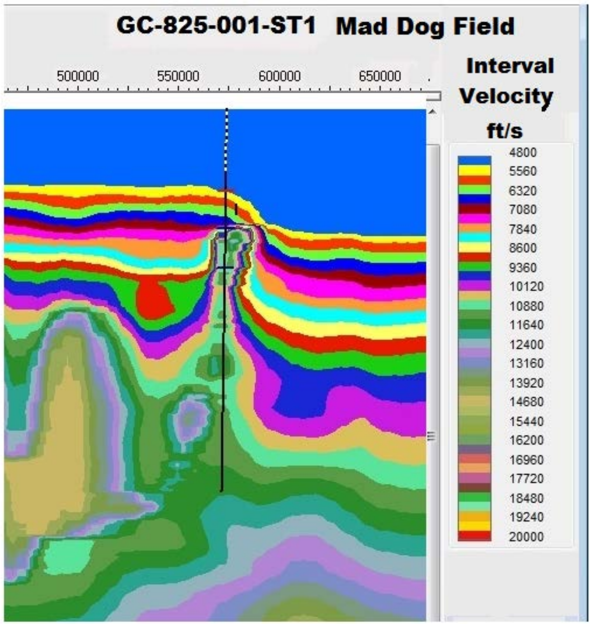

Figure 2.10b. SEGY display of a walkaway VSP over Mad Dog Field along depositional dip of the Wilcox formation (NW to SE). The field is on the edge of the Sigsbee Escarpment. This image is truncated at 30,000 feet vertically but has the same 40 random-color colorbar as the other seismic-interval velocity displays.

2.5 MINERALOGICAL COMPONENTS WITHIN THE SALT BY LATITUDINAL AREA

The study area has been divided into five different sections geographically based more or less on latitude and the interval velocities for the salt-bodies found within that section. A summary for the group of wells within each section is presented in the following tables, which have been color-coded to correspond to the map in Figure 2.16. The standard borehole values for halite compressional and shear velocities under borehole conditions are given by 14,763 ft/sec (4,500 meters/sec) and 8,005 ft/sec (2,440 meters/sec) respectively, as shown in Figure 2.11. When reading the mud-logs, gypsum is never mentioned as a component, its presence is denoted by the amount of yellow fluorescence observed under ultraviolet light (Figures 2.12a-d). Manganese and iron exhibit a bright orange to red fluorescence in halite, but these are not encountered in marine samples, only from specific locations in the world, usually originating from dried up lake beds (Murata and Smith, 1946). The fluorescence description is very subjective: one person's “dull yellow” is another person's “pale yellow”, and as such introduces uncertainty into the estimated volume present. However, the description is very important because it directly translates into a rough percentage of the gypsum present.

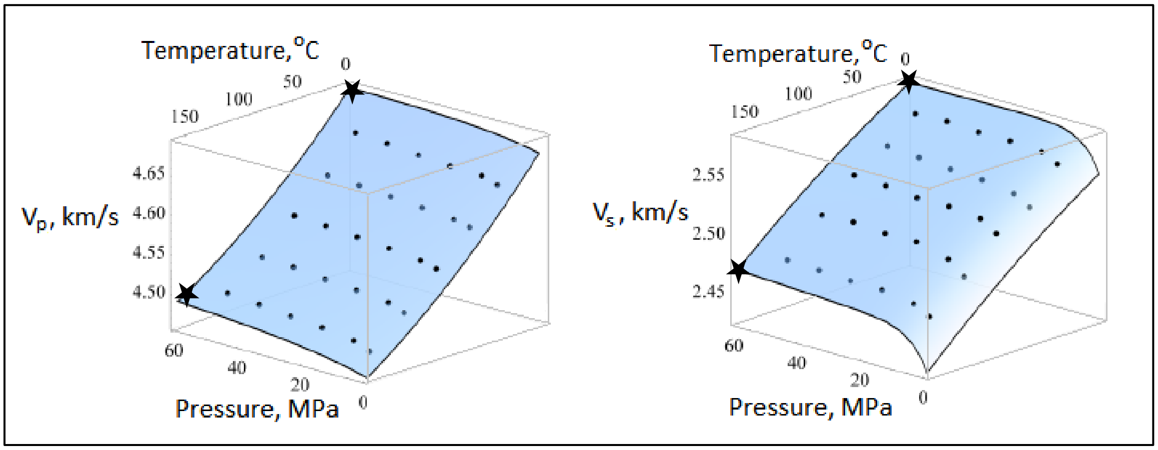

Figure 2.11. Temperature and pressure effects on halite velocities under borehole conditions. After Yan et al., 2014 SEG annual meeting.

Figure 2.12a.

Figure 2.12b.

Figure 2.12c.

Figure 2.12d.

Figure 2.12a shows a sample of halite and gypsum in ordinary light, both are white to clear and crystalline. In Figure 2.12b is a similar sample under UV light and the gypsum exhibits a "pale or dull yellow" fluorescence, indicating a few percent (3% to 5%) gypsum present. Figure 2.12c exhibits a "bright yellow" fluorescence indicating about 10% to 20% gypsum present and Figure 2.12d shows a "strong yellow" fluorescence indicating 40% or more presence of gypsum. (Images from www.galleries.com/minerals /property/ fluorescence.htm). These are semi-quantitative measurements of percentage content because the amount or the intensity of fluorescence of gypsum can vary with temperature, as well as the subjective descriptions by the mudlogger. Gypsum is one of the minerals that exhibit a slight fluorescence at room temperature but that intensity will increase significantly as the temperature decreases to -50°C (McDougall, 1952). One hopes that these mudlog observations were made over a relatively short time span not experiencing drastic temperature fluctuations, such that they are correct relative to each other. There is a way to quantify the fluorescence signal emitted that is used in molecular/cellular biology called fluorescent microscopy. However, it is used on microscopic-sized samples and hasn't been used in mudlogging, at least to my knowledge (http://faculty.jsd.claremont.edu.jarmstrong/fquant/).

The following five tables give the detailed descriptions of the salt components from the mudlogs and the depth of their occurrence. The measured salt V_{int} is presented in a black font and the estimated salt V_{int} is in a red font. Some of these wells have been recently drilled, and as such, their velocity information is not yet available. In these instances, the salt V_{int} has been estimated from the volume fractions of its components.

Table 2.3 displays the eight southernmost wells having mudlog descriptions of the salt and velocity information through the salt. These wells form Group 1. The one exception is the fairly recent well KC-953-001, which has not yet had any sonic information made public; so its salt V_{int} was estimated based upon its salt constituents described in the lower 92% of the salt column. If and when sonic logs or a checkshot survey for this well are released, it is possible that the estimated velocity could be in error due to unknown constituents in the upper 8% of the salt column. This holds true for all other wells in the study area where the mudlogs start below the top of salt and no sonic information is currently available. Note that the salt V_{int} values for Group 1 are considerably higher than for pure halite due to the presence of gypsum, along with traces of pyrite and the rare anhydrite clusters found in the salt of WR-969-001. The measured salt V_{int} for Group 1 varies between 14,925 ft/s (4549 m/s) and 16,289 ft/s (4965 m/s).

Moving northward, Table 2.4 displays seventeen wells of the second group having salt V_{int} less than 15,000 ft/s (4572m/s) but typically more than the pure halite value of 14763 ft/s (4500m/s). These wells form Group 2, where the amount of gypsum is less than in the wells of Group 1, but still present, along with traces of pyrite and sylvite. Group 2 wells have larger sediment intrusions of shale and clay. Three wells in this group have estimated salt V_{int} due to lack of any sonic measurements in the salt-body. In the WR-848-001 well approximately 260 ft

(79 m) of salt coming out of the borehole was stained a bright yellow. Could this possibly be due to the presence of sulphur, even though there is no mention of it in the mudlog? Most accumulations of the mineral sulfur found in the subsurface are associated with evaporite minerals where gypsum and anhydrite produce native sulfur as a product of bacterial action (http://geology.com/minerals/sulfur.shtml).

Table 2.5 has 13 wells with salt V_{int} fairly close to the average halite value of around 14,763 ft/s (4500 m/s) and they form salt Group 3. Some of the wells in this group display oil stains, tar, and dead oil within the salt-body, which definitely suggests these were incorporated into the salt matrix during salt movement, because it is not geologically possible for these components to have been part of the original salt deposition. Sediment intrusions are more pronounced and more varied, including sandstone, chert, lignite, siltstone, shale, and calcareous claystone within the salt-bodies.

Going still further north, Group 4 contains twelve wells, shown in Table 2.6. These wells exhibit salt V_{int} less than the expected halite value. The gypsum content has been diminished to only traces of dull yellow fluorescence, while the halite has traces of bitumen with noticeable amounts of both claystone and sylvite. The WR-70-001 well has traces of soft anhydrite over a 9,500 ft (2896 meters) span in the borehole; but since soft anhydrite has a similar compressional velocity to halite, its presence doesn't increase the salt V_{int} (Bell, 1981) and (Takahashi and Tanaka, 2009). Regular anhydrite is crystalline; but soft anhydrite can be fragmented, granular or nodular, depending on the amount of re-sedimentation down slope and the energy of the transport process (Rouchy et al., 1995).

Table 2.7 includes four of the northernmost wells and two anomalous wells from the mid-latitude, combined to form Group 5. The salt V_{int} in Group 5 increases to the highest value of any group due to a significant presence of anhydrite. In general, this is not a separate anhydrite cap on top of salt as seen onshore and in shallower-water salt diapirs; this anhydrite is usually mixed within the salt matrix. Salt V_{int} in Group 5 wells varies from 15,000 ft/s (4572 m/s) to as high as 18,535 ft/s (5650 m/s) in the GC-955-002 well, which does have a VSP survey confirming this velocity. Sylvite, which tends to lower the V_{int}, is noticeably present in this group of six wells; but this potential decrease in velocity is more than compensated for by the larger amounts of anhydrite.

Well name	Dec Latitude	Depth interval of flourescence	Flourescence color exhibited	Mineral present	Mineral Vp in ft/s	Salt interval velocity ft/s
SE-39-001-BP2	25.947	11500-12350	tr. Yellow	Gypsum	17044	15634
WR-970-001	25.974	13200-14280	(dull) Yellow	Gypsum	17044	15422
		15450-15540	(dull) Yellow	Gypsum	17044	
WR-969-001	25.999	15800-17700	NA	traces of Anhydrite clusters	21023	16289
		17000-17100	(strong) Yellow	Gypsum	17044	
KC-963-001-ST1	26.025	12680-13597		none mentioned		14925
			comment that salt is very hard indicating presence of			
			either anhydrite, calcite or some denser mineral			
KC-953-001	26.049	9898-10474		No mudlog data		14882
		11050-11080	NA	calcareous claystone	10200	estimated
		13700-14000	pale Yellow	Gypsum	17044	
		14570-14730	pale-Yellow-gold	Gypsum	17044	
KC-919-002	26.066	12920-13150	NA	tr. Pyrite + tr. limestone	26575 variable	15416
		13150-13350	NA	tr. SLTST + tr. CLST		
		13350-13450	NA	tr. Pyrite	26575	
		13550-13900	(pale) Yellow	Gypsum	17044	
		14200-14250	20% strong Yellow	Gypsum	17044	
		14250-14350	Yellow	Gypsum	17044	
		14600-14950	30% strong Yellow	Gypsum	17044	
		14950-15250	20% strong Yellow	Gypsum	17044	
		15450-15950	scat. strong Yellow	Gypsum	17044	
KC-918-00-ST1	26.080	12850-13350	NA	traces brn and gry limestone + marl	variable	15815
		13750-13840	NA	12.5% dk gry marl	8202	
		14110-14200	NA	12.5% black marl	8202	
		14750-15220 15470-16470	(dull) Yellow	Gypsum	17044	
KC-919-003-BP1	26.100	12269-13800	NA	Halite w minor tr shale		15734
		13800-14200	tr bright Yellow	Gypsum	17044	
		14360-14600	tr bright Yellow	Gypsum	17044	
		15553-18790	NA	mixed sediments		
		18790-19000	NA	Halite resumes	14760	
		19000-19628	NA	Both Sylvite & Anhydrite present	12880 21023	

Table 2.3. Mudlog description of components within salt Group 1. in the far south of the project area where gypsum is the secondary salt component.

Well name	Dec Latitude	Depth interval of flourescence	Flourescence color exhibited	Mineral present	Mineral's Vp in ft/s	Salt interval velocity ft/s
WR-793-ss001	26.092	9570-19020	NA	Halite	14760	14760
		50 ft of	white fluorescence	Calcite	20423	
KC-875-002	26.107	12022-12190	NA	only Halite	14760	No data
		12190-12310	NA	shale + trace tar	9800	14745
		15510-15630	NA	5% shale	9800	estimated
		15630-16038	NA	only Halite	14760	
KC-875-001-ST1	26.113	12030-17120	none mentioned			14892
			comments that salt is very hard indicating presence			
			of either anhydrite, calcite or some denser mineral			
WR-848-001	26.130	10034-10650	no mudlog data for first 616 ft of salt			No data
		10850-10890	bright Yellow	Gypsum	17044	14910
		11100-11280	NA	Salt has bright Yellow residue	14760	estimated sonic logs
		11760-11840	NA	Salt has bright Yellow residue	14760	below salt only
		12340-12360	NA	tr Pyrite + dead oil	26575	
		12780-12830	dull Yellow	Gypsum	17044	
		12960-13330	NA	reddish Fe stains		
		13560-13680	NA	10% Clay intrusion	9500	
		17950-18050	NA	7% Marl intrusion	8200	
		19550-19750	dull Yellow	Gypsum	17044	
KC-872-001-BP1	26.133	9300-13560	No fluorescence	only Halite	14760	14850
		13560-13860	Pale Yellow	Gypsum	17044	
		13860-19410	No fluorescence	only Halite	14760	
WR-758-PS005	26.207	11050-11250	dull Yellow	Gypsum	17044	No data
		12280-12300	NA	10% SLST intrusion	9600	14746
		14650-14700	dull Yellow	Gypsum	17044	estimated
		15400-15550	NA	moderate oil stains		
		17640-17800	NA	15% SLST intrusion	9600	
		17950-18050	NA	7% Marl intrusion	8200	
		19550-19750	dull Yellow	Gypsum	17044	
WR-758-002	26.208	10075-12410	NA	only Halite	14760	14815
		12410-12440	pale Yellow-green	Gypsum	17044	
		12980-14340	NA	Interbedded Sylvite	12880	
		14750-14980	pale Yellow-green	Gypsum	17044	
		15000-15120	NA	dk brown oil stains		
		15240-15960	Yellow	Gypsum	17044	
		16890-16915	NA	60% Shale intrusion		
		17475-17700	pale Yellow-green	Gypsum dk brown oil stains traces Sylvite	17044 ------- 12880	
		18340-18400	NA	traces calc. Shale	9600	
		19800-19990	pale Yellow-green	Gypsum	18701	
WR-759-001-BP1	26.213	No mudlog--salt Vint from a checkshot survey				14909

Table 2.4a. Southern part of Group 2 area. These wells show primarily gypsum inclusions with some sediments and occasionally small amounts of sylvite in their salt matrices.

Table 2.4 continued.

Well name	Dec Latitude	Depth interval of flourescence	Flourescence color exhibited	Mineral present	Mineral's Vp in ft/s	Salt interval velocity ft/s
KC-736-001	26.236	8810-8915	NA	10% Claystone	9500	14782
		8810-21720	No fluorescence	Halite only	14760	
WR-724-001	26.242	No mudlog--salt Vint from a checkshot survey				14837
WR-678-001-BP1	26.289	No mudlog--salt Vint from sonic log				15034
WR-678-002	26.292	No mudlog--salt Vint from a VSP				14815
WR-677-001	26.299	Mudlogged only below salt--salt Vint from sonic log				14722
KC-681-001	26.300	No mudlog data above 9780 ft-- salt Vint taken from checkshot survey				14740
		10080-10100	trace fluorescence	Gypsum	17044	
		16200		oil stain		
		16550	trace fluorescence	Gypsum	17044	
		16900-16985	NA	20% shale	9800	
		17325	trace fluorescence	Gypsum	17044	
		18450	trace fluorescence	Gypsum	17044	
WR-674-001	26.305	11600-12580	No fluorescence	Halite only	14760	14752
		12580-12960	trace Yellow	Gypsum	17044	
		12960-19250	No fluorescence	Halite only	14760	
KC-698-001	26.309	8270-9050	No mudlog data for upper salt			No data
		9300-10970	pale Yellow	Gypsum	17044	14870
		11630-11950	pale Yellow + trace dead oil	Gypsum	17044	estimated
		12700-12890	NA	tr Anhydrite ft/sec	21023	
		16210-16310	dull Yellow	Gypsum	17044	
		17030-17250	pale Yellow	Gypsum	17044	
		18670-18740	NA	tr Anhydrite	21023	
		19060-19090	NA	all Anhydrite, mixed soft to hard texture	variable	
		20490-21000	NA	tr Anhydrite + tar	21023	
		21300-22800	NA	tr Anhydrite + tar	21023	
		23120-23200	NA	tr Anhydrite + dead oil	21023	
WR-627-001	26.333	10300--10660	No mudlog data for upper salt			14731
		10660-21798	No flourescence	Halite only	14760	

Table 2.4b. Northern part of Group 2 area. Mudlog description of components in salt Group 2. These wells transition from traces of gypsum to traces of anhydrite going northward.

Well name	Dec Latitude	Depth interval of flourescence	Flourescence color exhibited	Mineral present	Mineral's Vp in ft/s	Salt interval velocity ft/s
KC-596-001	26.371	Mudlog not in dataset--salt V_{int} taken from checkshot survey				14780
WR-581-001	26.380	8700-9080	No mudlog data			14706
		8700-20400	Halite only reported but fluorescence wasn't measured?			
		20400-20525	NA	44% Claystone		
		20550-20605	NA	44% Claystone		
		20605-20900	NA	10% Claystone		
		21730-21750	NA	30% Shale		
		23805-24000	NA	18% Marl		
		24000-24100	NA	63% Marl		
WR-543-001-BP1	26.441	9716-10300	NA	No mudlog data		14779
		10570-11920	NA	traces Lignite	8200	
		16375-16665	Yellow fluorescence	Gypsum +tr siltstone	18701	
		17860	NA	tr marl, chert, tar	8200	
		24340-24399	NA	trace tar	4921	
WR-584-WR001	26.384	12350-13300	NA	tr Shale + dead oil	9800	14780
		13540-13570	NA	abundant Tar	4161	
		16480-16750	NA	tr Shale and tr Tar		
		16870-16800	dull Yellow residual	Gypsum	17044	
		19760-19770	NA	tr Sylvite	12880	
		21150-21200	dull pale Yellow	Gypsum	17044	
		21250-21350	NA	Salt impregnated 2-5% with dead oil	------	
WR-460-001	26.519	10270-10330	NA	Anhydrite inclusions	21023	14925
		10810-11470	NA	Anhydrite inclusions	21023	14942
		12010-13091	NA	Anhydrite inclusions	21023	estimated
		13690	NA	Anhydrite inclusions	21023	
		13990-14170	NA	Anhydrite inclusions	21023	
		14530-14590	NA	trace siltstone	9600	
		16150-16270	trace Yellow	Gypsum	17044	
		17050	trace Yellow	Gypsum	17044	
KC-414-001	26.570	8445-9290	No mudlog data			14880
		9290-13440	patchy dull yellow-gold	Gypsum	17044	estimated
		13440-14700	constant pale yellow	Gypsum	17044	sonic logs
		15150-16400	trace pale yellow	Gypsum	17044	below salt
		16030-16040	NA	all Sylvite	12880	only
		17880-18150	trace pale yellow	Gypsum	17044	
		18170	NA	more Sylvite	12880	
WR-372-001	26.599	8140-8870	No mudlog data	In salt		14755
		8870-19300	No fluorescence	Halite only	14760	
		19243-19300	NA	10% Shale intrusion	9800	
WR-316-001	26.636	6950-8360	No mudlog data	In salt		14745
		8600-10450	trace dull Yellow	Gypsum	17044	from VSP
		11300-11650	NA	tr Shale inclusion	9800	
		12450-13450	trace dull Yellow	Gypsum	17044	
		13450-13480	NA	tr amber Sandstone	10498	
		13480-13505	NA	tr Shale inclusion	9800	
		13610-14000	trace dull Yellow	Gypsum	17044	
		17300	NA	tr soft granular Halite	14700	
		22400-22600	trace dull Yellow	Gypsum	17044	
		23600-24800	NA	brown opaque Halite	14700	
		25860-25920	NA	40% Shale inclusion	9800	

Table 2.5a. Mudlog description of salt components in southern part of mid-latitude Group 3.

Table 2.5 continued.

Well name	Dec Latitude	Depth interval of flourescence	Flourescence color exhibited	Mineral present	Mineral's Vp in ft/sec	Salt interval velocity ft/sec
WR-278-001	26.661					14836
		13220-13370	Yellowish-green	Gypsum	17044	
		13520-13790	Yellowish-green	Gypsum	17044	
		14030-14180	5% Yellowish-green	Gypsum	17044	
		14300-14510	19.2 % Yellowish-green	Gypsum	17044	
		19535-19990	trace fluorescence	Gypsum	17044	
		22210-24970	salt turns a very pale orange -» algae present when salt deposited			
KC-292-001-BP1	26.673	10300-10530	NA	only Halite	14760	14925
		10530-10650	NA	10% siltstone	9600	from sonic
		11320-11370	NA	15% shale	9800	log in lower
		12730-12910	NA	22% sand	10498	salt
		14930-15000	NA	15% vfg quartz sand	10498	14733
		15110-15220	NA	15% vfg quartz sand	10498	calculated
		16200-16350	Bright Yellow	Gypsum	17044	from
		16350-16650	Tr dull yellowish white	Gypsum	17044	components
		16900-17170	Tr dull yellowish white	Gypsum + tr dead oil	17044	
		17750-17950	NA	20% sand	10498	
		17860-17950	NA	25% shale	9800	
KC-292-002-BP1	26.677	11020-11800	NA	only Halite	14763	14815
		11800	moderate fluorescence	Gypsum	170544	
		13050-13250	trace dull yellow + traces of oil stains	Gypsum	170544	
		13550-13850	traces dull yellow	Gypsum	17044	
		14600-14900	traces dull yellow	Gypsum	17044	
		15800	traces dull yellow	Gypsum	17044	
		16330-17520	traces dull yellow	Gypsum	17044	
		18020-18080	traces dull yellow	Gypsum	17044	
		18560-18580	traces bright yellow	Gypsum	17044	
		18580-18920	traces dull yellow + traces clay in mixture	Gypsum Claystone	17044 9500	
		19030-19260	traces dull yellow	Gypsum	17044	
		20130-20240	traces dull yellow	Gypsum	17044	
		20425-20475	NA	calcareous Claystone	9800	
		20500-20830	traces dull yellow	Gypsum	17045	
		21080-21120	NA	trace Claystone	9500	
		22865-22885	NA	20% Claystone	9500	
		23020-23080	NA	8% Claystone	9500	
		24600-24750	traces bright yellow	Gypsum	17044	
		24850-25050	traces dull yellow + 15% black stains with burnt tar odor	Gypsum Tar	17044 4921	
KC-291-001	26.699	Mudlog is in unreadable format but GR & Res logs show lots of small				14706
		sediment intrusions in salt that are either shale, siltstone or claystone				

Table 2.5b. Mudlog description of salt components in northern part of mid-latitude Group 3. Gypsum is still present in some of these wells and sediments are a noticeable part of the salt matrix in KC-292-001-BP1 and in KC-291-001, both blocks in the Kaskida Field.

Table 2.5 continued.

Well name	Dec Latitude	Depth interval of flourescence	Flourescence color exhibited	Mineral present	Mineral Vp in ft/s	Salt interval velocity ft/s
WR-95-001	26.863	7060-8680	NA	only Halite		14980
		8680-9040	trace fluorescence	Gypsum	17044	14965
		10570-14620	Some fluorescence	Gypsum	17044	estimated
		16600-17320	avg 11.5% faint yellow	Gypsum	17044	
		17950-20200	avg 12.2% faint yellow	Gypsum	17044	
		20200-21870	avg 14.7% yellow	Gypsum	17044	
		21870-22500	trace fluorescence	Gypsum	17044	
		22590-23310	avg 11.9% yellow	Gypsum	17044	
	NOTE: most of the whole salt column showed traces of hydrocarbons stains					

Table 2.5c. Mudlog description of salt components in northernmost part of mid-latitude Group 3. This well is located in the Shenandoah sub-basin and still contains small amounts of gypsum.

Well name	Dec Latitude	Depth interval of flourescence	Flourescence color exhibited	Mineral present	Mineral Vp in ft/s	Salt interval velocity ft/s
KC-244-001-ST1	26.729	8200-10400	No fluorescence			14549
		10400-10750	trace dull Yellow	Gypsum	17044	
		10750-14750	No fluorescence			
		16900-17200	No fluorescence	Halite changes color from white		
				to yellowish to pale pink (or maybe Sylvite)		
WR-155-001-ST1	26.799	11038-18320	No flourescence			14388
		12230-12250	NA	16% calcareous Shale	9800	
		18170-18220	NA	oil stains in Salt		
		18320-18470	trace dull Yellow	Gypsum	17044	
		18780-18870	trace dull Yellow	Gypsum	17044	
		19590-19770	trace dull Yellow	Gypsum	17044	
		20300-21500	trace dull Yellow	Gypsum	17044	
WR-143-003	26.836	12280-12600	trace fluorescence	Gypsum	17044	14706
		13180-13700	trace fluorescence	Gypsum	17044	
		14780-16800	trace fluorescence	Gypsum	17044	
		17450-17585	NA	100% Silty Claystone	9500	
		17450-17585	NA	100% Silty Claystone	9500	
		18420-18650	NA	100% Silty Claystone	9500	
		18740-18820	NA	37% Silty Claystone	9500	
		18850-19540	NA	16% Silty Claystone	9500	
		20205-20445	NA	10% Silty Claystone	9500	
		20750-20800	NA	20% Silty Claystone	9500	
		22050-22160	NA	50% Silty Claystone	9500	
WR-96-001-BP1	26.873	5856-8380	No mudlog data until 8380 ft			14706
		8380-10550	NA	noticeable tar presence		estimated
		9460-9950	NA	aver. 10% Claystone	9500	sonic logs
		11450-14100	NA	noticeable tar presence	4921	below salt
		21300-21750	NA	heavy oil staining		
		21300-21750	NA	rusty-colored Halite inclusions ??		
		22000-22030	NA	50% Claystone	9500	
		22750-22800	slightly Yellow	Gypsum	17044	
		23450-23790	NA	aver. 50% Claystone	9500	

Table 2.6a. Mudlog description of various components within salt in the southern part of northerly Group 4.

Table 2.6 continued.

Well name	Dec Latitude	Depth interval of flourescence	Flourescence color exhibited	Mineral present	Mineral Vp in ft/s	Salt interval velocity ft/s
KC 102-001	26.878	8485-8650	NA			14475
		8650-9250	tr medium Yellow	Gypsum	17044	
		9500-9750	trace dull Yellow	Gypsum	17044	
		15600-19900	NA			
		19900-20100	tr dull pale Yellow	Gypsum	17044	
		20100-24980	NA			
WR-70-001	26.895	8400-17950	NA	traces soft Anhydrite	similar to	14595
		17950-18980	NA			
KC-57-001	26.909	8250-13950	trace Yellow	Gypsum	17044	14760
		10450-11950	No fluorescence	tr bitumen	8200	
		13850-13950	No fluorescence	trace SYLVITE	12880	
		15250-15650	No fluorescence	trace SYLVITE	12880	
		15700-19400	trace Yellow	Gypsum	17044	
		19450-20200	No fluorescence	tr bitumen	8200	
WR-52-001-BP2	26.920	8500-9200	trace dull Yellow	Gypsum	17044	14459
		9600-10000	trace dull Yellow	Gypsum	17044	
		12200-16685	No fluorescence	only Halite	14760	
WR-29-003-ST1	26.927	8580-17525	NA	only Halite	14760	14760
WR-30-001-ST2	26.934	16100-20040	No fluorescence	only Halite	14760	14483
		20040-21500	trace Yellow	Gypsum	17044	
KC-10-001	26.958	6825-7670	No mudlog data			14492
		7670-8000	NA	only Halite		sonic log
		8000-9200	tr dull pale Yellow	Gypsum		at bottom
		8300-8500	NA	trace Sylvite		1100 ft of
		9920	NA	trace Tar		salt where
		10180-10200	tr dull pale Yellow	Gypsum		there is~ 20%
		12700-12900	tr dull pale Yellow	Gypsum		Sylvite
		13290-13400	NA	trace Sylvite		
		13350-13650	NA	40% Claystone + 20%		Calculated
		13650-13940	NA	40% Marl + 20% Claystone		Vp for whole salt
		13940-14250	NA	40% Claystone		is 14579
		14250-14540	NA	30% Claystone + traces Sylvite		
		14920-15100	tr dull pale Yellow	Gypsum		
		15440-15750	NA	10% Claystone		
		16300-18200	NA	traces of Sylvite		
		18300-18400	NA	red Clay		
		18700-18800	NA	10% red Sylvite / Carnallite		
		19670-19720	NA	of Hematite		
		22140-22440	NA	20% Sylvite		
		23140-23300	NA	20% Sylvite		
		23640-23908	NA	20% Sylvite		
		23908-24000	NA	10% Sylvite		
		24000-25990	NA	5% Sylvite		
GC-821-001	27.156	6060-6900	No fluorescence	only Halite	14760	14669
		6900-8000	trace dull Yellow	Gypsum	17044	
		8950-9650	NA	clay intrusion with	9500	
		10000-10500	NA	Anydrite present	21023	
		10500-19050	No fluorescence	only Halite	14760	
		19050-24000	rare tr dull Yellow	Gypsum	17044	

Table 2.6b. Mudlog description of various components within salt in northerly Group 4. Sylvite is the primary secondary salt component for Group 4.

Well name	Dec Latitude	Depth interval of flourescence	Flourescence color exhibited	Mineral present	Mineral Vp in ft/s	Salt interval velocity ft/s
WR-544-001	26.421	No mudlog--salt Vint taken from checkshot survey				15026
KC-511-001	26.470	13204-14215	No flourescence	95% Anhydrite	21023	16348
		15600-15750	bright Yellow	Gypsum + 20%	17044	
				dk. brown Asphalt	4921	
		17760-17800	NA	tr. brown Asphalt	4921	
		18380-18420	NA	tr. reddish FeO_2		
		20400-20900	pale Yellow	Gypsum	17044	
KC-93-001	26.515	8190-9163	NA	Anhydrite inclusions	21023	15226
		9163-9200	NA	20% calcareous clay	9500	from VSP
		9200-9300	NA	12% calcareous clay	9500	
		15300-15900	NA	trace dead oil	------	
		18300-18360	NA	tr Sylvite + f-g sand	12880	
		18900-19450	NA	trace red clay	9500	
		20390-20850	NA	trace pink Sylvite	12880	
		23700-24120	NA	trace pink Sylvite	12880	
GC-825-001-ST1	27.094	Mudlog starts below the shallow salt, but there is a VSP				15000
GC-955-002	27.015	18270-19070	dull Yellow	Gypsum	17044	18535
		18350-19160	NA	Anydrite present	21023	
GB-959-001	27.053	10568-10933	NA	Visable calc marl		17544
			NA	traces of anhydrite	21023	
		10933-11069	NA	Visable pink Sylvite	12880	
		14734-15300	NA	Visable pink Sylvite	12880	
		15060-15280	NA	20% shale	8200-8500	
		16000-16200	NA	average 15% shale	8400-8600	
		18300-18500	NA	average 40% SLTST		
		20300-20400	NA	Visable pink Sylvite	12880	
		22500-22600	NA	average 15% SLTST		
		23200-23400	NA	85% Sylvite+15% shale	12373	
		23600-23800	NA	20% Shale		
		24800-25534	NA	15% SLTST		

Table 2.7. Mudlog description of components within salt Group 5 in the northern area. These wells have significant anhydrite as the secondary salt component with gypsum usually being the third component.

2.5.2 Well log interval velocity displays

Another way to visualize the velocity variability within the salt is illustrated in plots of interval velocity versus depth. This was done by arbitrary lines through the wells in more or less a depositional dip direction (NW to SE for the Wilcox Formation) from inside the 3D velocity model discussed in Chapter 3. These plots integrate observations that are presented in Tables

2.3 to 2.7 in another way. Keep in mind when observing these V_{int} versus depth displays that you are observing velocity layers, not lithological layers. As a visual delineation tool, orange in the colorbar indicates an interval velocity range usually representing halite (or a sediment section with partial limestone). The color magenta indicates the interval velocity range usually associated with the presence of gypsum, or limestone, or volume fractions of anhydrite in the 30-50% range if inside the salt-body. The lighter-pink color denotes large volume fractions of anhydrite (>50%).

Figure 2.13 is an arbitrary dip profile that ties eight wells on the western side of the study area from north to south demonstrating the variability of salt interval velocities latitudinally. The northernmost well in this figure is KC-102-001 in Tiber Field and its lower than average salt V_{int} of 14,475 ft/s (4412 m/s) places it in Group 4. This well happens to be the deepest well drilled to date in the study area with a total depth of 35,050 ft (10683 m), which encounters volcanic tuff at the K/T boundary with Cretaceous limestone below. This Cretaceous limestone is the cause of the V_{int} spike towards the bottom of the well; it is not another salt layer. In KC-681-001 (in Table 2.3), there is a velocity checkshot survey but no mudlog. It is hypothesized, due to the well's southerly location that the higher-velocity zones in the halite are caused by the presence of gypsum. The same explanation may apply to the next well, KC-596-001. Based on data from wireline logs, the increase in velocities at the bottom of this well may be due to the presence of Cenozoic limestone mixed in with shale and siltstone. In KC-774-001, there is no salt but there is a 70 foot interval of Cenozoic limestone present which causes the V_{int} spike in the sediments. This well also has a checkshot velocity survey. Salt V_{int} values are average for halite in KC-736-001, where no evaporitic mineral inclusions are evidenced in the mudlog, only a small amount of claystone. The mudlog for KC-872-001 begins below salt in Cenozoic limestone, so there is no way to ascertain that its high salt V_{int} is due to gypsum, but it is highly probable due to geographic location. However, the last two wells experience significant jumps in salt Vint confirmed by the presence of gypsum in their mudlogs.

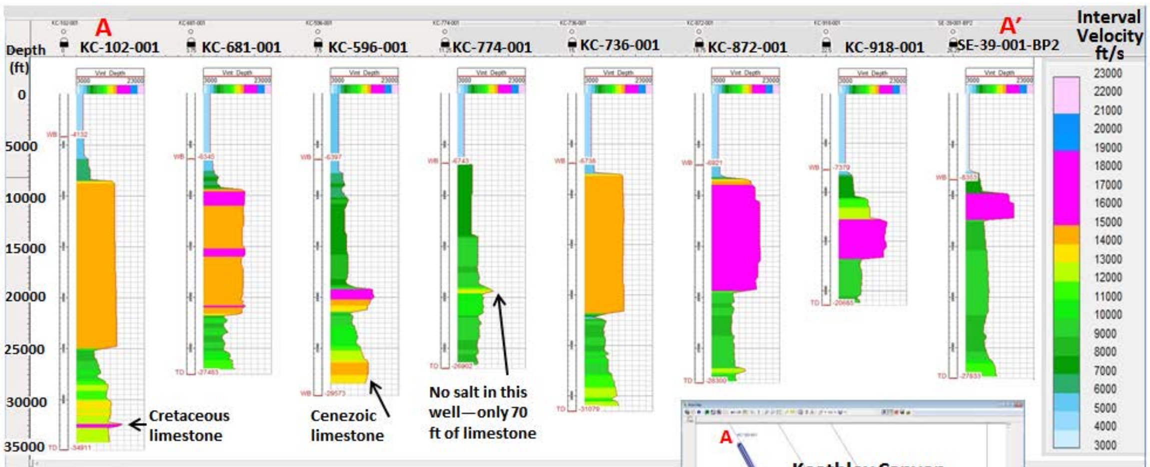

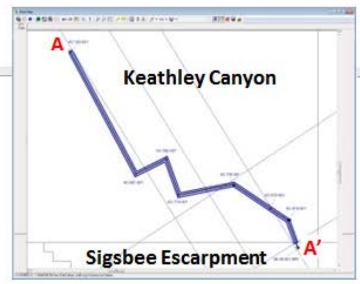

Figure 2.13. Interval velocity with a scale of 5,000 ft/sec (l1524 m/sec) in light blue to 23,000 ft/sec (7010 m/sec) in light pink vs. well depth in feet on vertical axis along dip arbitrary line A-A' in central Keathley Canyon. The color range for halite V_{int} is orange on this scale.

Figure 2.14 shows another well log cross section along the dip direction, in eastern Keathley Canyon, showing the lower salt $V_{\mathbf{int}}$ due to the presence of sylvite beginning with the Group 4 wells in the north (on the left) and then moving southeasterly down into the Group 1 wells which have higher salt velocities due to the noticeable presence of gypsum within the salt (on the right). Well KC-244-001-ST1 only has a trace of gypsum and the effect of the salt V_{int} increase caused by the gypsum is more than offset by the almost 10% volume fraction of sylvite (see Table 2.8), giving an overall interval velocity less than normal halite. Well KC-291-001 has several sediment inclusions of sand, shale and traces of limestone within its salt column and limestone occurring right below the salt. Limestone also occurs below salt in the KC-292-002 well. The odd well, KC-511-001 (fourth from the left) is a Group 5 well with ~ 1,000 ft (305 m) of anhydrite at the top of the salt column, and traces of anhydrite mixed in the halite matrix below. In KC-470-001 the salt column is pure halite until the lower half where traces of gypsum begin to appear. The KC-785-001 well evidences Cenozoic limestone above the salt with gypsum restricted to the base of salt. In KC-875-001-ST1, the mudlog does not mention any other salt components but does make the comment that the "halite" is unusually hard in places, indicating the possible presence of gypsum or calcite that the mudlogger didn't recognize. The salt V_{int} for this well is 14,892 ft/s (4539 m/s), suggesting there is some secondary inclusion present with a higher V_p than halite. There is limestone above the salt in KC-874-ss001 and minor amounts of

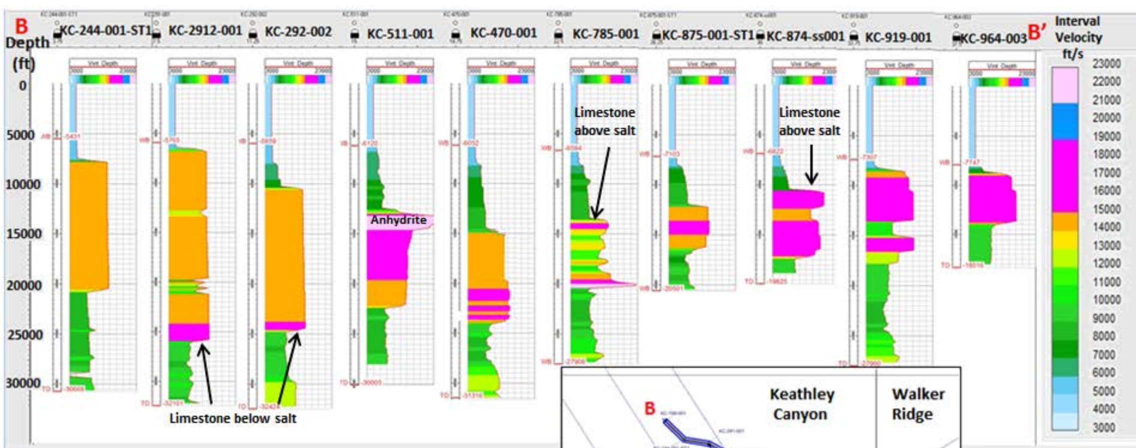

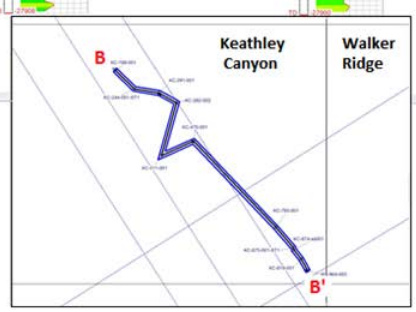

Figure 2.14. Interval velocity vs. well depth with same scales as in Figure 2.13 along arbitrary dip line B-B' located in eastern Keathley Canyon.

gypsum within the salt. The KC-919-001 and KC-964-003 wells exhibit salt with gypsum mixed into the halite matrix, thus raising the salt-body V_{int}. Figure 2.15 has shifted the dip line eastward into Walker Ridge. The north to south trend of lower salt V_{int} in the northern area of

Group 4, then slowly increasing V_{int} in the mid-latitudes with Groups 3 and 2, and increasing still more in the southernmost area of Group 1 wells, repeats itself. The WR-52-001-BP2 well in the Shenandoah sub-basin has inclusions of gypsum in its salt matrix. The same is true for nearby wells in WR-95-001 and WR-96-001-BP1. In the WR-316-001 well, the salt has gypsum inclusions in the upper part followed by shale inclusions, hence the changes in the salt V_{int} from higher than halite to lower than halite and then just average values halite for the remainder of the salt column. However, there is a 480 foot interval of ~60-65% limestone below the salt.

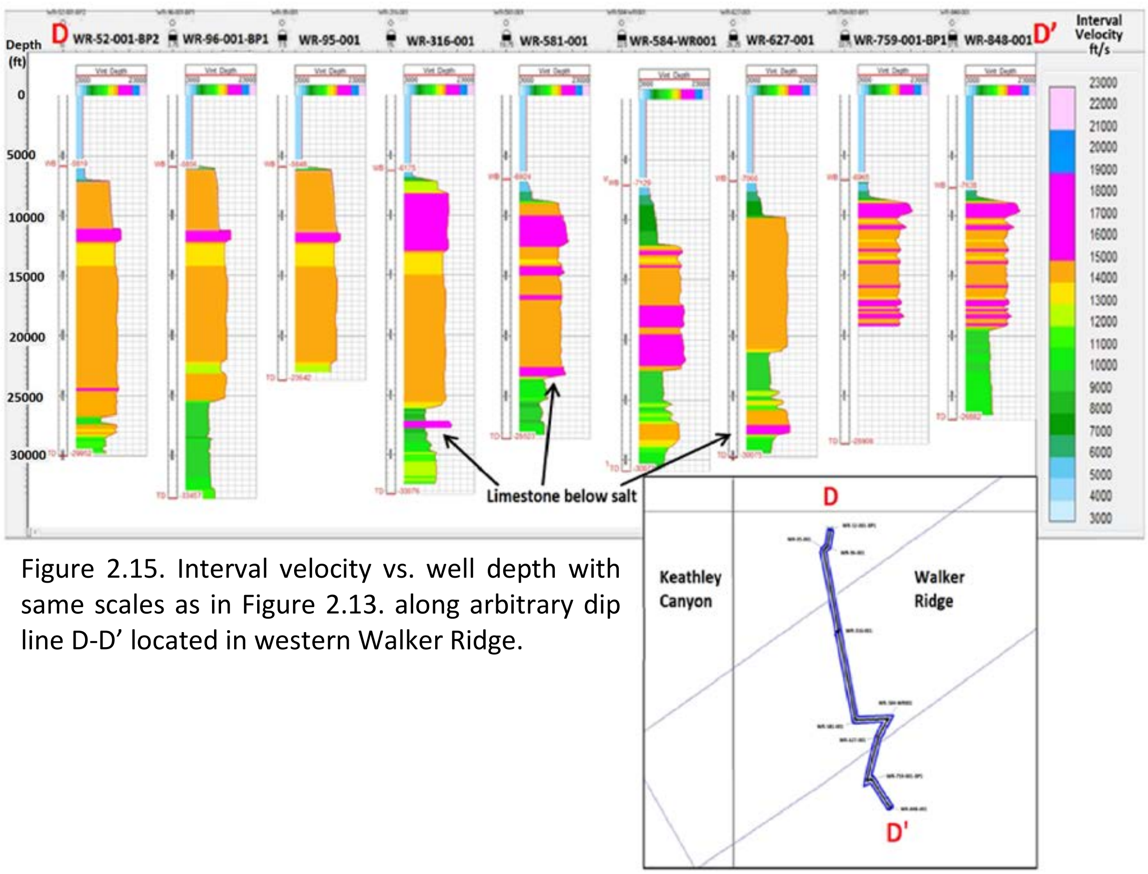

Figure 2.15. Interval velocity vs. well depth with same scales as in Figure 2.13. along arbitrary dip line D-D' located in western Walker Ridge.

There is no mudlog for WR-581-001; one can only hypothesize from its velocity profile that the salt-body contains gypsum, or else there might be a layer of Cenozoic limestone above the salt. The next well, WR-584-WR001, has gypsum with traces of shale and tar in the salt matrix, and an interval of limestone below salt, separated by a thick layer of shale. The WR-627-001 well is an odd well: it is the only well in the study area that shows 100% halite in its mudlog for the salt composition. The WR-759-001-BP1 well has no mudlog but there is a checkshot survey that generated the velocity profile vs. depth. However, in the WR-758-002 well, only 6780 ft (2067 m) away, there is a mudlog showing a strong presence of gypsum within the salt-body. The salt-body in WR-848-001 has gypsum, traces of tar and pyrite, as well as minor shale intrusions.

2.5.3 Calculated estimates of salt-body component volume fractions based on mudlogs

Unfortunately, the main compositional information for the salt-bodies is from commercial mudlogs. Mudlog descriptions are not accurate or precise. They are subjective and will depend upon the skill and experience of the mudlogger and the amount of detail requested by the drilling operator. In some wells, descriptions were made every 30 feet and in others, every 100 feet or more.

Converting the mudlog descriptions for the salt-body to percentage compositions over specific depth ranges, and then totaling the estimated percentages of a specific component over the entire salt body allows the compilation of compositional volume fractions. The calculated estimates of salt components based upon these mudlog descriptions for 44 wells in the study area are presented in Table 2.8. Though not to be interpreted as being correct in an absolute sense, this information is the best indication for mineralogical variation and can be used to study the direction (if not the absolute magnitude) of velocity changes due to varying composition. The standard deviation and mean value for each column are calculated without the one outlier well (GC-955-002) with the highest salt V_{int} due to its salt-body containing 57.49% anhydrite.

Well Name	salt group	salt V_{int} ft/s	salt V_{int} m/s	salt thickness in feet	salt thickness in meters	Halite %	Anhydrite %	Gypsum %	Sylvite %	Clastics or Other %
SE-39-001-BP2	1	15634	4765	2629	801	82.57		17.43		
WR-970-001	1	15422	4701	8893	2711	86.08		13.92		
WR-969-001	1	16289	4965	3622	1104	76.41	22.90	0.69		
KC-918-001	1	15815	4820	4003	1220	73.23		26.77		
KC-919-002	1	15416	4699	>3934	>1199	75.07		24.40		0.53
KC-919-003-BP1	1	15734	4796	3309	1009	66.11		33.89		
KC-875-002	2	14745*	4494	4016	1224	99.70				0.30
KC-875-001-ST1	2	14892	4539	4340	1323	96.65		3.35		
WR-848-001	2	14910*	4545	5312	1619	99.38		0.38		0.24
KC-872-001-BP1	2	14850	4526	11090	3380	97.57		2.43		
WR -758-PS005	2	14746	4495	9690	2954	99.47		0.15		0.38
WR-758-002	2	14815	4516	>10106	3080>	88.56		10.44		1.00
KC-736-001	2	14782	4506	13800	4206	99.92		0.00		0.08
KC-681-001	2	14740	4493	12302	3750	99.63		0.00		0.37
WR-674-001	2	14779	4505	7682	2342	95.88		4.12		
KC-698-001	2	14870*	4532	15080	4596	97.72	0.75	1.53		
WR-627-001	2	14731	4490	11523	3512	100.00				
WR-581-001	3	14706	4482	15316	4668	98.61				1.39
WR-584-WR001	3	14780*	4505	10399	3170	97.59		2.06	0.02	0.33
WR-543-001-BP1	3	14779	4505	15040	4584	99.01	0.33	0.66		
WR-460-001	3	14942*	4554	7454	2272	97.14	2.66	0.20		
KC-414-001	3	14880*	4535	11795	3595	96.63		3.12	0.25	
WR-372-001	3	14755*	4497	11690	3563	99.97		0.00		0.03
WR-316-001	3	14745	4494	19088	5818	95.17		4.71		0.12
WR-278-001	3	14836	4522	18083	5512	97.95		2.05		
KC-292-001-BP1	3	14925	4549	14314	4363	98.51		0.46		1.03
KC-292-002-BP1	3	14815	4516	14060	4286	98.19		1.28		0.53
WR-95-001	3	14965	4561	17320	5279	94.80		5.20		
KC-244-001-ST1	4	14549	4435	13080	3987	89.02		1.07	9.91	
WR-155-001-ST1	4	14388	4386	11110	3386	73.70		4.15	22.13	0.02
WR-143-003	4	14706	4482	13745	4190	95.67		0.71		3.62
WR-96-001-BP1	4	14762*	4500	22147	6750	98.70		0.01		1.29
KC 102-001	4	14475	4412	16495	5028	82.73		0.19	17.08	
WR-70-001	4	14595	4449	10608	3233	91.10		0.00	8.90	
KC-57-001	4	14751	4496	18330	5587	93.22		2.33	4.37	0.08
WR-52-001-BP2	4	14459	4407	21233	6472	82.30		0.14	17.56	
WR-30-001-ST2	4	14483	4414	>13188	>4020	80.41		0.44	19.15	
KC-10-001	4	14579	4444	19173	5844	95.54		0.19	1.11	3.16
GC-821-001	4	14669	4471	11028	3361	85.64	0.07	0.22	14.07	
KC-511-001	5	16348	4983	8950	2728	79.18	16.41	4.38		0.03
KC-93-001	5	15226	4641	16033	4887	92.26	7.33		0.29	0.12
GC-825-001-ST1	5	15000	4572	2670	814	96.34	3.66			
GC-955-002	5	18535	5650	2875	876	42.51	57.49			
GB-959-001	5	17544	5347	16950	5166	53.85	38.67		5.73	1.75
Standard deviations:		595	181	5425	1635	12.85	19.47	8.18	7.99	1.00
Mean values:		14996	4571	11443	3541	89.54	15.03	4.68	9.27	0.78

Table 2.8. Estimates of salt-body components for 44 wells based on mudlog descriptions. Salt-body V_{int} represent the whole salt column, except for wells marked with an asterisk. Those wells indicate that the velocity measurement did not penetrate the whole salt body and the stated velocity is representative only of the measured section. Column labeled "Clastics or other" includes pyrite, shale, siltstone, claystone, limestone, sand, marl, bitumen and tar. Note that the standard deviations and the mean values were calculated without the outlier well GC-955-002.

2.5.4 Mineralogical components within the salt-body by latitude

The study area has been divided into five different sections geographically based on composition and interval velocities (Figure 2.16). Essentially, the data presented in Table 2.8 has been converted to a map view that now clearly shows the latitudinal relationship of the five compositional groups.

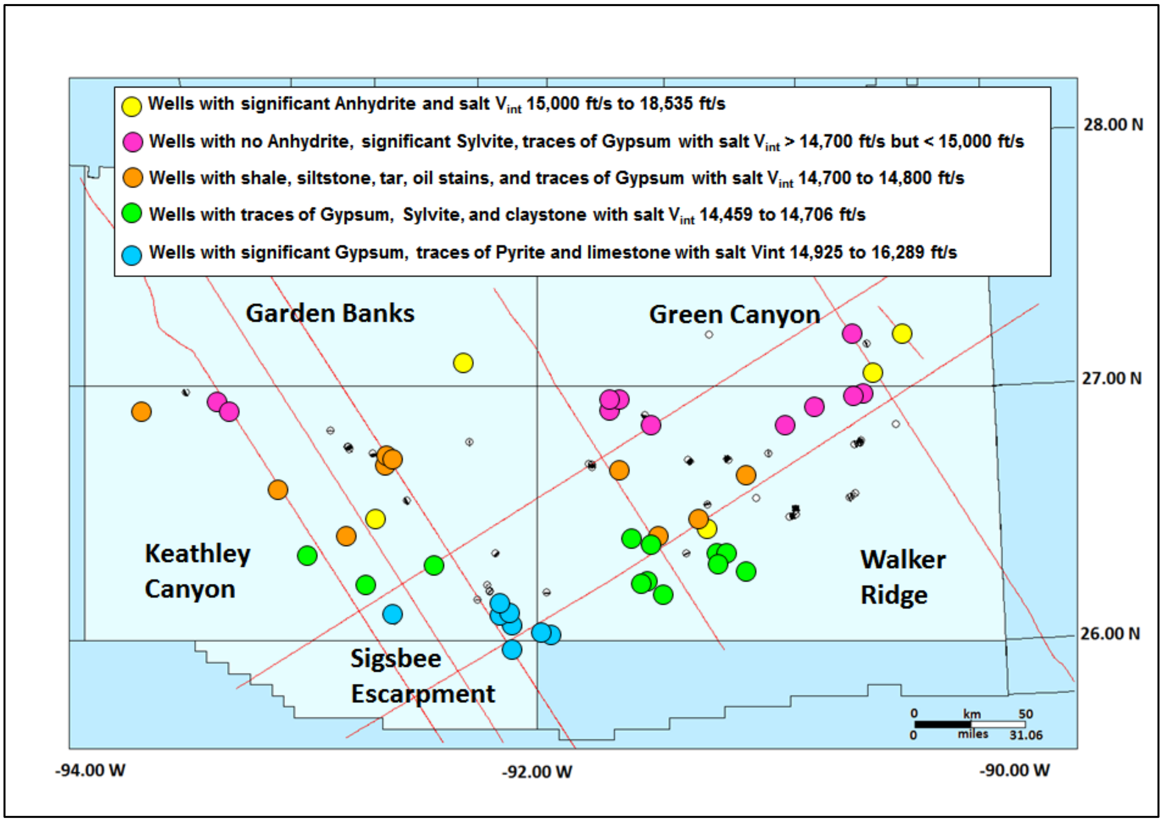

Figure 2.16. Data from Table 2.8 plotted onto the research study area basemap. The map clearly shows the latitudinal relationship suggested by the combined surface-seismic and borehole salt-body velocities plotted against decimal latitude in Figure 2.5b. Open black circles indicate straight vertical boreholes while other markings indicate the direction of deviated boreholes.

2.6 MINERALOGICAL MODELING OF VELOCITY

For these wells, halite is the primary component in all wells except one where anhydrite is more abundant. The secondary component can be gypsum, sylvite, anhydrite, or one of several sedimentary inclusions. The mineral elastic constants in Table 2.9 are laboratory measurements. At borehole depths >100 ft (30.48 m) the evaporites are assumed to have zero porosity (Alger and Crain, 1966). The clastic values are more or less averages from various borehole studies, but since clastic components are minor constituents in the salt-bodies, their overall effect is minimal.

2.6.1 Hashin-Shtrikman bounds

The Haskin-Shtrikman bounds are thought to be the tightest bounds possible for a homogeneous two-component material (Watt and O'Connell, 1980). However, in 1984, even tighter bounds on effective elastic constants were devised for cases in which the micro-geometry of each component is known and there is some similarity between the two (Kantor and Bergman, 1984). Meeting these requirements is not possible with borehole data evidencing variability not only in salt component mineralogy but also variability in the physical form of the individual components. Therefore, applying Hashin-Shtrikman bounds is a better choice for this large-scale dataset, even though these borehole salt-bodies are neither homogeneous nor isotropic; and possibly this will have some bearing on the results. The implicit long-wavelength assumption may preclude large cobbles/boulders and thicker layers, especially in the case of sonic logs. Nevertheless, it is instructive to calculate the magnitude of velocity variation that could result from compositional variation were the model valid. For a two-component material, the Hashin-Shtrikman bounds for the bulk modulus, K, and the shear modulus, μ are given by equation (1):

(1) $$K = K_2 + \frac{X_1}{(K_1 - K_2)^{-1} + (1-X_1)\,(K_2 + (4/3)\,\mu_2)^{-1}} \quad \text{and} \quad \mu = \mu_2 + \frac{X_1}{(\mu_1 - \mu_2)^{-1} + \dfrac{2(1-X_1)\,(K_2 + 2\mu_2)}{5\mu_2\,(K_2 + (4/3)\,\mu_2)}}$$

where, K_2 is the larger bulk modulus of the two components, K_1 is the smaller bulk modulus, X_1 is the volume fraction of the component with K_1, μ_2 is the shear modulus of the component having K_2 (not necessarily the larger μ), and μ_1 is the shear modulus for the component with K_1. The upper-bulk modulus bound is computed when $K_2 > K_1$ and the upper-shear modulus bound when μ_2 is the μ associated with K_2. The lower bounds are computed by interchanging the indices in the equations (Hashin, Z. and Shtrikman, S., 1963).

Anhydrite exhibits a large V_p in these wells and the in situ bulk and shear modulus had to be adjusted accordingly. Later regression analysis will suggest that perhaps the velocity used for gypsum was too low under deepwater borehole conditions. Since salt is almost never cored during deepwater drilling, no published borehole measurements for the elastic constants in evaporites could be located. The only known well in the study area that had sidewall cores taken in salt is in Mad Dog Field, Green Canyon block 825. These sidewall cores were analyzed for various salt constituents but not for any elastic constants (Fredrich, 2007). Fredrich found 4.03% anhydrite on average within the sidewall salt cores compared to the 3.66% calculated via mudlog for the whole salt column in the same well.

Mineral or sediment intrusion	ρ, density g /cm^3	K, bulk modulus in Gpa	μ, shear modulus in Gpa	V_p (ft/s)	V_p (m/s)	V_s (ft/s)	V_s (m/s)	Ref. no.
Halite	2.163	24.9	14.7	14763	4500	8553	2607	1,5,6
Anhydrite	2.963	^71.14	^37.99	21023	6408	11747	3581	3,6,7
Gypsum	2.317	42.0	15.4	17044	5195	8458	2578	4,5
Sylvite	1.987	18.1	9.4	12880	3926	7136	2175	2,5,6
Pyrite	5.016	142.7	125.7	26575	8100	16424	5006	2,9
Bitumen	1.346	5.0	2.0	8200	2499	3609	1100	11
Shale	2.46	25.0	13.8	9800	2987	5026	1532	6,8
Sandstone	2.33	^13.58	^7.69	10498	3200	5965	1818	7,9
Siltstone	2.76	16.95	5.03	9600	2926	4429	1350	9
Claystone	2.20	13.3	3.85	9500	2896	4341	1323	9
Limestone	2.71	65.0	24.0	19000	5791	10170	3100	9
^ calculated from V_p, V_s and ρ								

1 From Yan (2014)
2 From D. R. Schmitt (2014)
3 From www.appliedgeophysics.berkeley.edu/seismic/seismic_24
4 From Milsch and Priegnitz (2012)
5 From Alger and Crain at https://www.spec2000net/freepubs/Salt1966.pdf
6 From Jones and Davison (2014)
7 From Hunt (2006)
8 From Morcote, Mavko and Prasad (2010)
9 From Martinez (2014),Chang et al (2005) and www.jsg.utexas.edu/Hyzhu/files

Table 2.9. Mineral chart with elastic constants used in mineral modeling calculations. An additional source consulted was Robertson et al., 1958, but decision was made to use more recently calibrated values for halite, anhydrite and gypsum.

The upper and lower Hashin-Shtrikman (H-S) bounds for both K (bulk modulus) and μ (shear modulus) for the salt-body primary and secondary constituents in each well are shown in Table 2.10. Usually, the H-S bounds are then plotted against the porosity, but in this case the porosity is zero because the primary and secondary salt components are both evaporites in all wells except for six, where the secondary component is a clastic. Sometimes, the bounds are plotted against depth to show variability with depth but that is not possible with this dataset; the reason being that the percent of each component volume has been calculated for the whole salt-body and so the K and μ moduli represent the whole salt-body even though it is not homogeneous.

Using equation (2), we can calculate the compressional velocity (V_p) that such a specified salt-body should display and then compare it with the actual measured salt V_{int} values. Well data sonic measurements will be of much lower frequency content than those taken in a laboratory; and also there is the problem of attenuation in the real earth. Consequently, measured sonic velocities in the laboratory should be noticeably higher than those retrieved from well data.

(2) $V_{\mathbf{p}} = \sqrt{\dfrac{K+(4/3)\mu}{\rho}}$, where ρ is the volume fraction calculated density.

Well Name	salt group	salt V_{int} ft/s	Hashin-Shtrikman K_{HS} upper GPas	Hashin-Shtrikman μ_{HS} upper Gpas	volumetric density ρ	Vp upper H-S (ft/s)	% difference with well salt V_{int}	Hashin-Shtrikman K_{HS} lower GPas	Hashin-Shtrikman μ_{HS} lower GPas	Vp lower H-S (ft/s)	% difference with well salt V_{int}
SE-39-001-BP2	1	15634	27.32	14.90	2.190	15222	-2.64	27.16	14.80	15175	-2.94
WR-970-001	1	15422	26.81	14.88	2.184	15154	-1.74	26.69	14.78	15112	-2.01
WR-969-001	1	16289	30.14	17.49	2.331	15703	-3.60	29.44	17.14	15529	-4.67
KC-918-001	1	15815	28.71	14.96	2.204	15406	-2.59	28.48	14.86	15348	-2.95
KC-919-002	1	15416	28.45	14.95	2.189	15415	-0.01	28.14	14.84	15344	-0.47
KC-919-003-BP1	1	15734	29.81	15.00	2.215	15549	-1.18	29.53	14.90	15484	-0.47
KC-875-002	2	14745	25.00	13.79	2.168	14669	-0.52	24.99	13.80	14348	2.70
KC-875-001-ST1	2	14892	24.81	14.80	2.237	14634	-1.73	25.33	14.72	14702	-1.28
WR-848-001	2	14910	24.85	14.80	2.238	14636	-1.84	25.37	14.72	14705	-1.37
KC-872-001-BP1	2	14850	25.21	14.81	2.167	14936	0.58	25.30	14.71	14914	0.43
WR-758-002	2	14815	26.79	14.87	2.182	15156	2.30	25.08	14.71	14840	0.17
KC-736-001	2	14782	24.910	14.710	2.163	14877	0.64	24.910	14.70	14873	0.62
KC-681-001	2	14706	25.00	13.803	2.163	14689	-0.12	24.99	13.80	14365	-2.32
WR-674-001	2	14759	25.44	14.82	2.169	14968	1.42	25.42	14.72	14942	1.24
KC-698-001	2	14807	25.21	14.81	2.149	14998	1.29	25.09	14.71	14955	1.00
WR-627-001	2	14731	24.90	14.70	2.163	14873	0.96	24.90	14.70	14546	-1.25
WR-584-WR001	3	14780	25.22	14.81	2.159	14966	1.26	25.16	14.71	14933	1.04
WR-543-001-BP1	3	15152	25.03	14.81	2.151	14961	-1.26	24.95	14.7	14924	-1.50
WR-460-001	3	14935	25.48	15.03	2.180	14983	0.32	25.38	14.96	14953	0.12
KC-414-001	3	14880	25.34	14.82	2.162	14975	0.64	25.29	14.72	14944	0.43
WR-372-001	3	14755	24.99	13.81	2.163	14689	-0.45	24.88	13.20	14532	-1.51
WR-316-001	3	14745	25.54	14.83	2.168	14992	1.68	25.49	14.73	14961	1.46
WR-278-001	3	14836	25.15	14.81	2.166	14929	0.63	25.15	14.71	14907	0.48
KC-292-001-BP1	3	14925	24.79	14.68	2.166	14839	-0.58	24.70	14.60	14806	-0.80
WR-95-001	3	14965	25.59	14.83	2.171	14988	0.15	25.55	14.73	14961	-0.03
KC-244-001-ST1	4	14549	24.12	14.20	2.147	14691	0.98	24.03	14.12	14657	0.74
WR-155-001-ST1	4	14388	23.20	13.55	2.130	14771	2.66	22.88	13.32	14657	1.87
WR-143-003	4	14706	25.22	14.33	2.165	14893	1.27	25.18	14.25	14866	1.09
WR-96-001-BP1	4	14762	25.00	14.63	2.159	14909	1.38	24.96	14.57	14888	1.24
KC-102-001	4	14475	23.57	13.82	2.129	14564	0.61	23.52	13.79	14549	0.51
WR-70-001	4	14595	24.20	14.26	2.147	14709	0.78	24.18	14.23	14699	0.71
KC-57-001	4	14751	24.55	14.5	2.157	14978	1.54	24.38	14.34	14913	1.10
WR-52-001-BP2	4	14459	23.53	13.80	2.129	14551	0.64	23.49	13.77	14537	0.54
WR-30-001-ST2	4	14483	23.41	13.71	2.120	14543	0.41	23.35	13.67	14522	0.27
GC-821-001	4	14669	23.80	13.98	2.139	14606	-0.43	23.75	13.95	14589	-0.55
KC-511-001	5	16348	32.04	18.59	2.199	16669	1.96	29.07	17.07	15919	-2.62
KC-93-001	5	15223	27.20	16.01	2.222	15326	0.68	26.63	15.7	15170	-0.35
GC-825-001-ST1	5	15000	25.63	15.11	2.192	14983	-0.11	25.57	15.06	14963	-0.25
GC-955-002	5	18535	45.95	26.04	2.623	18185	-1.89	43.35	21.66	17696	-4.53
GB-959-001	5	17544	36.45	20.63	2.472	17899	1.97	33.41	19.18	16743	-4.57

Table 2.10. Calculated Hashin-Shtrikman bounds values and derived V_p for all study wells.

Comparison between the predicted salt velocities generated by the upper and lower H-S bounds with the measured salt-body interval velocities is shown in Figure 2.17.

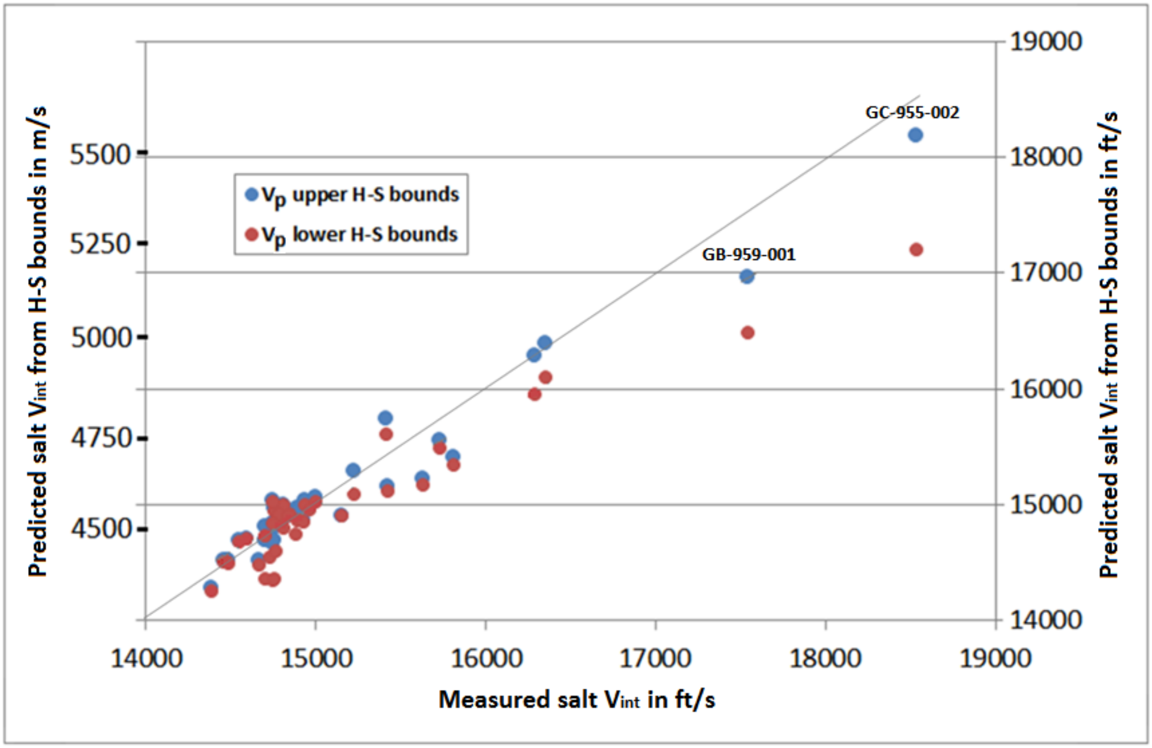

Figure 2.17 Comparison of upper and lower H-S bounds derived velocities with measured salt Vint velocities. The two extreme outlier wells with significant anhydrite are labelled.

Since the upper and lower bounds are very close numerically, the upper and lower bounds values were averaged and then used in calculating the H-S velocities plotted in Figure 2.17. The density used in these calculations was a volumetrically proportioned density. The velocities derived from the upper Hashin-Shtrikman bounds and the lower Hashin-Shtrikman bounds are found in Table 2.10. In general, the bounds' derived velocities are within 2% agreement for 35 of the wells, agree between 2% and 5% for another four wells and then the last well has Hashin-Shtrikman derived velocities differing between -9.45% and -10.46%. This "outlier" has >57% anhydrite present with the secondary component as halite. Anhydrite has very large moduli values compared to those of halite, but even so, the derived H-S velocities do not measure up to the VSP measured value of 18,535 ft/s (5650 m/s) for the salt-body interval velocity in this well.

2.6.2 Calculation of proportional (or volume fraction) bounds

Desiring to add to the results from the Hashin-Shtrikman bounds, I sought to find bounds more representative of the salt-body that did not require the salt mixture to be either homogeneous or isotropic. If we look at the whole salt-body with its components calculated as volume fractions, and that Hashin-Shtrikman bounds are based on volume fractions, it makes sense to try a volumetrically proportioned set of moduli based on a volume fraction (%) contribution. The other advantage to this simplistic idea is it allows all components of the salt matrix, whether it is just two components or 10, to be included in the representative volume fraction contribution to the overall bulk and shear modulus of the salt. For example: If the salt contains 95% halite, 4% gypsum, and 1% anhydrite, then the proportional bulk modulus is given by equation (3) and likewise, the proportional shear modulus is given by equation (4):

(3) $K = 0.95(K \text{ for halite}) + 0.04(K \text{ for gypsum}) + 0.01(K \text{ for anhydrite}) = 26.05$ GPas

(4) $\mu = 0.95(\mu \text{ for halite}) + 0.04(\mu \text{ for gypsum}) +0.01(\mu \text{ for anhydrite}) = 14.96$ GPas

These calculations were done for the wells having measured salt Vint and then derivative compressional velocities from equation (2) were calculated. The V_p from both the proportional bounds and the averaged H-S bounds are plotted in Figure 2.18. The velocities from the proportional bounds match very well to the measured salt V_{int} with 35 out of 40 well salt-bodies matching with less than 2% difference. The other five salt V_{int} match between 2.08% and 3.59% difference, which is a slightly closer match than the H-S bounds; and with this calculation, there is no outlier (see Table 2.10). In these five instances, there is either a large component of gypsum or anhydrite in the salt composition. This is due to the high values of the moduli for gypsum and anhydrite relative to halite. Considering the volume fractions were estimated from mudlogs, this is fairly good agreement. Note that if the salt V_{int} is >15,800 ft/s (4816 m/s), the averaged H-S bound velocity will be lower than the measured salt-body V_{int} while the proportional-bound velocity will be higher; and that below a measured salt-body V_{int} of 15,000 ft/s (4572 m/s), the predicted velocity from both bounds is fairly close to the measured velocity.

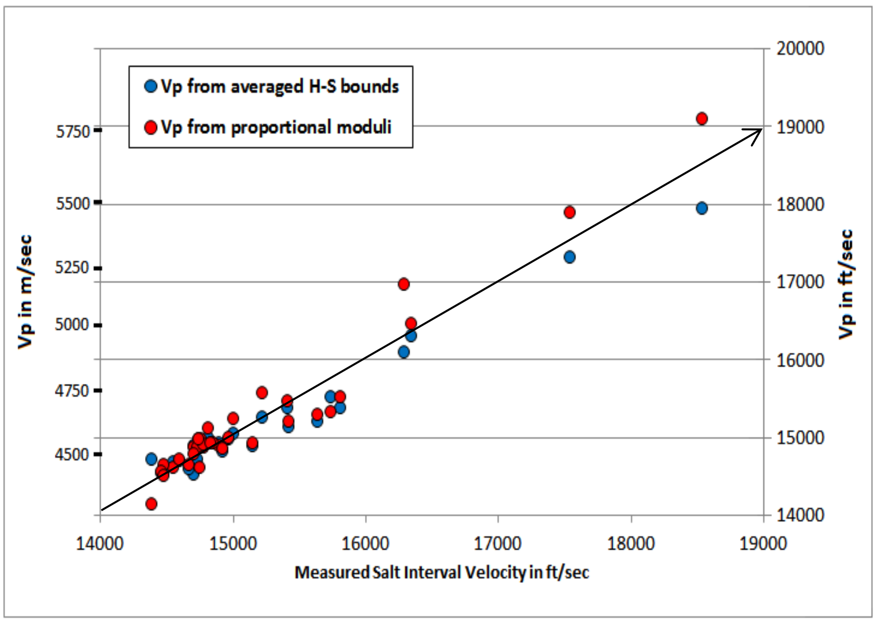

Figure 2.18. Salt V_{int} from well data plotted against the V_p calculated from the average of Hashin-Shtrikman bounds and V_p from the proportional bounds. The black diagonal line is for the calculated velocities equaling the measured velocities.

Well Name	salt Vint ft/s	Proportional K in GPas	Proportional μ in GPas	Proportional derived V_p in ft/s	volumetric density ρ	% difference with well salt V_{int}
SE-39-001-BP2	15634	27.88	14.82	15294	2.190	2.19
WR-970-001	15422	27.28	14.80	15210	2.184	1.37
WR-969-001	16289	35.607	20.04	16963	2.331	3.59
KC-918-001	15815	29.48	14.96	15513	2.204	1.91
KC-919-002	15416	29.13	14.96	15458	2.189	0.27
KC-919-003-BP1	15734	30.69	14.94	15323	2.215	2.61
KC-875-002	14745	24.90	14.70	14887	2.168	-0.03
KC-875-001-ST1	14892	24.96	14.70	14856	2.1635	0.17
WR-848-001	14910	24.91	14.67	14856	2.168	0.17
KC-872-001-BP1	14850	25.31	14.72	14928	2.167	0.53
WR-758-002	14815	26.69	14.76	15123	2.182	2.08
KC-736-001	14782	24.91	14.69	14872	2.163	0.61
KC-681-001	14706	24.89	14.69	14869	2.163	1.11
WR-674-001	14759	25.60	14.73	14975	2.169	1.46
KC-698-001	14807	25.51	14.88	14916	2.194	0.73
WR-627-001	14731	24.90	14.70	14873	2.163	0.96
WR-584-WR001	14780	25.17	14.66	14906	2.166	0.85
WR-543-001-BP1	15152	25.165	14.78	14929	2.167	1.47
WR-460-001	14935	26.16	15.32	15152	2.184	1.45
KC-414-001	14880	25.416	14.71	14947	2.167	0.45
WR-372-001	14755	24.897	14.698	14872	2.163	0.79
WR-316-001	14745	25.67	14.72	14976	2.168	1.54
WR-278-001	14836	25.25	14.71	14924	2.166	0.59
KC-292-001-BP1	14925	24.90	14.65	14859	2.166	0.44
WR-95-001	14965	25.79	14.74	15001	2.171	0.24
KC-244-001-ST1	14549	23.96	14.02	14614	2.147	0.44
WR-155-001-ST1	14388	22.36	12.91	14134	2.130	1.76
WR-143-003	14706	25.05	14.21	14782	2.165	0.51
WR-96-001-BP1	14762	24.87	14.54	14850	2.159	0.98
KC-102-001	14475	23.69	13.77	14637	2.129	1.10
WR-70-001	14595	24.30	14.23	14720	2.147	0.85
KC-57-001	14751	24.00	14.11	14610	2.157	0.96
WR-52-001-BP2	14459	23.67	13.75	14554	2.129	0.65
WR-30-001-ST2	14483	23.49	13.62	14499	2.120	0.11
GC-821-001	14669	24.01	13.97	14648	2.123	-0.14
KC-511-001	16348	33.23	18.55	16465	2.215	0.71
KC-93-001	15223	28.28	16.38	15577	2.221	2.32
GC-825-001-ST1	15000	26.59	15.55	15236	2.192	1.57
GC-955-002	18535	51.48	28.09	19093	2.623	3.01
GB-959-001	17544	42.39	23.41	17892	2.472	1.98

Table 2.11. Calculated proportional bounds based on volume fraction and derived V_p for all study wells.

2.6.3 Plot of Hashin-Shtrikman bounds values versus volumetric percentage of halite

Since the H-S upper and lower bounds from this dataset are so close together, any plot of the lower bounds would be virtually identical to one of the upper bounds. For accuracy's sake, the two were averaged together for computing the derived V_p in Figure 2.18, but here that is not necessary. The idea is to see if the mineralogical contents are distinct, and they are. In Figure 2.19, the bulk and shear moduli computed from the upper H-S bounds are plotted vs. the volume fraction of halite. The upper plot line for both the bulk and the shear modulus contains wells with salt having varying percentages of anhydrite present as its secondary component. The next plot line down shows all the wells having gypsum as the secondary component. The next group of wells lower and to the right is the "sediment" well group where the secondary component is siltstone, sandstone, claystone, or shale. The lowest line is for the wells having sylvite as the secondary component.

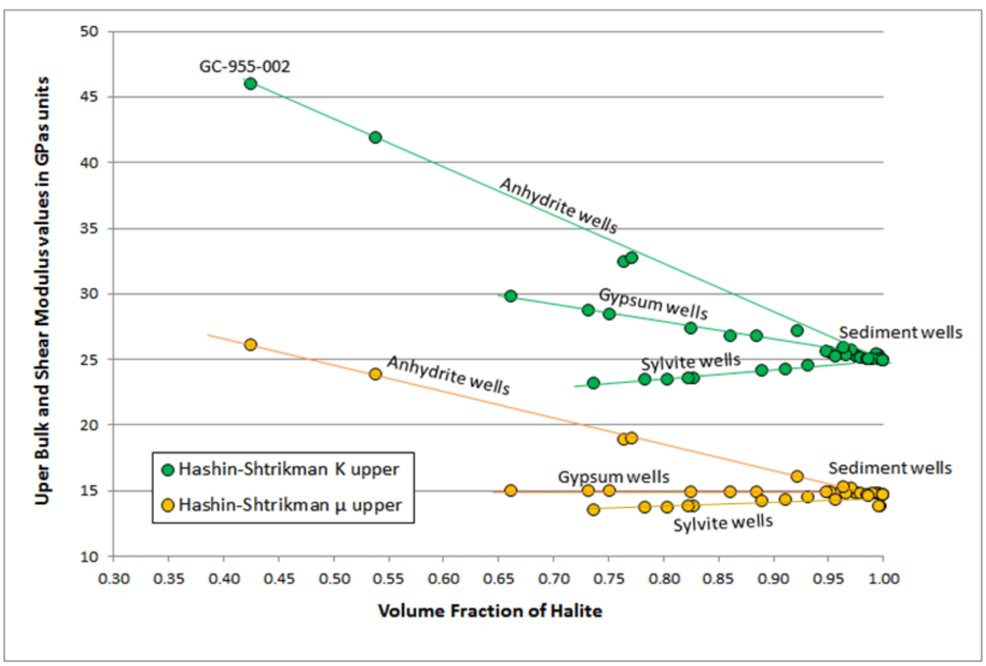

Figure 2.19. Plot of Hashin-Shtrikman upper bounds values vs. volumetric percentage of halite in salt. The bounds plot according to the secondary component in the salt composition.

2.6.4 Multicomponent Hashin-Shtrikman bounds

There was concern, since the salt-bodies in 23 out of the 40 wells in this mineralogical study had more than two components, that perhaps standard Hashin-Shtrikman bounds were not entirely appropriate, in spite of the excellent results. Consequently, the Hashin-Shtrikman bounds for multicomponents in a given material were applied to these 23 wells and the results then compared with both the regular Hashin-Shtrikman bounds and the proportional bounds. A search for an appropriate version of multicomponent equations allowing for zero porosity (Bőhkle and Lobos, 2013 and Brown, 2013) in the components led to the following version (Walpole, 1966) in equations (5) and (6):

$$(5)\qquad K_{HS-} = \left[\sum_{i=1}^{n} \frac{x_i}{K_i + \frac{4}{3}\mu_{min}}\right]^{-1} - \frac{4}{3}\mu_{min}\,, \qquad K_{HS+} = \left[\sum_{i=1}^{n} \frac{x_i}{K_i + \frac{4}{3}\mu_{max}}\right]^{-1} - \frac{4}{3}\mu_{max} \quad \text{and}$$

$$(6)\qquad \mu_{HS-} = \left[\sum_{i=1}^{n} \frac{x_i}{\mu_i + \frac{\mu_{min}}{6}\left(\frac{9K_{min} + 8\mu_{min}}{K_{min} + 2\mu_{min}}\right)}\right]^{-1} - \frac{\mu_{min}}{6}\left(\frac{9K_{min} + 8\mu_{min}}{K_{min} + 2\mu_{min}}\right)$$

$$\mu_{HS+} = \left[\sum_{i=1}^{n} \frac{x_i}{\mu_i + \frac{\mu_{max}}{6}\left(\frac{9K_{max} + 8\mu_{max}}{K_{max} + 2\mu_{max}}\right)}\right]^{-1} - \frac{\mu_{max}}{6}\left(\frac{9K_{max} + 8\mu_{max}}{K_{max} + 2\mu_{max}}\right), \text{ where}$$

K_{min} and K_{max} are the minimum and maximum bulk moduli of the components; K_{HS-} and K_{HS+} are the Hashin-Shtrikman lower and upper bounds for bulk modulus of the composite; $\mu_{\mathbf{min}}$ and $\mu_{\mathbf{max}}$ are the minimum and maximum shear moduli of the components; $\mu_{\mathbf{HS-}}$ and $\mu_{\mathbf{HS+}}$ are the minimum and maximum lower and upper bounds for the shear modulus of the component. The results of multicomponent Hashin-Shtrikman bounds' derived K, μ and $V_{\mathbf{p}}$ are displayed in Table 2.12.

Well Name	Salt Vint in ft/s	Multicomponent H-S K_{HS} upper in GPas	Multicomponent H-S μ_{HS} upper in Gpas	Vp from upper H-S multi-component bounds	% difference with well salt V_{int}	Multicomponent H-S K_{HS} lower in GPas	Multicomponent H-S μ_{HS} lower in Gpas	Vp from lower H-S multi-component bounds	% difference with well salt V_{int}
WR-969-001	16289	32.317	18.873	16291	0.01	30.905	18.139	15948	-2.09
KC-919-002	15416	28.988	17.763	15739	2.09	28.894	15.520	15614	1.28
WR-848-001	14910	24.970	14.669	14868	-0.28	24.961	14.656	14863	-0.32
WR-758-002	14815	26.236	14.762	14998	1.24	26.220	14.741	14991	1.19
KC-698-001	14807	25.262	14.834	14864	0.38	24.889	14.802	14795	0.08
WR-584-WR001	14780	25.176	14.722	14921	0.95	25.155	14.720	14917	0.93
WR-543-001-BP1	15152	25.087	14.759	14911	-1.59	25.057	14.748	14903	-1.64
WR-460-001	14935	25.699	15.141	15037	0.67	25.532	15.055	14991	0.37
KC-414-001	14880	25.270	14.706	14929	0.33	24.138	14.704	14740	0.94
WR-316-001	14745	25.672	14.903	15036	1.97	25.658	14.887	15030	1.93
KC-292-001-BP1	14925	25.042	14.591	14862	0.42	25.024	14.559	14852	0.49
KC-244-001-ST1	14549	24.250	14.104	14691	0.98	24.208	14.062	14674	0.86
WR-155-001-ST1	14388	22.535	13.381	14283	-0.73	22.477	13.318	14258	-0.90
WR-143-003	14706	25.265	14.136	14808	0.69	25.234	13.838	14737	0.21
WR-96-001-BP1	14762	24.742	14.447	14810	0.33	23.507	14.435	14602	1.08
KC-102-001	14475	23.596	13.653	14523	0.33	23.577	13.601	14507	0.22
KC-57-001	14751	24.876	14.466	14844	0.63	24.840	14.444	14833	0.55
WR-52-001-BP2	14459	23.554	13.624	14522	0.43	23.515	13.571	14503	0.30
WR-30-001-ST2	14483	23.470	13.532	14517	0.23	23.421	13.473	14495	0.04
GC-821-001	14669	23.549	13.606	14513	-1.06	23.417	13.545	14477	-1.31
KC-511-001	16348	31.316	17.975	16389	0.25	30.191	17.375	16102	-1.50
KC-93-001	15223	27.049	15.894	15289	0.43	26.283	15.560	15096	-0.83
GB-959-001	17544	37.457	21.446	16958	-3.34	35.177	20.452	16489	-6.01

Table 2.12. Bulk and shear moduli calculated using multicomponent Hashin-Shtrikman bounds and the velocities derived from them for the 23 wells having more than 2 components within salt.

Comparison of the velocity values derived from the three bounds with the measured salt V_{int} is made in Figure 2.20. The diagonal line is for $V_{\mathbf{p}}$ bound value equal to salt-body $V_{\mathbf{int}}$ value. Interestingly, the proportional bound values are higher at the higher velocity ranges, where the salt-body contains either anhydrite or gypsum; but fall to either side of the line at $V_p < 16{,}000$ ft/s (4877 m/s), similar to Figure 2.18. An enlarged version of Figure 2.20 for the lower velocities is shown in Figure 2.21. The averaged multicomponent derived velocities tend to be lower when V_p > 16,000 ft/s (4877 m/s). It is difficult to discern which bound values are the closest to the measured values by visual inspection, so mean absolute deviations (MAD) and mean-squared error (MSE) calculations were done for all three bounds and displayed in Table 2.13. It is the relative comparison among them that is important.

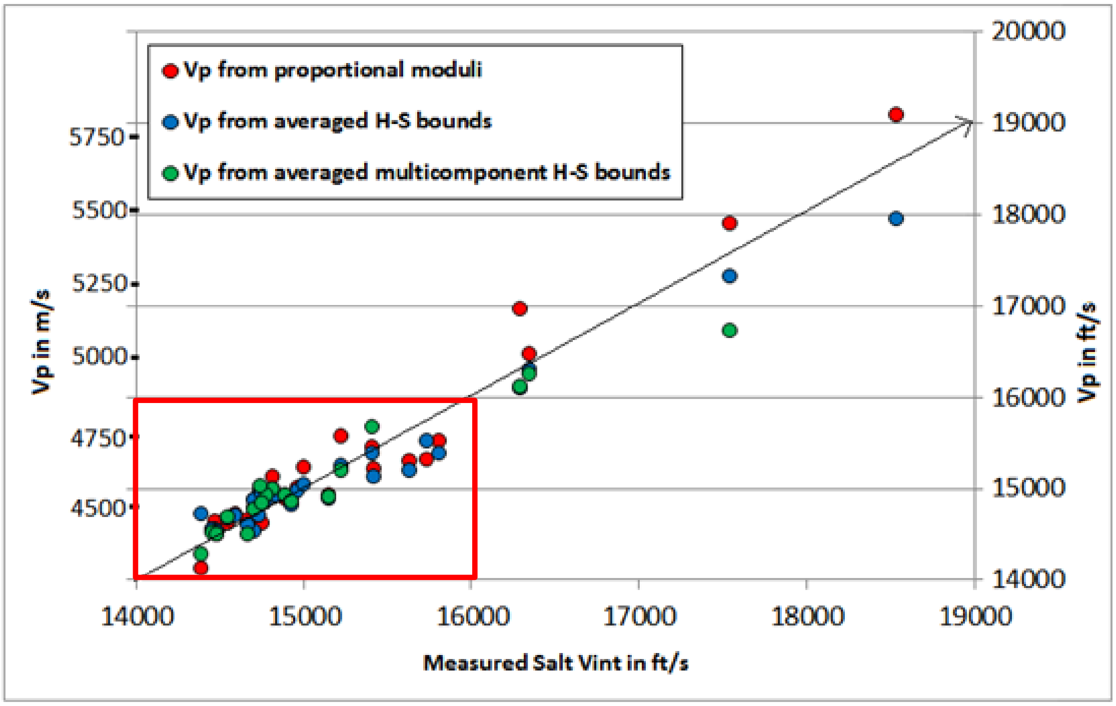

Figure 2.20. Velocities computed from various bounds plotted against the measured salt V_{int}. The enlargement of the left corner is plotted in Figure 2.21.

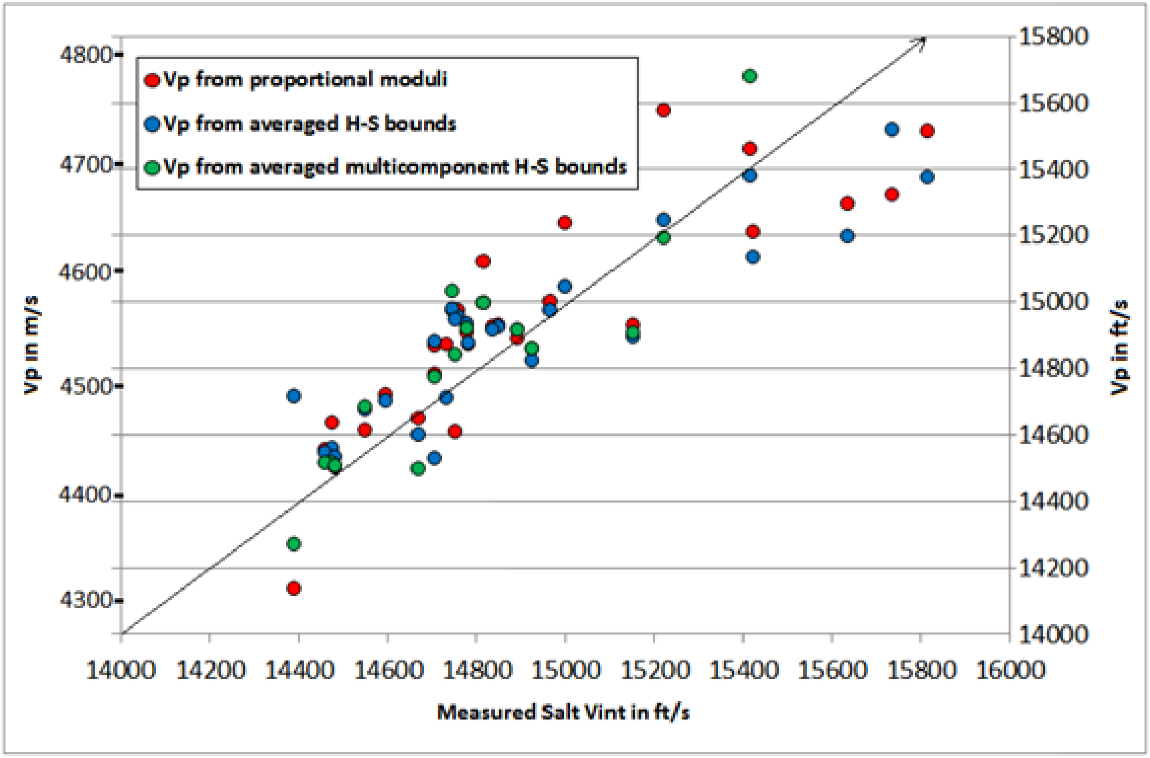

Figure 2.21. Enlargement of left corner inside the red box in Figure 2.20 showing the details of the velocity distribution.

The velocities from the proportional bounds are greater than those derived from the multicomponent H-S bounds, but in between the upper and lower standard H-S bounds. So, if one is looking for a rule of thumb, the proportional bounds are a quick approximation to the more accurate versions of the H-S bounds.

	V_p upper H-S bounds	V_p lower H-S bounds	Proportional derived V_p	Multicomponent V_p upper H-S	Multicomponent V_p lower H-S	
English units	162	206	178	130	173	MAD
English units	40864	100762	52222	32929	72904	MSE
Metric units	49.4	62.8	54.3	39.6	52.7	MAD
Metric units	12455	30713	15917	10037	22221	MSE

Table 2.13. Mean absolute deviation (MAD) and mean-squared error (MSE) for the velocities from standard Hashin-Shtrikman bounds, proportional bounds and multicomponent Hashin-Shtrikman bounds compared to the measured salt V_{int}. The English velocity units are in ft/s (so the numbers are relatively large) and the metric velocity units are in m/s.

2.6.5 Wyllie Time-Averaging

The Wyllie time-average equation relates sonic velocities with the porosity of a rock, basically stating that the total travel-time recorded on a sonic log is the sum of the time the sonic wave spends traveling through the rock matrix and through the fluids in the pores (Wyllie, et al., 1956). In this study, the evaporites have zero porosity and the small volume fractions of sediments found in the salt from 18 out of our 40 wells are relatively insignificant. Wyllie time-average velocities were calculated using equation (7) and the results are found in Table 2.14.

(7) $\frac{1}{V_p} = \frac{X_1}{V_{p1}} + \frac{X_2}{V_{p2}} + \frac{X_3}{V_{p3}} + \ldots\ldots,$ where V_{pi} is the respective compressional velocity of the volume fraction for each component, represented by X_i, and V_p is the representative compressional velocity for the whole salt body. The Wyllie time-average velocities and the salt V_{int} were plotted against the volume fraction of halite in Figure 2.22. In most instances, the Wyllie V_p is lower than the borehole salt V_{int}, but agreeing with a less than 2% difference in 33 out of 40 wells. The other seven wells range from 2.47% to 6.70% difference and again these wells are the ones with noticeable anhydrite and/or gypsum present in the salt-body.

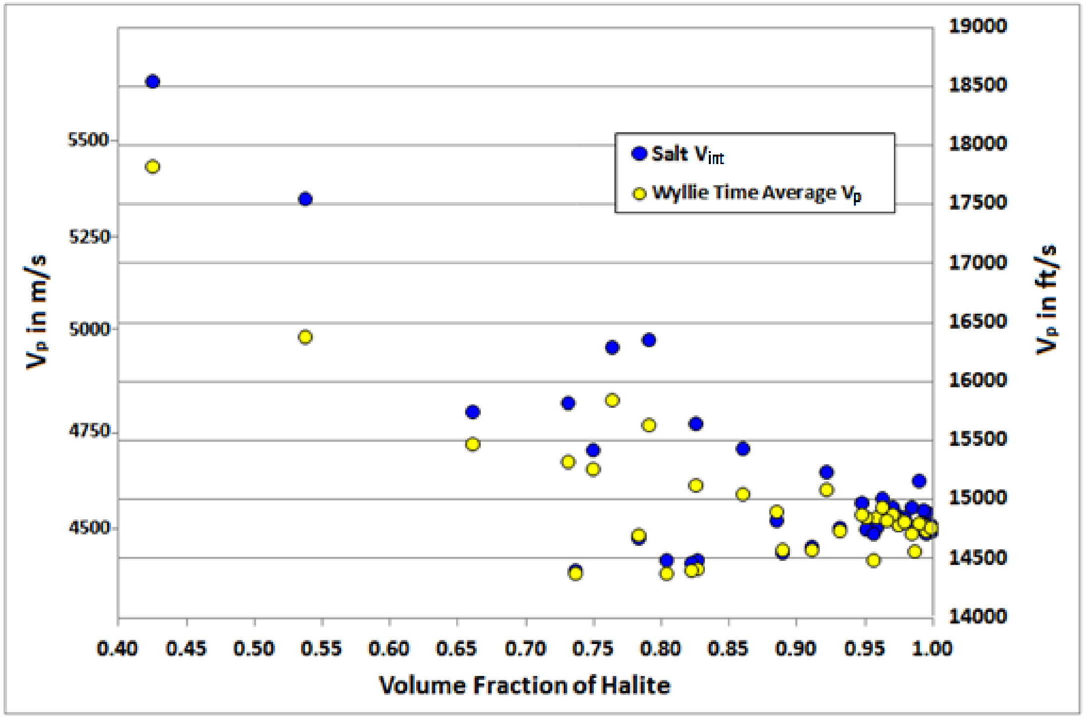

Figure 2.22. Salt V_{int} and Wyllie time-average velocities plotted against the volume fraction of halite in the salt matrix.

2.6.6. Backus averaging

Backus averaging requires thin layers of inclusions within the primary component (Sams and Williamson, 1994) and (Bos et al., 2016). In this specific data set, all mineralogical inclusions appear random and do not uniformly occur across 100% of total salt-body volume, not even within the zone of occurrence across the diameter of a borehole. In general, the same is true for the sediment inclusions that generally occur as a volume fraction over a short depth span relative to the whole salt column, and there is no evidence of layering. Nonetheless, it is useful to apply Backus averaging and look at the results. The equations for Backus averaging are given in the equations (8), (9) and (10):

(8) using the plane wave modulus $M = K + (4/3)\,\mu$, where K is the bulk modulus and μ is the shear modulus,

(9) $\frac{1}{M} = \frac{X_1}{M_1} + \frac{X_2}{M_2} + \frac{X_3}{M_3} + \ldots\ldots$, where X_i is the volume fraction of the component.

(10) V_p = SQRT (M/ρ), with ρ being the density, so (10) becomes an analog to equation (2).

A plot of the salt V_{int} and the V_p from Backus Averages are plotted against the volume fraction of halite in the salt-bodies in Figure 2.23. There is a noticeable difference between this plot and the one in Figure 2.22 because the Backus Average velocities are higher than the salt V_{int} in ~ 50% of the wells, especially in wells where the halite volume fraction is >95%. The details are displayed in Table 2.15 next to the Wyllie Time-Average results. The MAD and MSE were also calculated for these two averages and were added to Table 2.13 and displayed in Table 2.14.

	V_p upper H-S bounds	V_p lower H-S bounds	Proportional derived V_p	Multicomponent V_p upper H-S bounds	Multicomponent V_p lower H-S bounds	V_p from Wyllie time-Average	V_p from Backus averages	
English units	162	206	178	130	173	185	249	MAD
English units	40864	100762	52222	32929	72904	34345	155089	MSE
Metric units	49.4	62.8	54.3	39.6	52.7	56.4	75.9	MAD
Metric units	12455	30713	15917	10037	22221	10468	42272	MSE

Table 2.14. Mean absolute deviations (MAD) and mean-squared errors (MSE) for the velocities from standard H-S bounds, proportional bounds, multicomponent H-S bounds, Wyllie Time-Averages, and Backus Averages compared to the measured salt V_{int}.

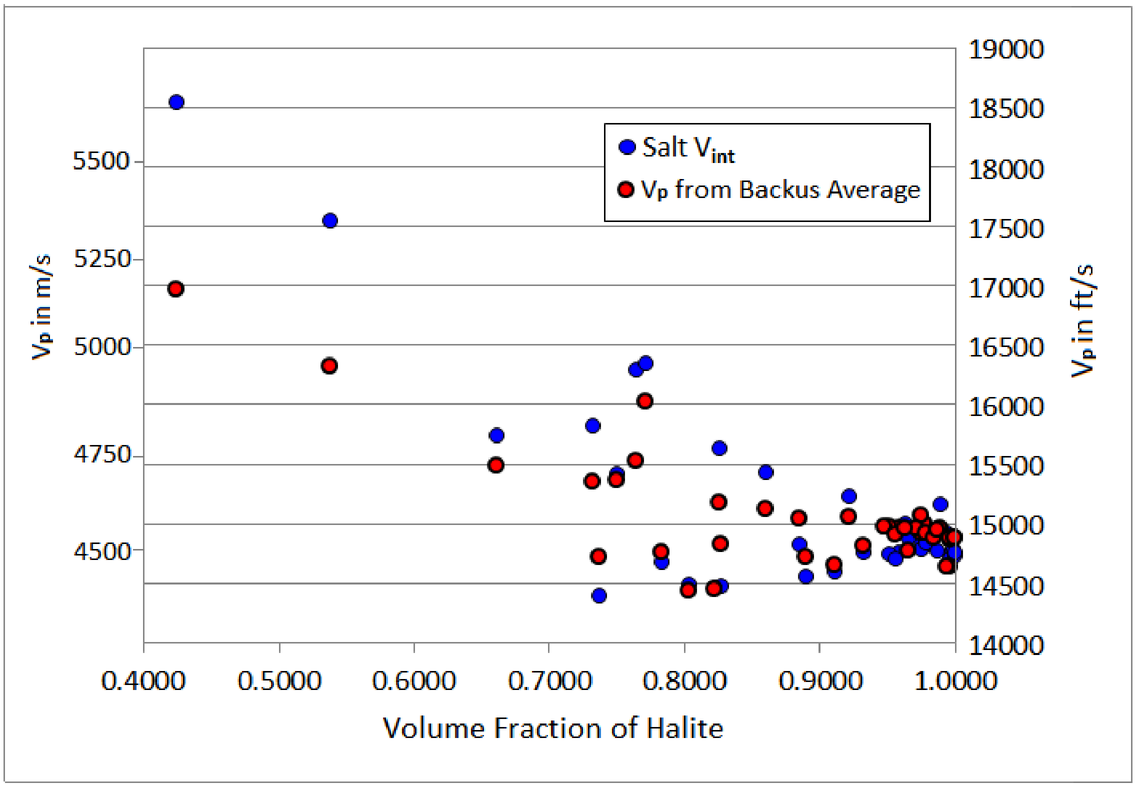

Figure 2.23. Salt V_{int} and V_p from Backus Averages plotted against the volume fraction of halite in the salt matrix.

Well Name	Salt Vint in ft/sec	Wyllie Time Average Vp in ft/s	% difference Wyllie vs salt V_{int}	Backus Average M	Volume Fraction density	Vp from M in km/s	Vp from Backus Average in ft/s	% difference Backus vs salt V_{int}
SE-39-001-BP2	15634	15114	-3.36	46.85157	2.190	4.625	15175	-2.93
WR-970-001	15422	15040	-2.40	46.35617	2.184	4.607	15115	-1.99
WR-969-001	16289	15837	-2.77	52.20378	2.331	4.732	15526	-4.68
KC-918-001	15815	15309	-3.20	48.21833	2.204	4.677	15345	-2.97
KC-919-002	15416	15253	-1.06	47.98741	2.189	4.682	15361	-0.36
KC-919-003-BP1	15734	15462	-1.73	49.31526	2.215	4.718	15480	-1.68
KC-875-002	14745	14738	-0.05	44.49190	2.168	4.530	14862	0.79
KC-875-001-ST1	14892	14767	-0.84	44.54006	2.164	4.462	14639	-1.70
WR-848-001	14910	14748	-1.09	44.52954	2.168	4.461	14634	-1.85
KC-872-001-BP1	14850	14808	-0.28	44.80889	2.167	4.547	14919	0.46
WR-758-002	14815	14896	0.55	45.86546	2.182	4.585	15042	1.53
KC-736-001	14782	14743	-0.26	44.49190	2.163	4.535	14880	0.73
KC-681-001	14706	14732	0.18	44.49190	2.163	4.535	14880	1.18
WR-674-001	14759	14842	0.56	45.03084	2.169	4.556	14949	1.29
KC-698-001	14807	14823	0.10	44.90547	2.194	4.571	14997	1.28
WR-627-001	14731	14760	0.19	44.49510	2.163	4.535	14880	1.01
WR-584-WR001	14780	14785	0.03	45.51061	2.166	4.591	15063	1.91
WR-543-001-BP1	15152	14788	-2.46	44.67277	2.167	4.557	14951	-1.33
WR-460-001	14935	14870	-0.43	45.28575	2.184	4.558	14953	0.12
KC-414-001	14880	14817	-0.42	43.53125	2.167	4.487	14772	-1.06
WR-372-001	14755	14758	0.02	44.48992	2.163	4.535	14879	0.84
WR-316-001	14745	14845	0.68	45.10600	2.168	4.561	14965	1.49
WR-278-001	14836	14801	-0.23	44.75014	2.166	4.545	14912	0.51
KC-292-001-BP1	14925	14703	-1.49	44.52185	2.166	4.534	14874	-0.34
WR-95-001	14965	14864	-0.67	45.17242	2.171	4.561	14965	0.00
KC-244-001-ST1	14549	14570	0.14	42.67723	2.147	4.485	14713	1.13
WR-155-001-ST1	14388	14374	-0.09	40.88842	2.130	4.484	14709	2.23
WR-143-003	14706	14483	-1.52	44.37502	2.165	4.544	14908	1.37
WR-96-001-BP1	14762	14556	-1.39	44.65621	2.1586	4.554	14942	1.22
KC-102-001	14475	14405	-0.48	43.54263	2.129	4.518	14823	2.40
WR-70-001	14595	14571	-0.16	42.77186	2.147	4.463	14643	0.33
KC-57-001	14751	14724	-0.18	43.95623	2.157	4.514	14810	0.40
WR-52-001-BP2	14459	14394	-0.45	41.23422	2.129	4.401	14438	-0.15
WR-30-001-ST2	14483	14367	-0.80	40.99352	2.120	4.392	14427	-0.39
GC-821-001	14669	14697	0.19	41.89026	2.139	4.495	14748	0.54
KC-511-001	16348	15623	-4.43	52.7718	2.199	4.882	16014	-2.04
KC-93-001	15223	15073	-0.98	46.59398	2.222	4.589	15054	-1.11
GC-825-001-ST1	15000	14923	-0.51	45.55394	2.192	4.559	14956	-0.29
GC-955-002	18535	17810	-3.91	70.05401	2.623	5.168	16955	-8.52
GB-959-001	17544	16367	-6.70	57.17716	2.472	4.974	16319	-6.98

Table 2.15. Wyllie Time Average derived velocities and Backus Average derived velocities compared to the measured salt V_{int}.

2.7 EVALUATION OF MINERALOGICAL MODELING

Plots were prepared for Hashin-Shtrikman bounds derived velocity variation of secondary minerals with halite at every 3% increment for anhydrite, gypsum, and sylvite. The same was done for both the Wylie Time-Average V_p and the Backus Average V_p and the results plotted along with the Hashin-Shtrikman results.

2.7.1 Wells plotted on the various bounds for a specific mineral component

The results are displayed in Figure 2.24 with anhydrite as the secondary component, in Figure 2.25 with gypsum as the secondary component and in Figure 2.26 with sylvite as the secondary component.

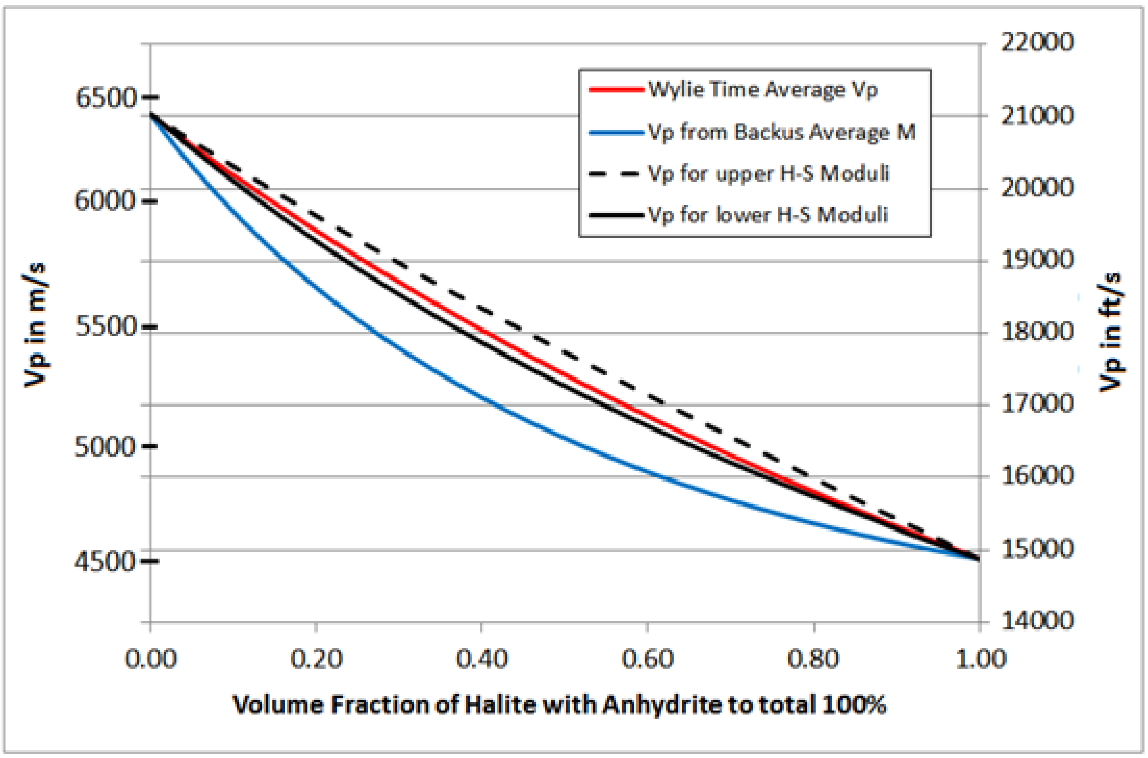

Figure 2.24. Variation of various bounds derived velocities versus the volume fraction of halite with anhydrite incrementing every 3%.

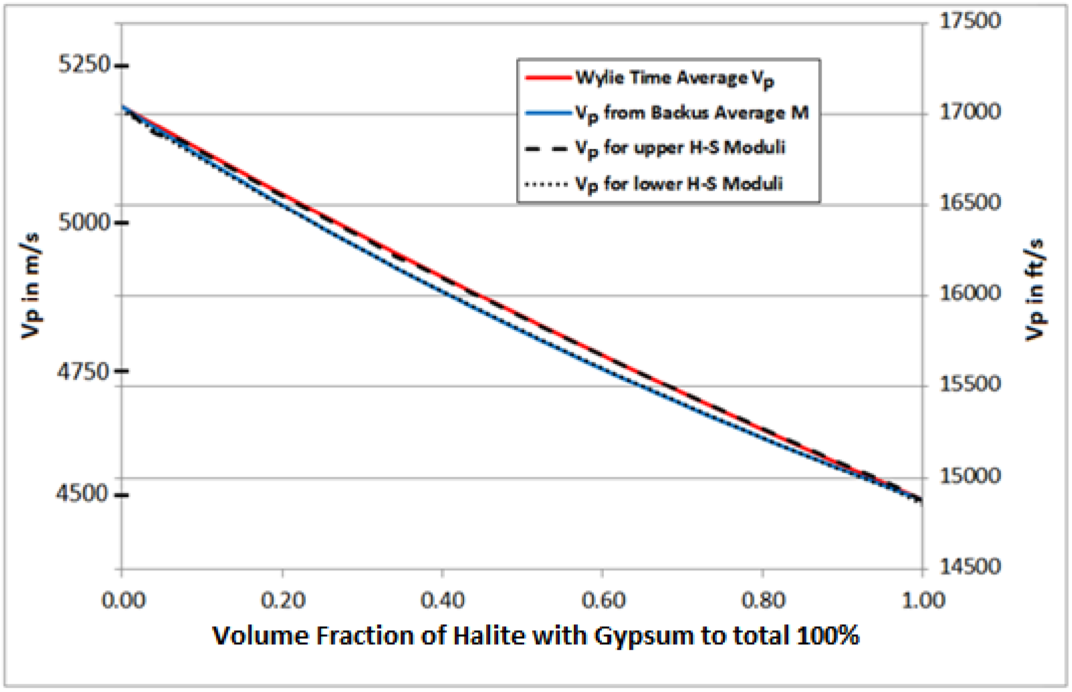

Figure 2.25. Variation of various bounds derived velocities versus the volume fraction of halite with gypsum incrementing every 3%.

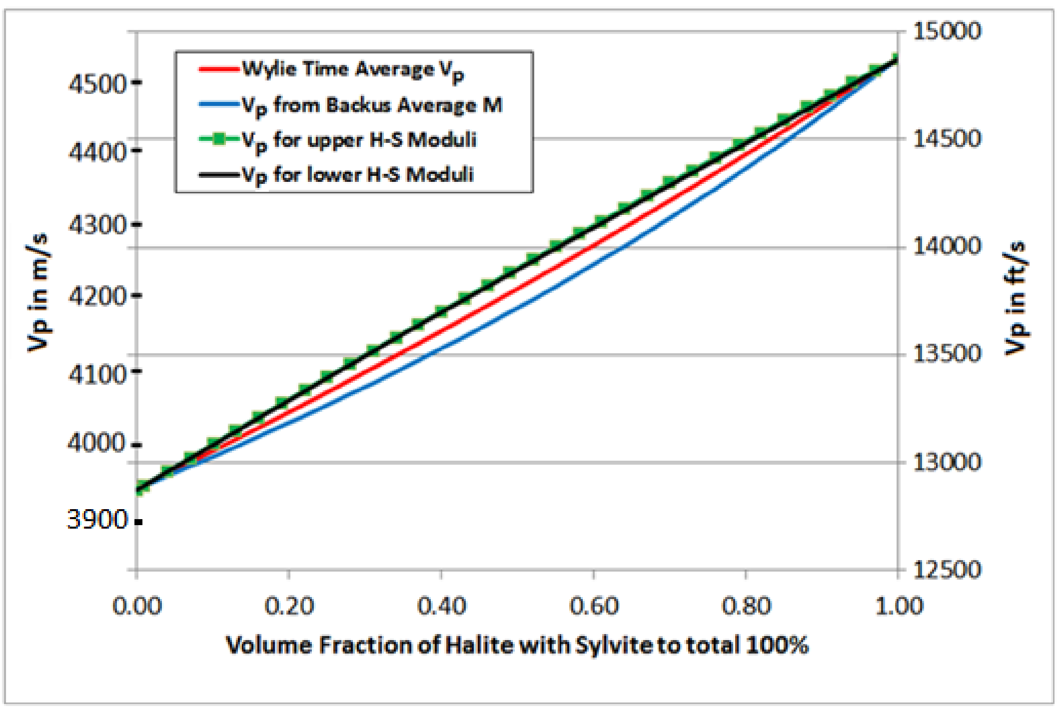

Figure 2.26. Variation of various bounds derived velocities versus the volume fraction of halite with gypsum incrementing every 3%.

Note that since sylvite has a lower V_p than halite, the plot in Figure 2.26 is turned the opposite direction from the plots of anhydrite and gypsum. In Figures 2.27, 2.28, and 2.29 the salt V_{int} from wells with the appropriate mineral component are plotted on top of Figures 2.24, 2.25, and 2.26, respectively.

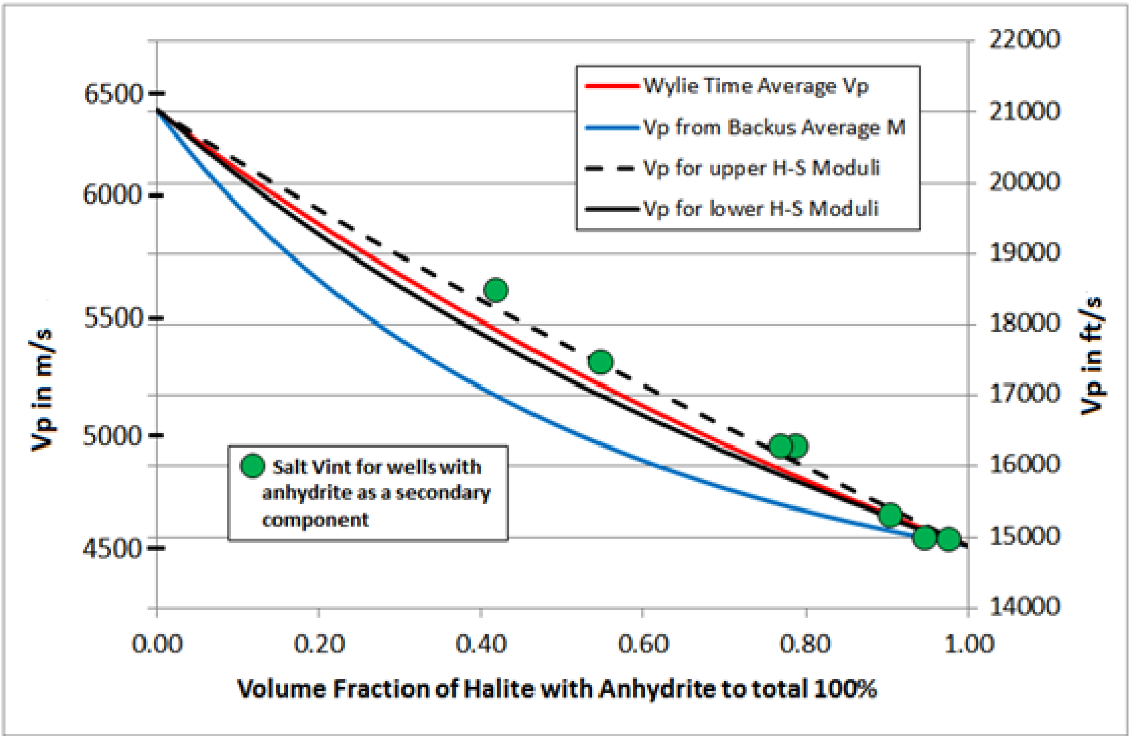

Figure 2.27. The same as Figure 2.24 with the salt V_{int} from wells having anhydrite as the secondary component superimposed.

Halite-anhydrite (Figure 2.27): In this case, due to the large difference in elastic properties of halite and anhydrite, there is a large spread between the various composite medium models. If the observations were accurate, the fact that the observed velocities follow the Hashin-Shtrikman upper bound would suggest that anhydrite is the pervasive interconnected matrix material. This is not plausible, suggesting that the anhydrite volumes greater than about 20% are underestimated. The conclusions to be drawn are (1) the magnitude of the velocity variation can be readily explained by any of these models, and (2) the data is not inconsistent with a rough linear relationship between anhydrite volume and velocity.

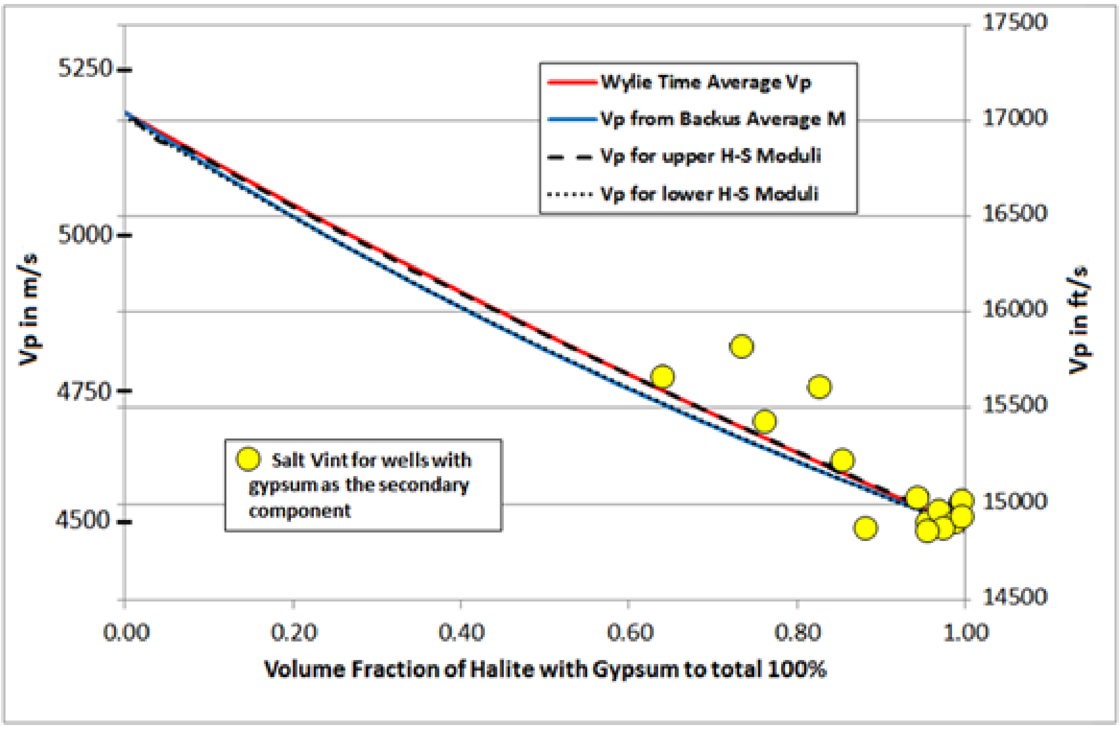

Figure 2.28. The same as Figure 2.25 with the salt V_{int} from wells having gypsum as the secondary component superimposed.

Halite-gypsum (Figure 2.28): In this case, the elastic properties of the end-member minerals are similar, so all the models converge suggesting a nearly linear relationship with composition. The scatter is increased, possibly due to the less accurate measurement of gypsum abundance, or that the velocity value from Table 8 is too low for deep borehole conditions. Once again, the observations suggest no reason to deviate from a linear relationship between gypsum composition and velocity.

Halite-sylvite (Figure 2.29): In this case, the H-S bounds converge to a nearly linear relationship and scatter in the points does not favor any one model over another.

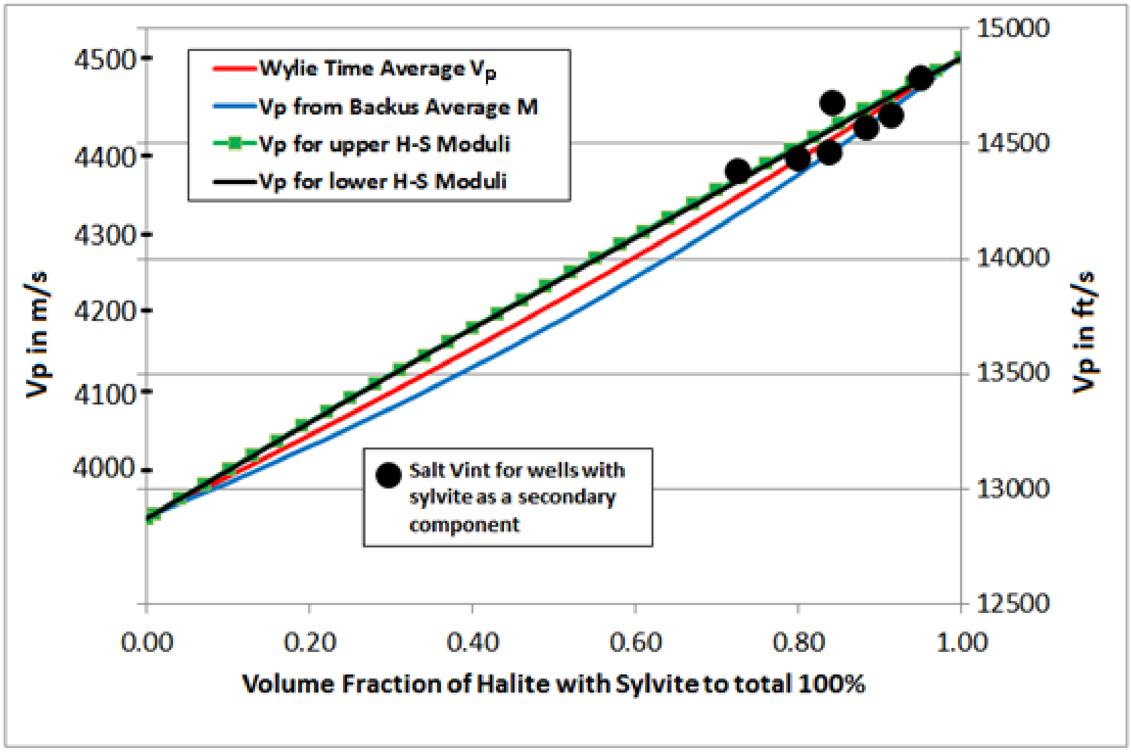

Figure 2.29. The same as Figure 2.26 with the salt V_{int} from wells having sylvite as the secondary component superimposed.

2.7.2 Regression analysis

From modeling of these binary mixtures, we can conclude that the observed velocity variation is of a magnitude that could readily be explained by compositional variation. We also find that the models and the spread in the observations suggest no reason to deviate from linear velocity-composition empirical relationships over the range of compositions studied. The nearly linear relationships between velocity and composition, both observed and modeled, suggests that it would be reasonable to empirically investigate the relationships in more complex mineralogies using a multiple linear regression approach. The multiple linear regression equation for the four evaporite components is:

(10) V_{int} (ft/s) = 14768.42 + 6918.101 X_{Anh} + 3305.146 X_{Gyp} - 1758.56 X_{Syl},

where V_{int} represents the salt interval velocity for the composite in ft/s, where $X_{\mathbf{Anh}}$ is the volume fraction of anhydrite, $X_{\mathbf{Gyp}}$ is the volume fraction of gypsum and $X_{\mathbf{Syl}}$ is the volume fraction of sylvite, and the intercept is the velocity for halite. The same regression equation in m/s is in equation (11):

(11) $V_{\mathbf{int}}$ (m/s) $= 4501.47 + 2108.66\ X_{\mathbf{Anh}} + 1007.42\ X_{\mathbf{Gyp}} + (-536.02)\ X_{\mathbf{Syl}}$,

where $R^2 = 0.976911$ for both versions, F = 412, and the significance of F is 2.45E-31.

Extrapolating to 100% of any given component gives regression velocities for the pure evaporites:

Halite.........14768.42 (±28.43) ft/s, or 4501.47 (± 8.66) m/s

Anhydrite....21686.52 (±207.38) ft/s, or 6610.13 (± 63.21) m/s

Gypsum......18073.57 (±290.35) ft/s, or 5508.89 (± 88.50) m/s

Sylvite........13009.86 (±361.30) ft/s, or 3965.45 (± 110.30m/s

The regression velocities are close to the values reported in Table 2.9, except for gypsum. The measured velocities for gypsum average 5.6% more than that in Table 2.9. If linearity is a good assumption, this suggests that the velocity for gypsum under these conditions is higher than laboratory measurements (perhaps due to partial dehydration) or the gypsum volumes are underestimated.

I conclude from mineralogical modeling and regression analysis, that the majority of the variance in the observed salt-body interval velocities can be explained by variations in salt-body composition. Next to consider is how the magnitude of the compositional effect compares to that of other factors that may affect salt-body velocities.

2.8 EXAMINATION OF OTHER POSSIBLE CAUSES OF VELOCITY VARIATION

I now investigate the variation in the depth to the top of salt, variation of salt-body V_{int} with longitude, with increasing temperature or with increasing pressure, and make comparisons to laboratory measurements in relatively pure halite. The question is: "How much of a contribution, if any, do these factors make?"

2.8.1 Depth to the top of salt-body

The allochthonous salt canopy in the study area has considerable variation in both depth and thickness. As body-wave velocities are commonly depth dependent, I want to be sure that compositional variations with depth of the salt body do not introduce a false correlation between velocity and composition. Figure 2.30 is a plot of measured borehole P-wave velocity (V_p) taken in intervals reported as almost pure halite, over a wide depth range in 13 wells. When salt mineral composition is constant over a few thousand feet range in the borehole, the salt velocity remains constant and does not increase with depth**.** This is what one would expect in a zero-porosity mineral assemblage over the temperature and pressure ranges in this area. I conclude that depth-dependence is not a major influence on the salt-body velocities.

This is similar to a salt study conducted by Zong (2017, in press) wherein sonic logs in salt were measured for 141 wells in shallow water (<1000 ft) on the continental shelf of the GoM, plus four deepwater wells. Zong assumed all the offshore salt was at least 95% halite. This is truer on the continental shelf than for the lower continental slope in this study area. In this work, entirely in the deepwater, only nine wells out of 44 contain 95% (or more) halite. Zong's V_p versus depth trend, generated by a least-squares fit, is plotted in Figure 2.29 with a red line.

The dashed black line is a linear regression done for the 88 points plotted from my data. Note that multiple points from the same well plot a straight line (blue dots). Given the scatter in both datasets, the subtle difference in these two trends is probably not significant.

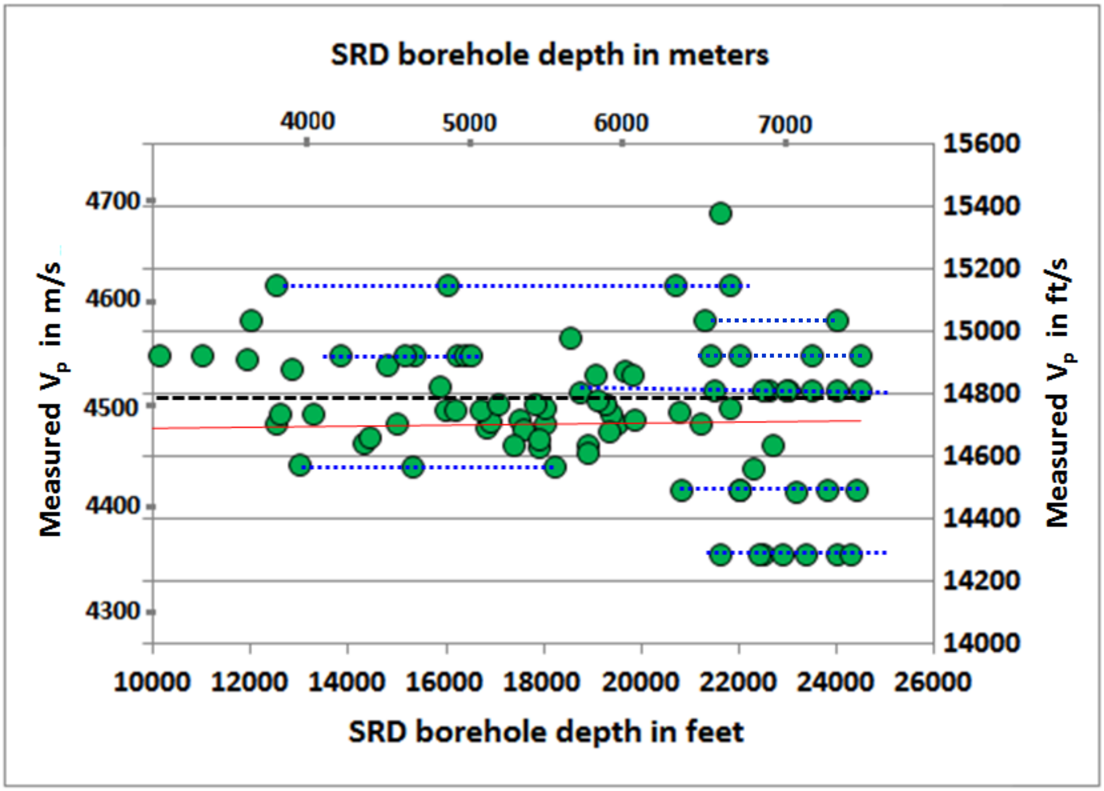

Figure 2.30. Measured borehole salt V_p vs. depth of measurement for zones reported as almost pure halite (per mudlogs) for 88 points from 13 wells. The dashed black line is a linear regression showing halite V_p does not increase with depth, similar to Zong's (2016) predicted V_p subtle increase in depth for GoM salt-bodies (shown in red). The linear blue dots connect points from the same well and again emphasize the velocity consistency with increasing depth. SRD (seismic reference datum) depth = sea level.

2.8.2 Correlation of salt-body V_{int} with longitude

Another obvious question is "If there is correlation of salt V_{int} with latitude, is there also a correlation with longitude?" Figure 2.31 is a plot of salt V_{int} from both seismic and well data plotted against decimal longitude and the distribution appears random, or without correlation.

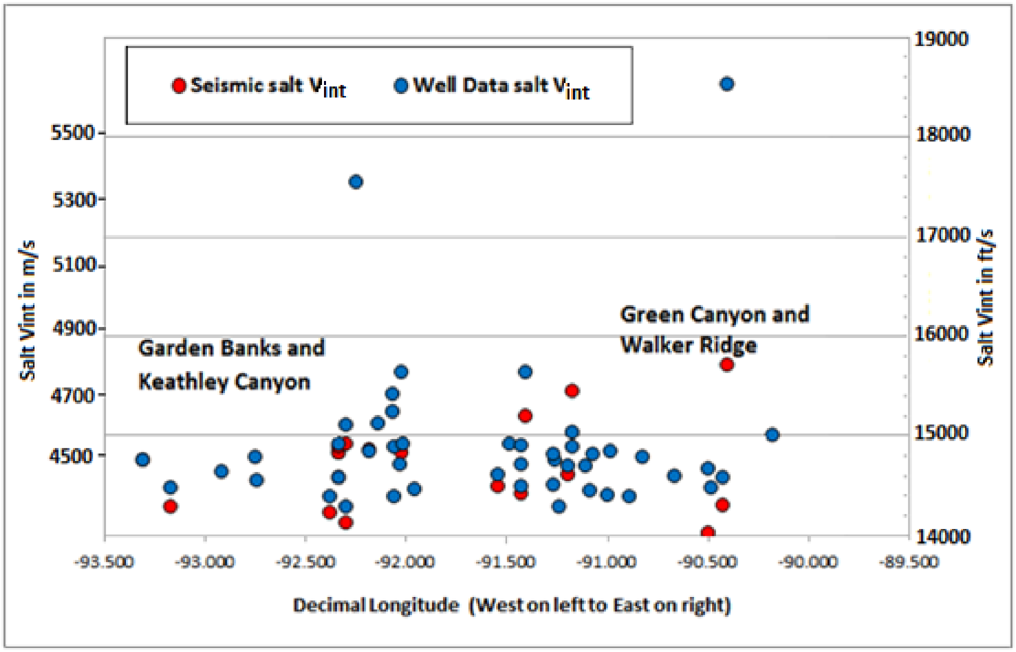

Figure 2.31. Salt V_{int} from both seismic and well data versus decimal longitude.

2.8.3 Variation of salt-body V_{int} with temperature

Both temperature and pressure affect body-wave velocities, so both temperature and overburden pressure were examined to see if variations in these could account for the observed variations in velocity. For the 63 wells having published information on the bottom-hole temperature (BHT), well-bore temperature gradients were calculated for sediments below the sea floor (mudline) down to the well's true vertical total depth (TVD), including the transit through salt (see Table 2.15.) A government report posted on www.bsee.gov states that although isolated salt diapirs on the continental shelf or the upper continental slope cause highly variable heat flow values due to the high-heat conductivity of salt, laterally continuous, sheet-like salt deposits (canopies) in the deepwater areas of the lower slope do NOT affect vertical heat flow. Most canopy-like salt has completely disengaged from the base autochthonous salt. The test here is if the salt is more horizontally spread than it is in vertical extent, then there is no effect; and this is definitely true for the study area where a large salt canopy covers most of the area in the subsurface.

Borehole temperature measurements do not treat salt any differently than the surrounding sediments partly because of the immersion of the measuring tool in drilling fluids. There is a scarcity of data from deepwater wells including sufficient temperature measurements along the borehole to do Horner plots needed to determine the true formation temperature at the bottom of the hole (Hyodo and Takasugi, 1995), (Peters and Nelson, 2009), and (Christie and Nagihara, 2015). Therefore, the true formation temperature (BFT) at the bottom of the borehole was estimated by adjusting the BHT upward by 10% in order to approximate the BFT. This is based upon having one well with both a BFT and a BHT and a reference (Forrest, 2007). The mean annual water temperature for the northern Gulf of Mexico is 40°F (4.44°C) for water depths greater than 3,900 feet (1189 meters) and it is consistent down to the mudline, regardless of water depth. The Walker Ridge area has the coolest temperature gradients (based only on six wells drilled before 2004) in the northern Gulf of Mexico (see Figure 2.34). The basic equation for the calculation of the wellbore temperature gradient in the Gulf of Mexico is:

$$(11) \quad \text{Wellbore temperature gradient} = \frac{\text{Formation temperature} - \text{mean annual water temperature}}{\text{Formation depth} - \text{water depth}}$$

and was offered, as it appears here (Forrest, 2007). There is an inherent depth dependency in equation (11) because: 1) of the inability to produce wellbore temperature gradients based upon Horner plots, and 2) the range of depths at the bottom of the hole. True vertical depths at the bottom of these wellbores can vary between 15,000 ft (4572 m) and 35,000 ft (10,668 m), resulting in varying temperature gradients based in part on the depth in the well that the one temperature measurement that was taken. If all the wells had similar depths, then the contour map would be meaningful. Even so, it is interesting, if not instructional, to look at these temperature gradients displayed in a contour map as shown in Figure 2.32. The wellbore temperature gradient calculations for 63 wells are displayed in Table 2.16. Figure 2.33 shows

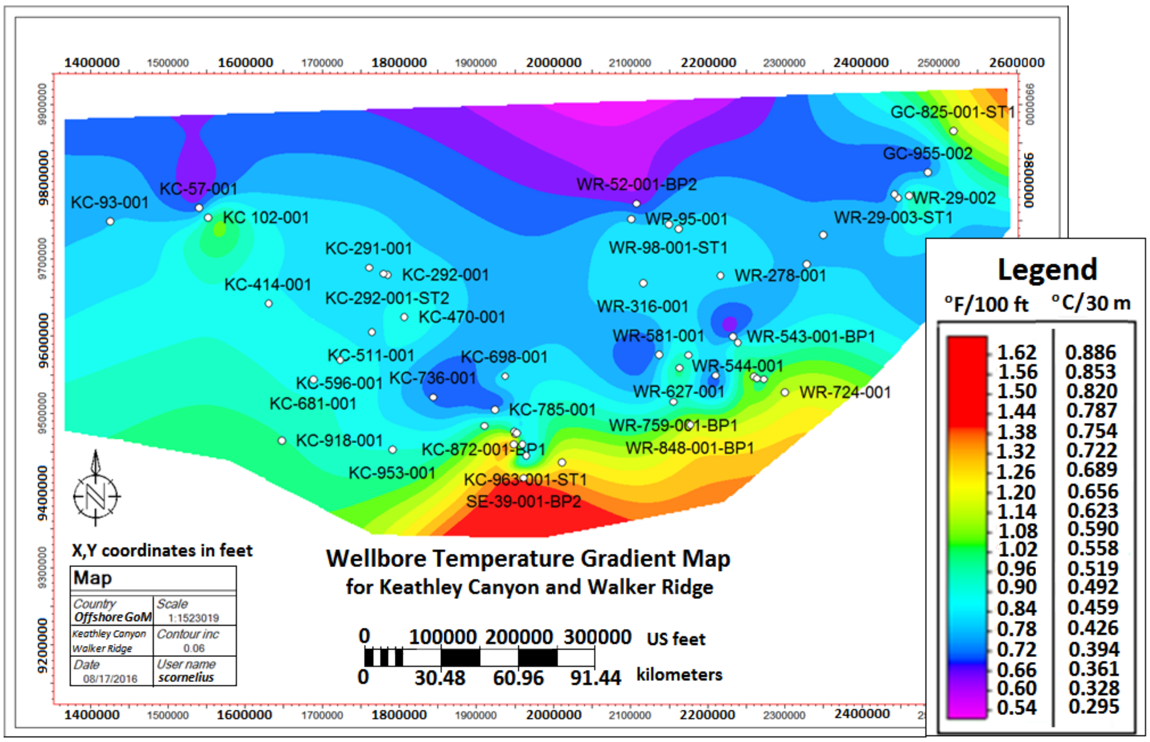

Figure 2.32. A wellbore temperature gradient map of the study area based on the estimated formation temperature with BHT data. Note the large rise in the temperature gradient at the southern edge of the Sigsbee Escarpment.

the lack of correlation between calculated borehole temperature and sonic log halite velocities. The linear regression for that plot yields a minimal dependence on temperature:

(12) $V_p = -.6718\ T + 14883$ in English units, or $= -.2075\ (T - 17.778) + 4536$ in metric units,

where V_p is halite compressional-wave velocity in ft/s (or m/s) and T is the estimated formation temperature in degrees Fahrenheit. R^2 is .0049 and with an F-test of .07 indicating that the scatter in the data is far greater than the variation captured by the trend. The conclusion is that there is no significant observable salt-body velocity variation with borehole temperature.

Well name	KB (ft)	water depth ft	Dec Lat	Top salt ft	Base salt ft	Salt thickness (ft)	BHT deg F	Estimated BFT deg F	TVD depth (ft)	Temp gradient °F/100 ft
GC-821-001	88	3944	27.156	5112	23998	18886	174	191	23998	0.7583
GC-825-001-ST1	91	5066	27.161	7215	9885	2670	207	228	22461	1.0847
GC-955-002	82	7278	27.015	16320	19195	2875	161	177	25573	0.7528
KC-10-001	92	3958	26.958	6825	25998	19173	235	259	30173	0.8364
KC-57-001	86	4065	26.909	7934	26264	18330	214	235	31320	0.7192
KC-93-001	84.3	4853	26.863	8190	24223	16033	198	217	27463	0.7828
KC 102-001	75	4132	26.878	8485	24980	16495	298	328	35051	0.9331
KC-244-001	75	5431	26.729	24356	24623	267	223	245	29601	0.8520
KC-291-001	86	5765	26.699	7932	25954	18022	230	253	31444	0.8323
KC-292-001	75	5859	26.674	10300	17900	7600	126	139	17900	0.8240
KC-292-001-ST2	75	5859	26.674	10300	24639	14339	225	248	32432	0.7831
KC-292-001-BP1	75	5859	26.674	10300	24614	14314	231	254	32475	0.8067
KC-292-002	86	6031	26.677	10342	25291	14949	227	250	31375	0.8302
KC-414-001	92	5515	26.570	8445	20240	11795	228	251	30057	0.8622
KC-470-001	85	6052	26.522	14780	22880	8100	235	259	30851	0.8841
KC-511-001	80	6120	26.470	13290	22240	8950	216	238	30003	0.8301
KC-596-001	85.5	6397	26.371	19040	21310	2270	225	248	29634	0.8963
KC-681-001	91	6345	26.300	9360	21662	12302	209	230	27553	0.8993
KC-698-001	92	6313	26.309	8270	23350	15080	196	216	28279	0.8028
KC-736-001	92	6738	26.236	7900	21700	13800	190	209	30379	0.7177
KC-785-001	92	6594	26.191	18585	20315	1730	180	198	27999	0.7413
KC-872-001-BP1	104	6921	26.133	8320	19410	11090	234	257	29400	0.9716
KC-874-ss001	84	6822	26.104	12220	17240	5020	157	173	19082	1.0898
KC-875-001-ST1	87	7103	26.113	12040	16380	4340	146	161	19556	0.9753
KC-875-002	82	6903	26.107	12022	16038	4016	130	143	18066	0.9295
KC-918-001	81	7471	26.113	12745	16071	3326	139	153	19141	0.9742
KC-919-001	75	7307	26.066	8340	17664	9324	211	232	27973	0.9329
KC-919-002	85.5	7367	26.066	12910	15970	3060	163	179	18754	1.2326
KC-953-001	92	7030	26.049	9900	16895	6995	142	156	19891	0.9100
KC-963-001-ST1	83.6	7583	26.025	12680	13648	968	118	130	17916	0.8761
SE-39-001-BP2	106	8559	25.947	9713	12342	2629	277	305	28673	1.3230
WR-29-002	72	5283	26.927	8740	12305	3565	178	196	25127	0.7880
WR-29-003-ST1	72	5232	26.927	8600	17525	8925	175	193	25287	0.7631
WR-30-001-ST2	83	6556	26.934	14782	27972	13190	215	237	27972	0.9211
WR-51-002	86	5841	26.909	6681	26377	19696	165	190	28806	0.6556
WR-52-001-BP2	82	5819	26.920	7040	28273	21233	190	209	31405	0.6626
WR-70-001	75	5505	26.895	8360	18968	10608	171	188	27901	0.6631
WR-95-001	47	5848	26.515	6410	23730	17320	162	178	23730	0.7749
WR-96-001-BP1	104	5860	26.873	5856	28273	22417	237	261	33560	0.7977
WR-98-001-ST1	82	6128	26.505	12350	24990	12640	230	253	32864	0.7991
WR-143-003	92	5768	26.836	11475	25220	13745	200	220	28430	0.7975
WR-155-001-ST1	80	5906	26.799	11040	22150	11110	185	204	27582	0.7571
WR-278-001	85.5	6464	26.661	6885	24968	18083	227	250	31845	0.8290
WR-285-001-BP1	79	6733	26.695	9178	19159	9981	164	180	24659	0.7867
WR-316-001	92	6175	26.636	6950	26038	19088	234	257	32609	0.8253
WR-372-001	91	6288	26.599	8140	19380	11690	214	235	30584	0.8073
WR-460-001	81	6986	26.519	10254	17708	7454	150	165	21900	0.8381
WR-469-001	83	8831	26.515	No salt	No salt	No salt	238	262	27543	1.1864
WR-543-001-BP1	106	6606	26.441	9716	24760	15044	182	200	28689	0.7289
WR-544-001	88	6844	26.421	9904	23598	13694	216	238	29628	0.8706
WR-581-001	72	6924	26.421	8700	24016	15316	185	204	28412	0.7634
WR-584-WR001	82	7219	26.380	12004	22403	10399	226	249	30495	0.8994
WR-627-001	75	7068	26.333	10300	21823	11523	240	264	30120	0.9749
WR-674-001	81	6812	26.305	11509	19191	7682	132	145	21384	0.7260
WR-677-001	92	6895	26.299	8525	19492	10967	245	270	28479	1.0678
WR-678-001-BP1	91	7036	26.289	8600	17000	8400	217	239	26795	1.0103
WR-678-002	91	6853	26.292	8750	18750	10000	230	253	29012	0.9652
WR-724-001	88	7545	26.242	8960	14130	5170	266	293	29845	1.1372
WR-758-PS005	92	6965	26.207	<10550	19840	>9290	260	286	28263	1.1600
WR-759-001-BP1	92	6965	26.213	8516	19654	11138	220	242	29000	0.9206
WR-848-001-BP1	82	7638	26.130	10034	15346	5312	253	278	28842	1.1268
WR-969-001	92	7755	25.600	14170	17792	3622	254	279	27391	1.2249

Table 2.16. Borehole temperature gradients for 63 wells in the study area.

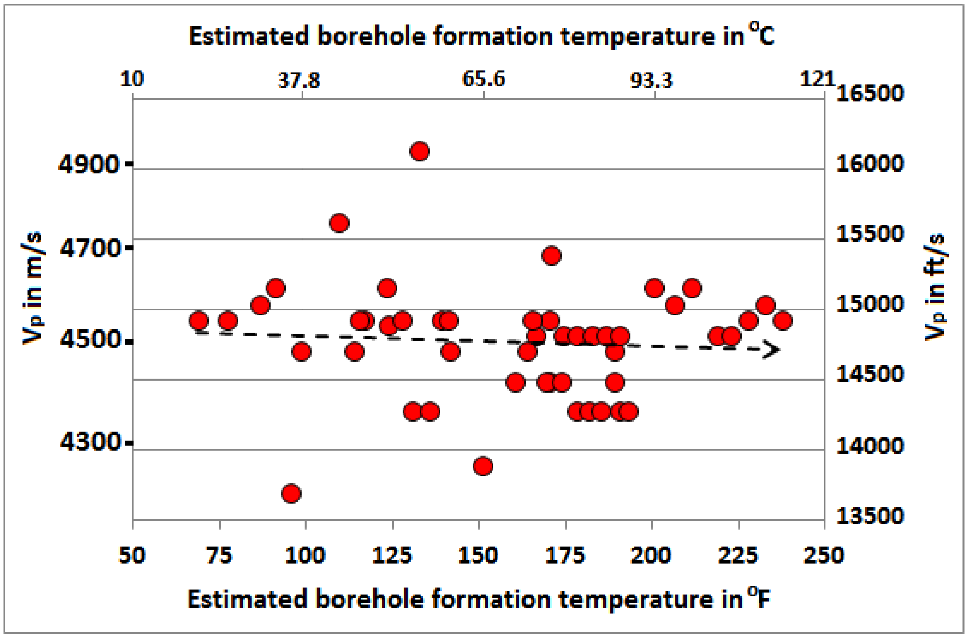

Figure 2.33. Sonic log V_p vs. borehole temperature both in °F and in °C for salt intervals that are nearly 100% halite showing that borehole temperature can account for very little of the velocity variation. The dashed blackline is a linear regression.

Figure 2.34 is a geothermal map of the GoM from Forrest (2007) that was based on only six wells within the study area outlined in black. In general, blue colors imply cooler temperature gradients (for greater depths required to reach 300°F) and red colors imply warmer temperature gradients (for shallower depths to reach 300°F). This map is not to be compared with Figure 2.32 because they illustrate two very different things. Forrest's contour map shows the depth at which a certain temperature is reached (300°F).

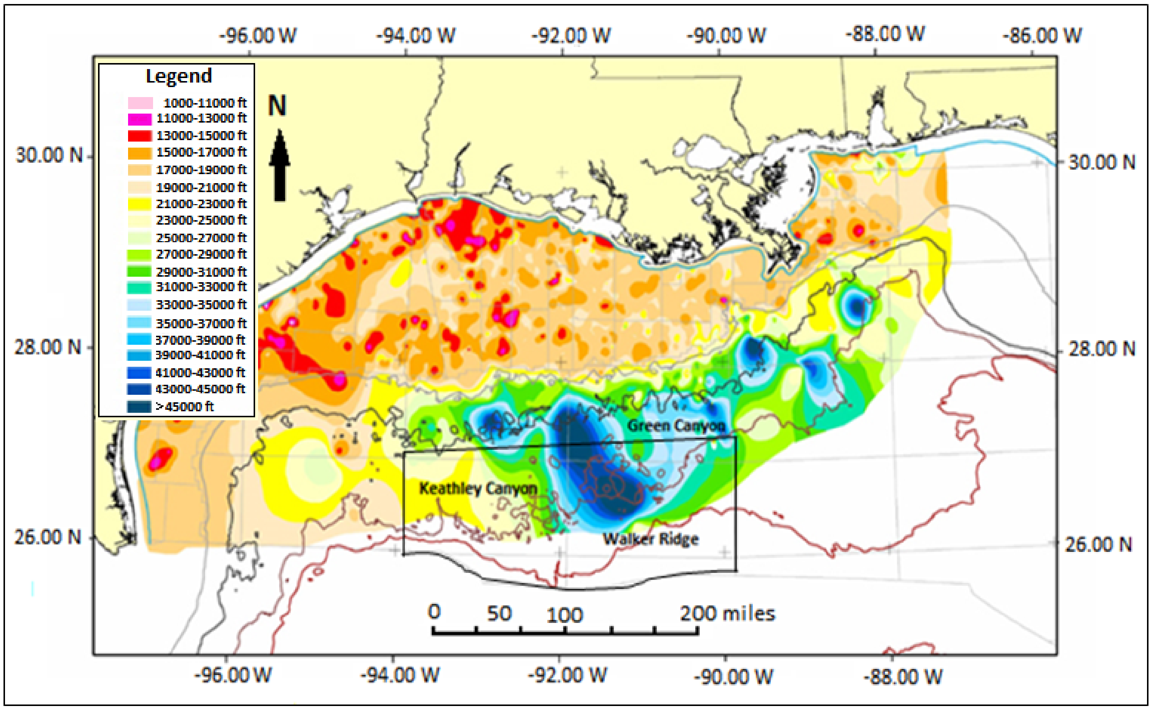

Figure 2.34. Map of interpreted depth below mudline at which 300 °F is reached in the offshore Gulf of Mexico. Cooler temperature gradients are in blues and higher temperature gradients are in orange- to red- to pink colors. Study area is inside black box. (After Forrest, 2007).

The well bore temperature gradients are plotted against the decimal latitude in Figure 2.35. There appears to be no correlation since there are multiple gradient values at all latitudes. However, there is a clustering of eight wells inside a circle between 26.60 and 26.70 degrees latitude where all of these wells are in salt group 3, meaning these eight salt compositions contain over 95% halite with a few percent of either anhydrite or gypsum plus minor constituents of shale, sandstone, sylvite, or tar. The average salt V_{int} of Group 3 is 14830 ft/sec (4520 m/sec).

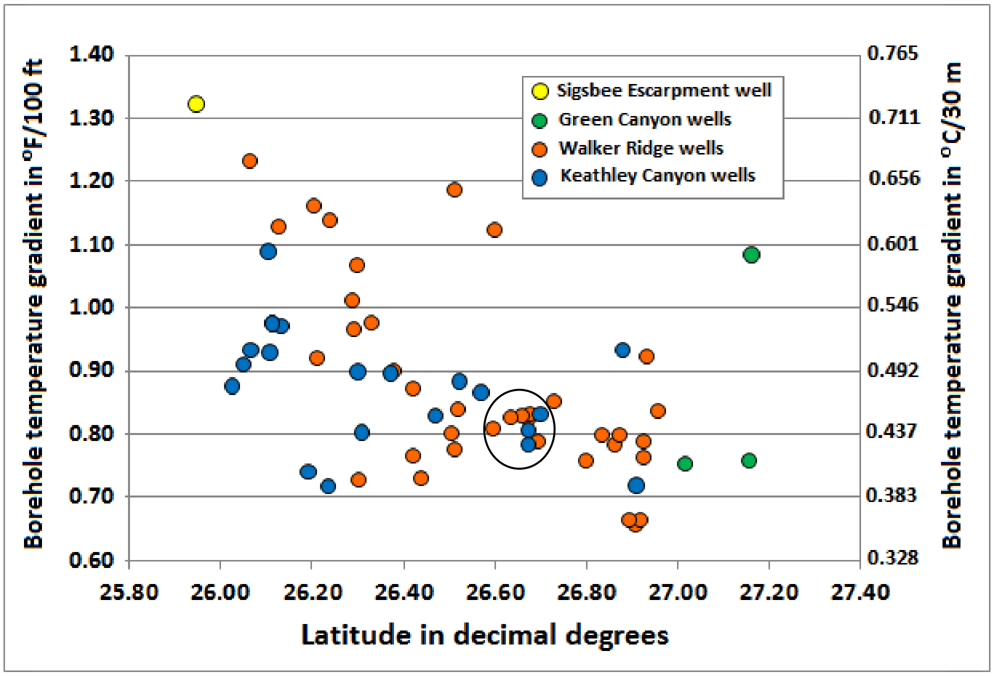

Figure 2.35. Borehole temperature gradients in 61 wells from seafloor to the TVD bottom of the well (including the salt matrix) plotted against latitude in decimal degrees. Some of the Group 3 wells are clustered inside the black circle. There is no correlation with latitude as there are multiple values for the same latitude.

2.8.4 Variation of salt-body V_{int} with pressure

The bottom hole mud weights in pounds per gallon (PPG) were collected for 66 wells and converted to psi/ft. Not all wells in the study area reported the final mud weight and this was true in some cases for the most recent wells where only a mudlog and a deviation survey were available. There is a slight linear trend in Figure 2.36 that plots the bottom hole mud weight versus the total true vertical depth. It shows a scattering of points in the shallower wells and a tightening of data points with increasing well depth, which indicates that above 27,000 ft (8230 m) depth there is a wider variety in pore pressure. This is the opposite of temperature points plotted versus true vertical depth as they tend to scatter with increasing depth, as shown in Figure 2.37.

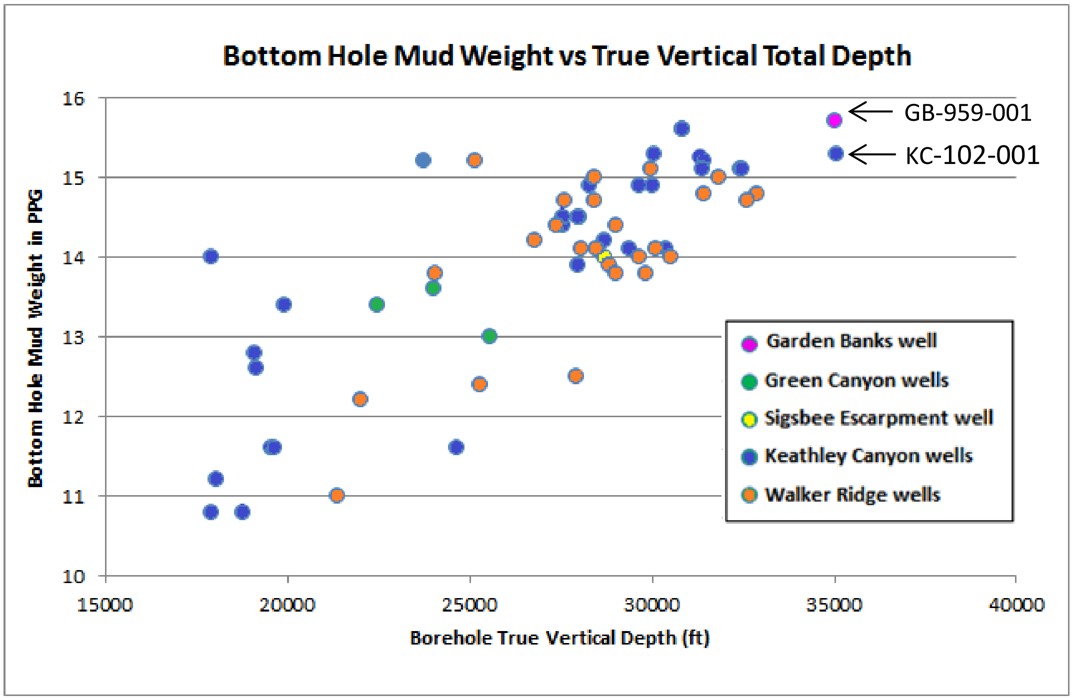

Figure 2.36. Bottom hole mud weights vs. the true vertical depth at bottom of the well. The deeper the well, the less scatter of mud weights reflecting bottom hole pressures.

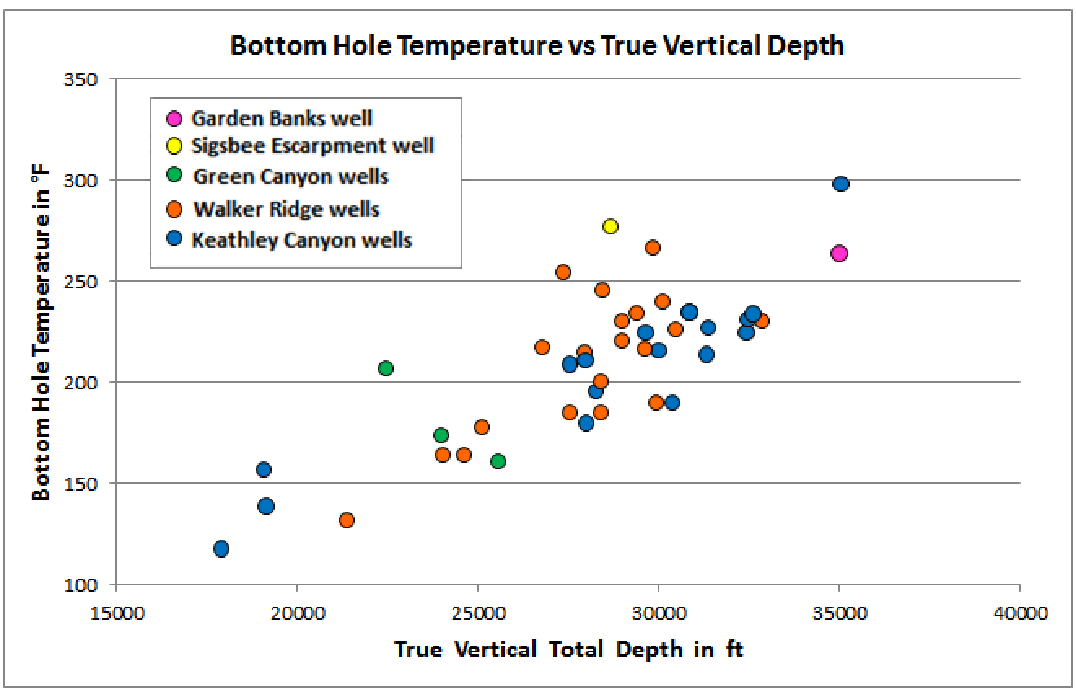

Figure 2.37 Bottom hole temperature vs. the true vertical depth at the bottom of the well. the deeper the well, the more scatter there is in temperature values.

An interesting fact related to pressures in a geological province that includes thick salt-bodies is that there is no pore pressure inside the salt due to zero porosity within the salt-body evaporites. So, calculating the overburden pressure at any depth point within the salt is shown in equation (13) in English units, and in equation (14) in metric units:

(13) Overburden pressure (psi) = (0.465 psi/ft *water depth in ft) + (depth between mudline and top of salt in ft) * (1.0 psi/ft) + (average density of salt converted to a pressure gradient) * (salt thickness in ft), or

(14) Overburden pressure (KPa) = (10.465 KPa/m *water depth in m) + (depth between mudline and top of salt in m) * (22.6026 KPa/m) + (average density of salt converted to a pressure gradient) * (salt thickness in m),

where it is assumed the lithostatic pressure gradient is the overburden pressure exerted by the sedimentary rocks overhead. This is a reasonable approximation for deepwater borehole conditions. The pressure gradient calculated within the salt was 0.9537 psi/ft (21.5561 KPa/m), assuming an average salt density of 2.2 g/cm^3. Figure 2.38 is a plot of the calculated overburden pressure at a variety of depths within the salt versus the sonic log-measured compressional-wave velocity at that same depth. The linear regression line in black shows any increase in velocity with increasing pressure is negligible over the great depth range of salt.

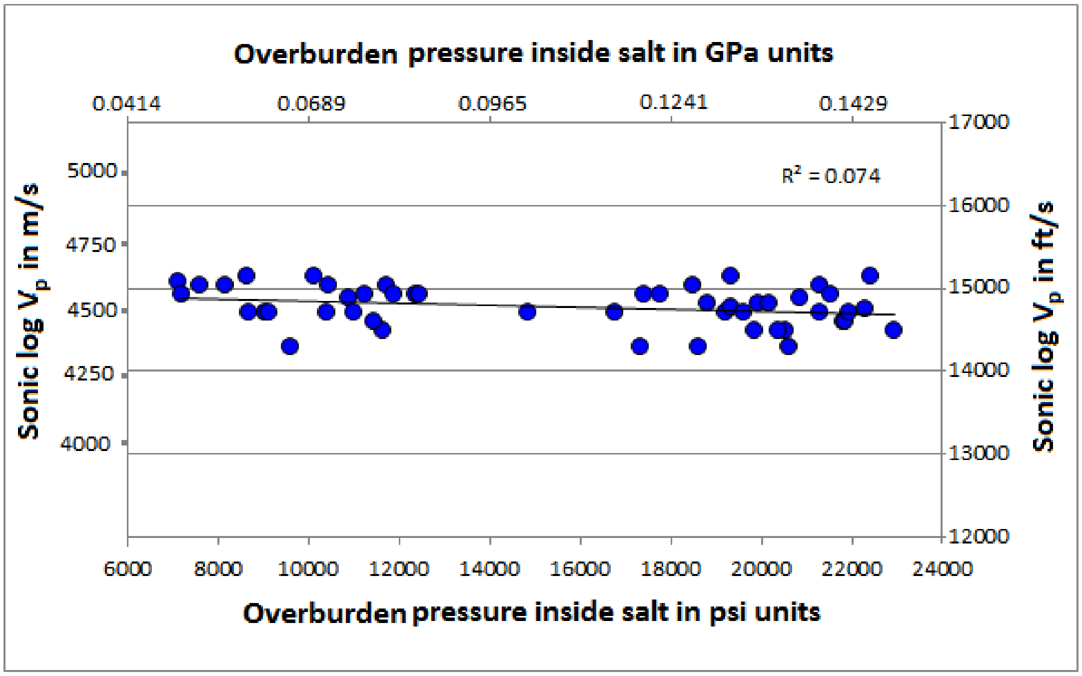

Figure 2.38. Overburden pressure within salt (almost pure halite) vs. the salt V_p measured by a sonic log at the same depth point, both in English units and in metric units. The black regression line shows there is minimal correlation between pressure and measured sonic log velocities.

Equation (15) represents the (bottomhole) mud pressure gradient (Schlumberger Oilfield Glossary, 2017) based on the bottomhole mud weight in psi/ft and equation (16) represents the same in metric units:

(15) Mud pressure gradient in psi/ft = Bottom hole mud weight in PPG * 0.052

(16) Mud pressure gradient in KPa/m = (Bottom hole mud weight in PPG * 0.052)/0.0442

Figure 2.39 shows the mud pressure gradients plotted against latitude resulting in two observable trends. Both trends show an increase in the pressure gradient from south to north, which is opposite of the velocity trend in Figures 2.5a and 2.5b that increases from north to south. This eliminates the possibility that the pressure gradients could be responsible for the

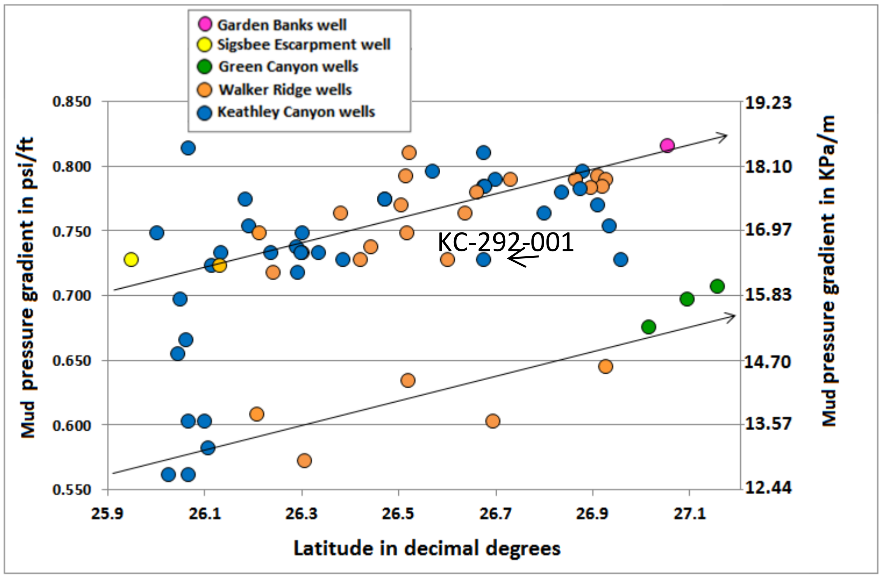

Figure 2.39. Bottomhole mud pressure gradients from 66 wells in study area plotted against latitude. Two different groups emerge: the upper group of wells trending towards the overpressure regime and the lower group in the moderate pressure regime.

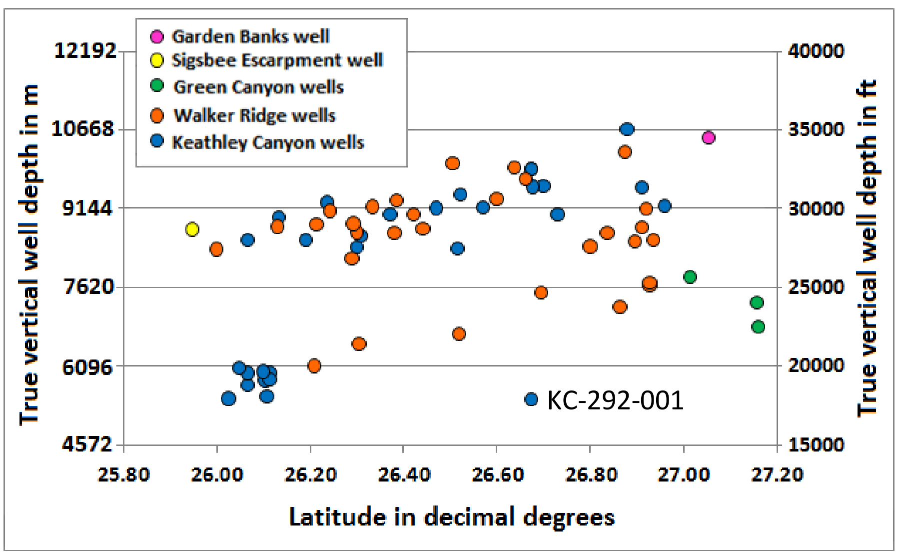

Figure 2.40. This is a simple plot of the TVD depth of all wells in the study area vs. the latitude in decimal degrees. In general, wells in the southern area are shallower than wells in the northern part of the study area.

velocity trend in the study area. In all borehole-pressure measurements, there is an inherent dependency on the depth of measurement; and this becomes an issue when comparing various pressures among wells in a local area. Figure 2.40 is a simple plot of true vertical depth at the bottom of the hole for all wells in the study area versus latitude in decimal degrees. At first glance, it looks similar to Figure 2.38 but a closer inspection of individual wells reveals the increase in pressure from south to north is not a false impression due to bias in well depth. Keathley Canyon wells really do have greater pressure than those in Walker Ridge for a given latitude. For example, look at the location of the KC-292-001 well in Figure 2.39 and again in Figure 2.40.

A plot showing that Keathley Canyon wells are more overpressured than Walker Ridge wells at the same latitude was presented by Green et al., 2014 as shown in Figure 2.41 showing that overpressure gradients increase from east to west from Green Canyon to Garden Banks and

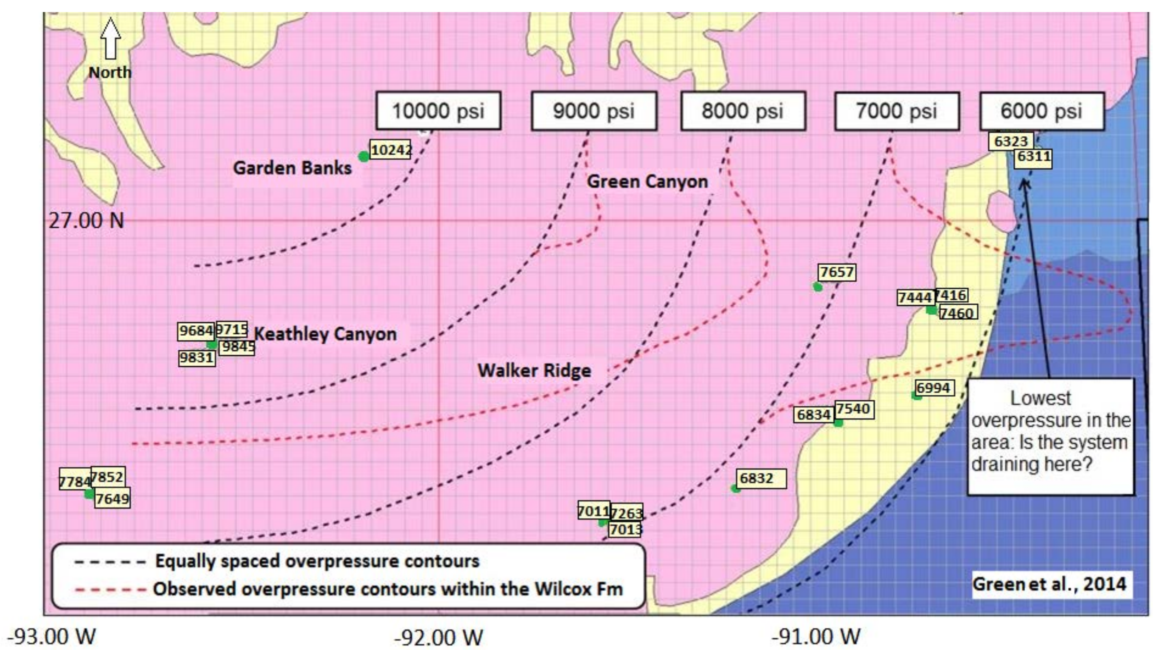

Figure 2.41. An overpressure map for the Wilcox reservoirs across eastern Keathley Canyon and Walker Ridge, and the southern blocks in Green Canyon and Garden Banks. The black dashed lines show equal-spaced contours and the red dashed lines show overpressure contours specifically for the Wilcox Formation. The lowest values are in Atwater Valley, to the east of Green Canyon, which has only produced a Wilcox gas discovery in its southwestern corner. The referenced author did not define the color scheme but Figure1.9 suggests that the pink color denotes Wilcox sand deposition and the pale yellow might be Pliocene-age sub-basins.

from Walker Ridge to Keathley Canyon, specifically for the Wilcox Formation. Overpressure, as used here, means abnormal pore pressure in excess of hydrostatic pressure. See Figure 1.8.

Figure 2.42 is a chart defining the pressure zones for the Gulf of Mexico Basin based on an exhaustive study done by the USGS for the southern half of Louisiana and the offshore out to the upper continental slope. Their study area did not include the area of this study but the trends observed in geopressure gradients are roughly the same, namely that they increase from south to north (Burke, et al., 2012).

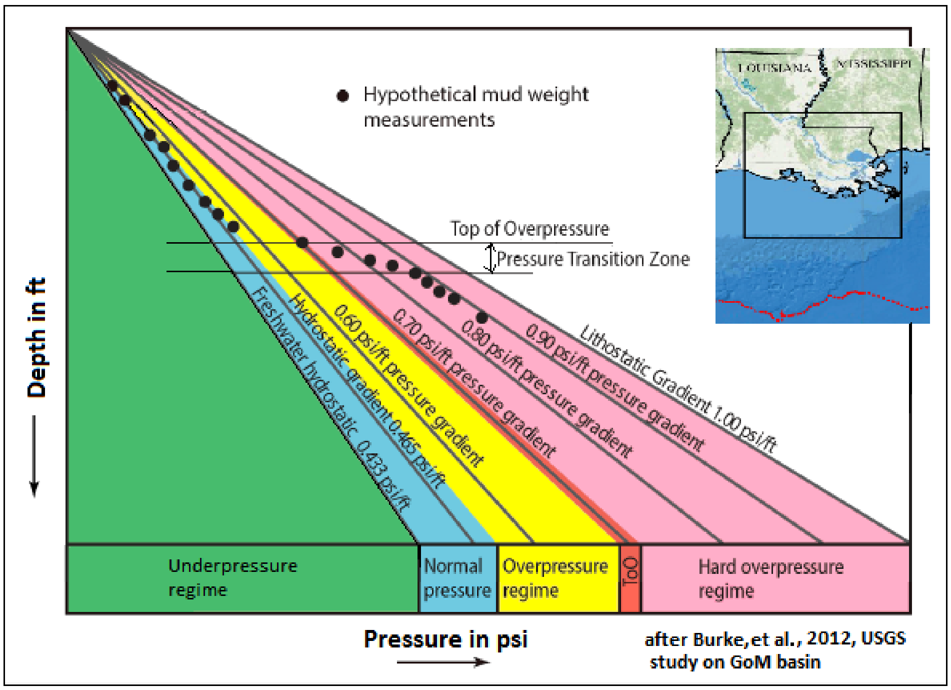

Figure 2.42. Pressure gradients defined for the Gulf of Mexico basin. The top of overpressure (ToO) is defined as 0.70 psi/ft.

Figure 2.43 is also from Burke, (2012) showing the depth required to reach the geopressure value of 0.70 psi/ft. This map shows these contours extending into this study area, but there is no mention of the data source for their derivation.

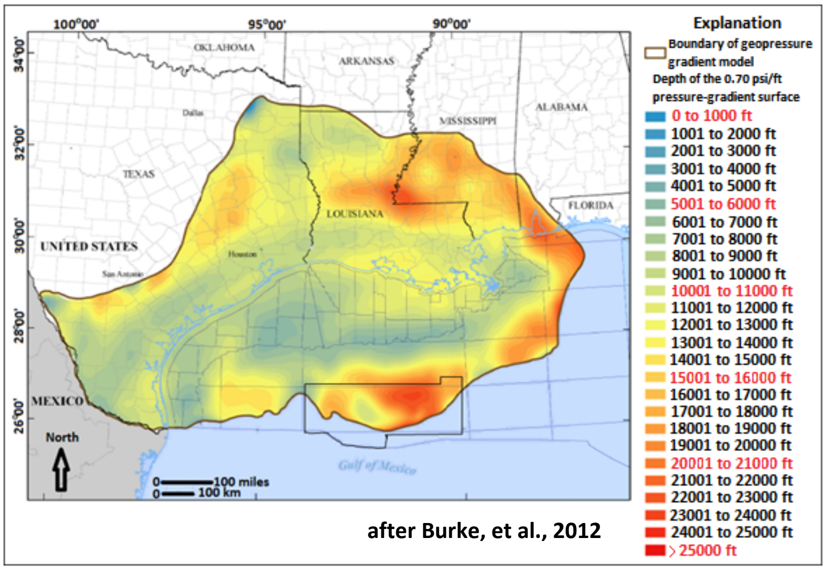

Figure 2.43. Map showing the regional distribution of the depth required to reach the 0.70 psi/ft geopressure gradient. For the study area, the geopressure gradient increases from south to north while the salt-body interval velocities decrease from south to north (Figure 2.5b).

Well name	API- UVI	Bottom MW in ppg	true vertical TD (ft)	Borehole pressure gradient psi/ft	Borehole pressure gradient Kpa/m
GB-959-001	608074030502	15.7	34499	0.816	17.463
GC-821-001	608114044800	13.6	23998	0.707	15.997
GC-825-001-ST1	608124003501	13.4	22461	0.697	15.762
GC-955-002	608114047700	13.0	25573	0.676	15.292
KC-10-001	608084004600	14.0	30173	0.728	16.468
KC-57-001	608084004100	15.25	31320	0.793	17.938
KC-93-001	608084003400	15.25	27463	0.793	17.938
KC 102-001	608084001500	15.3	35051	0.796	17.997
KC-244-001-ST1	608084001200	15.2	29601	0.790	17.879
KC-291-001	608084001700	15.2	31444	0.790	17.879
KC-292-001	608084001000	14.0	17900	0.728	16.468
KC-292-001-ST2	608084001104	15.6	32432	0.811	18.350
KC-292-001-BP1	608084001102	15.1	32475	0.785	17.762
KC-292-002	608084002700	15.1	31375	0.785	17.762
KC-414-001	608084005000	15.3	30057	0.796	17.997
KC-470-001	608054001900	15.6	30851	0.811	18.350
KC-511-001	608084000402	14.9	30003	0.775	17.526
KC-596-001	608084001300	14.9	29634	0.775	17.526
KC-681-001	608084000500	14.4	27553	0.749	16.938
KC-698-001	608084002600	14.9	28279	0.775	17.526
KC-736-001	608084002200	14.1	30379	0.733	16.585
KC-785-001	608084002100	14.5	27999	0.754	17.056
KC-872-001-BP1	608084001600	14.1	29400	0.733	16.585
KC-874-ss001	608084003300	12.8	19082	0.666	15.056
KC-875-001-ST1	608084002001	13.9	19556	0.723	16.350
KC-875-002	608084002400	11.2	18066	0.582	13.174
KC-918-001-ST1	608084003200	12.6	19141	0.655	14.821
KC-919-001	608084000600	13.9	27973	0.723	16.350
KC-919-002	608084001800	10.8	18754	0.562	12.704
KC-919-002-ST1	608084001802	11.6	19540	0.603	13.645
KC-919-003-BP1	608084002501	11.6	19628	0.603	13.645
KC-953-001	606084004200	13.4	19891	0.697	15.762
KC-963-001-ST1	608084001401	10.8	17916	0.562	12.704

Well name	API- UVI	Bottom MW in ppg	true vertical TD (ft)	Borehole pressure gradient psi/ft	Borehole pressure gradient Kpa/m
SE-39-001-BP2	608094000102	14.0	28673	0.728	16.468
WR-29-002	608124002000	15.2	25127	0.790	17.879
WR-29-003-ST1	608124002301	12.4	25287	0.645	14.586
WR-30-001-ST2	608124000600	14.5	27972	0.754	17.056
WR-51-002	608124007900	14.8	31405	0.770	17.409
WR-52-001-BP2	608124003402	15.1	29948	0.785	17.762
WR-70-001	608124000000	12.5	27901	0.650	14.703
WR-95-001	608124007800	15.2	23730	0.790	17.879
WR-96-001-BP1	608124009101	15.05	33560	0.783	17.703
WR-98-001-ST1	608124007601	14.8	32864	0.770	17.409
WR-143-003	608124008900	15.0	28430	0.780	17.644
WR-155-001-ST	608124002801	14.7	27582	0.764	17.291
WR-278-001	608124002500	15	31845	0.780	17.644
WR-285-001-BP	608124000901	11.6	24659	0.603	13.645
WR-316-001	608124003700	14.7	32609	0.764	17.291
WR-372-001	608124003000	14.0	28867	0.728	16.468
WR-460-001	608124008400	12.2	21999	0.634	14.351
WR-469-001	608124001000	14.4	26952	0.749	16.938
WR-543-001-BP	608124004500	14.2	28689	0.738	16.703
WR-544-001	608124002100	14.0	29628	0.728	16.468
WR-581-001	608124003500	14.7	28412	0.764	17.291
WR-584-WR001	608124003300	14.0	30495	0.728	16.468
WR-627-001	608124002400	14.1	30120	0.733	16.585
WR-674-001	608124008000	11.0	21384	0.572	12.939
WR-677-001	608124002900	14.1	28479	0.733	16.585
WR-678-001-BP	608124000401	14.2	26795	0.738	16.703
WR-678-002	608124001100	13.8	29012	0.718	16.233
WR-678-PS003	608124005600	14.1	28049	0.733	16.585
WR-724-001	608124001400	13.8	29845	0.718	16.233
WR-758-002	608124002700	11.7	19988	0.608	13.762
WR-759-001-BP	608124001301	14.4	29000	0.749	16.938
WR-848-001-BP	608124002601	13.9	28842	0.723	16.350
WR-969-001	608124004800	14.4	27391	0.749	16.938

Table 2.17. Borehole (mud) pressure gradients for 66 wells in study area. Wells included in the salt study are color-coded as to their group in Tables 3-7. Not all of these wells were included in the full analysis due to missing information. Some wells are missing mudlogs for salt composition and some wells are missing velocity information inside the salt.

2.8.5 Comparison to laboratory measurements in pure halite (Yan's equation)

Now that the thermal and pressure gradients have been determined for a majority of wells in the study area, it is possible to apply Yan's equation to derive V_p for rock salt if the temperature and pressure are known at a fixed point in the borehole. Yan's work was done in the Rock Physics Laboratory at the University of Houston using samples of onshore underground salt assumed to be pure halite. Based upon this detailed study of velocity anisotropy, salt matrix heterogeneity, and stress effects upon the salt; equation (17) was derived:

(17) $V_{\mathrm{p}} = 4.6910 - 0.01918\, e^{-0.05164\,\mathrm{P}} + 1.3265\times10^{-6}\,\mathrm{P\,T} - 0.001707\,\mathrm{T} + 2.3893\times10^{-6}\,\mathrm{T}^2$,

requiring the temperature T to be in degrees Celsius and the confining pressure P to be in MPa (Yan et al., 2014). Using an average overburden pressure (24456 psi or 168.62 MPa) over 66 wells, Yan's equation for both the maximum and minimum temperature range in the data, produced velocities of 14798 ft/s (4.510 km/s) and 15288 ft/s (4.660 km/s), respectively (see Table 2.18a). The spread between maximum and minimum velocity is 490 ft/s (0.150 km/s), which is small compared to the spread between the maximum salt V_{int} (18535 ft/s or 5.650 km/s) and the minimum salt V_{int} (14384 ft/s or 4.384 km/s) equal to 4151 ft/s (1.265km/s), or 11.8% difference (See Table 2.18b). Therefore, variations in temperature do not appear be the cause of such large velocity variations among the salt-bodies. Similarly, using the average temperature (198 °F or 92.2 °C) over 62 wells, Yan's equation was calculated for both the highest and the lowest overburden pressure in the data, producing velocities of 15030 ft/s (4.581 km/s) and 14940 ft/s (4.554 km/s), respectively. The spread between the high and low velocity is only 90 ft/s (0.027 km/s) or roughly 2.16% of the difference between the measured maximum and minimum salt $V_{\mathbf{int}}$. Again, the effect of pressure on the salt $V_{\mathbf{p}}$ is negligible.

Circumstance	temp °F	temp °C	Overburden pressure in psi	Overburden pressure in Mpa	TVD subsea depth in ft	TVD subsea depth in m	Yan's V_p in km/s	Yan's V_p in ft/s
highest temperature	328	164			35051	10684	4.510	14798
lowest temperature	68.9	20.5			10100	3079	4.660	15288
average OB pressure, temp	198	92.2	24456	168.62			4.574	15005
highest overburden pressure			40168	276.95	35051	10684	4.581	15030
lowest overburden pressure			8745	60.29	12023	3665	4.554	14940

Table 2.18a. Well data used in Yan's equation (15) and resulting velocities in English and metric units.

Units	Highest measured salt V_{int}	Lowest measured salt V_{int}	Yan's V_p from max temp with average pressure	Yan's V_p from min temp with average pressure	Yan's V_p from high pressure with average temp	Yan's V_p from low pressure with average temp
velocity in ft/s	18535	14384	14798	15288	15030	14940
velocity in km/s	5.650	4.384	4.510	4.660	4.581	4.554
range between high and low	4151 ft/s or 1.265 km/s		490 ft/s or 0.150 km/s		90 ft/s or 0.027 km/s	

Table 2.18b. Comparison of results among the various V_p calculations using Yan's equation under varying temperature and pressure conditions.

Figure 2.44 presents the same data shown in Figure 2.33, but with the addition of V_p values calculated from Yan's equation added in blue, using the same temperature- depth points; but the upper line is for a high-overburden pressure and the lower dashed line is for a low-overburden pressure found within the dataset. Yan's equation predicts higher velocities based upon laboratory conditions with controlled temperatures and confining pressures than what is observed under borehole conditions in the deepwater study area.

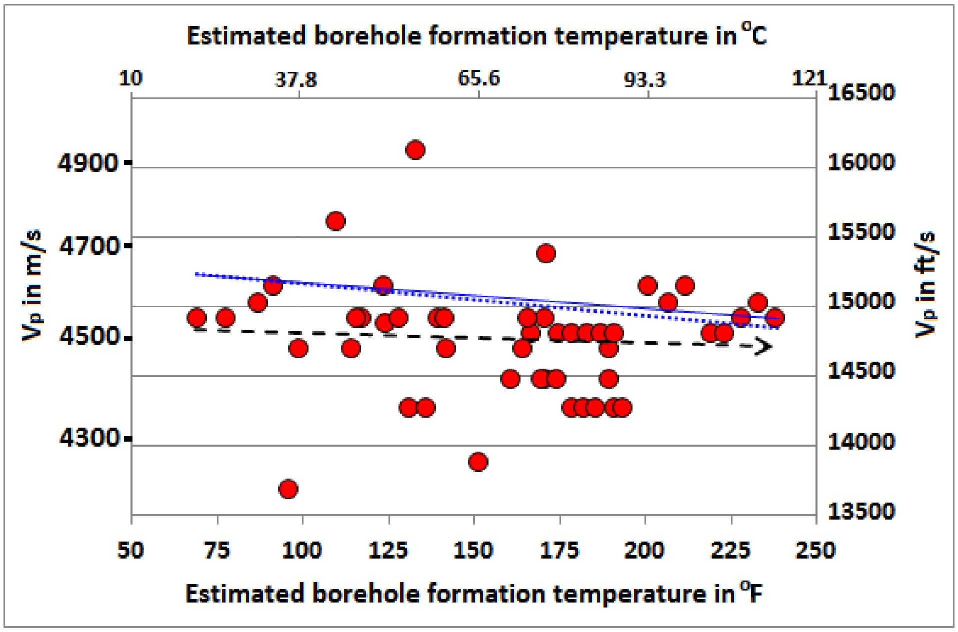

Figure 2.44. This is Figure 2.33 with V_p calculated from Yan's equation added in blue. Upper line is for a high pressure (26,309 psi or 181 MPa) found in the study wells and the dotted blue line is for a low pressure (6,000 psi or 41 MPa).

Averaging the sonic log salt V_p for 89 data points of 100% pure halite gives the average value of 14766 ft/s (4500 m/s, 4.5km/s), which is exactly the value used in Table 2.9, where Yan's work is a reference for the value. The standard deviation for this average velocity is 290.7 ft/s (88.6 m/s).

2.9 DISCUSSION

The most compelling argument for this variability of salt Vint vs latitude is its visual expression on the map presented in Figure 2.16. The five different salt groups in the study area show a distinct tendency for variation by latitude. The various mineralogical inclusions and the sediment intrusions change in abundance and type from north to south. There exists a chemical relationship between anhydrite and gypsum:

$$\underset{\text{Gypsum}}{CaSO_4{*}2H_2O} \rightleftharpoons \underset{\text{Anhydrite}}{CaSO_4} + \underset{\text{water}}{2H_2O}$$

The chemical relationship alluded to above implies that if anhydrite comes into contact with water, it could transform into gypsum, and that if gypsum is dewatered through an increase in temperature, it transforms back into anhydrite (Rolnick, 1954), (Ostroff, 1964) and (Klimchouk, 1996). But other observations bely a simple explanation. The geothermal gradients are the highest for Salt Group 1 wells to the far south, close to the southern edge of the Sigsbee Escarpment, and yet there is anhydrite reported in only one of these six wells. Therefore, no evidence is observed that this reaction is a controlling factor in the compositional variation in that part of the study area.

The two Group 5 wells with anhydrite that are more or less in the middle of the map (Figure 2.16) are an anomaly due to their significant volume fraction of anhydrite. With the available data, there is no way to know if the anhydrite present in these wells is converted gypsum, if the anhydrite has been acquired from ‘country rock” by salt movement basinward, or if this anhydrite was an original deposit. Many geological questions remain to be answered regarding how the mineralogical variations within the salt-bodies occurred, but the fact there are mineralogical variations that strongly correlate with variations in salt-body V_{int} is now believed to be well-documented in this data set.

It has been observed that the allochthonous salt bodies in the deepwater study area can have considerable variability in their mineralogy and associated compressional-wave velocities. This is important in constructing 3D velocity models for input into seismic processing. When possible, I suggest that it would be wise to examine the mudlogs of all wells in the prospective area for information on the local salt mineralogy.

2.10 CONCLUSIONS

There is significant variability in the interval velocity of bodies of Louann Salt in the deepwater GOM in and around Keathley Canyon and Walker Ridge, ranging from a minimum of 13884 ft/s (4232 m/s) to a maximum of 18535 ft/s (5650m/s). This variability is correlated to and most readily explained by variability in salt-body composition, which was qualitatively confirmed by mudlog descriptions. The latitudinal variation of velocity is associated with latitudinal changes in composition.

Composite medium modeling, in both binary and multicomponent mixtures, shows roughly a linear velocity variation with composition in the same direction and similar in magnitude to the observations. Multiple linear regression of observations in more complex salt mixtures provides a linear relationship between velocity and composition that explains most of the variance of the data with good statistical significance. Any contribution from the usual factors affecting the interval velocity of sediments (depth, temperature, and pressure) to the salt-body interval velocity is secondary. I conclude that the velocity variation with latitude can be explained by lithological variation with latitude.

2.11 REFERENCES

Alger, R. P. and Crain, E. R., 1966, Defining evaporite deposits with electrical well logs, Presented at Northern Ohio Geological Society, published in Symposium on Salt, **2,** 116-130.

Allwardt, J. R., et al*,* 2009, 2D modeling of overpressure in a salt withdrawal basin, Gulf of Mexico, USA, Marine and Petroleum Geology, **26**, 464-473.

Bell, F. G., 1981, Geotechnical properties of some evaporitic rocks, Bulletin of the International Assoc. of Engineering Geology, **24**, issue 1, 137-144.

Bőhlke, T. and Lobos, M., 2013, Representation of Hashin-Shtrikman bounds of cubic crystal aggregates in terms of texture coefficients with application in material design, Acta Materialia, **67**, 324-334.

Bos, L., et al, 2016, On Backus average for generally anisotropic layers, Physics-Geophysics, **1**, 1-21.

Brown, J. M., 2013, Determination of Hashin-Shtrikman bounds on the effective elastic moduli of polycrystals of any symmetry, http://earthweb.ess.washington.edu/brown/resources/HS_Determination.pdf, accessed 21 July 2016.

Burke, L. A., et al, 2012, Regional map of the 0.70 psi/ft pressure gradient and development of the regional geopressure-gradient model for the onshore and offshore Gulf of Mexico Basin, U.S.A., GCAGS Journal, **1**, 97-106.

Chang, C., et al, 2006, Empirical relations between rock strength and physical properties in sedimentary rocks, J. of Petroleum Science & Engineering, **51**, 223-237.

Christie, C. H. and Nagihara, S., 2015, Geothermal gradients of the northern continental shelf of the Gulf of Mexico, Geosphere, **12**, no.1, 26-34.

Cornelius, S., 2016, Salt interval velocities vs. latitude in the deepwater Gulf of Mexico: Keathley Canyon and Walker Ridge areas, Presented at the Fall Meeting, AGU.

DPDS, http://www.deepseadrilling.org/96/dsdp_toc.htm, accessed 17 March 2017.

Dribus, J. R., et al, 2008, The prize beneath the salt, Oilfield Review, Autumn issue, 4-17.

Forrest, J., et al, 2005, Geothermal gradients and subsurface temperatures in the northern Gulf of Mexico, GCAGS Transactions, **55**, 233-248.

Fort, X. and Brun, J.P., 2012, Kinematics of regional salt flow in the northern Gulf of Mexico, in Salt Tectonics, Sediments and Prospectivity, Geological Society of London, Special Publication 363, 265-287.

Fredrich, J. T., et al, 2007, Mineralogy of deepwater Gulf of Mexico salt formations and implications for constitutive behavior, Journal of Petroleum Science and Engineering, **57**, Issue 3, 354-374.

Gorjian, M., et al, 2013, dynamic properties of anhydrites, marls, and salts of the Gachsaran evaporitic formation, Iran, Journal of Geophysics and Engineering, **10**, 1-10.

Green, S., et al, 2014, The importance of recognizing hydrodynamics for understanding reservoir volumetrics, field development and well placement, Presented at AAPG Annual Convention and Exhibition, adapted to Search and Discovery Article #41314, 1-19.

Jones, I. F. and Davison, I., 2014, Seismic imaging in and around salt bodies, Interpretation, November, SL1-SL20.

Hashin, Z. and Shtrikman, S., 1963, A variational approach to the elastic behavior of multiphase materials, J. Mech. Phys. Solids, **11**, 127-140.

Hunt, R. E., 2006, Geotechnical Investigation Methods: A Field Guide for Geotechnical Engineers, CRC Press, Table 1.9 Typical Compression-Wave Velocities in Soil and Rocks.

Hudec, M.R. and Jackson, M. P. A., 2011, The salt mine: a digital atlas of salt tectonics: The University of Texas at Austin, Bureau of Economic Geology, Udden book series No. 5, AAPG Memoir 99, 161-216.

Hudec, M. R., et al, 2013, Jurassic evolution of the Gulf of Mexico salt basin, AAPG Bulletin, **97**, no.10, 1683-1710.

Hunsdale, R., 2009, Abstract: Salt movement in the south-central Walker Ridge Area, Gulf of Mexico, Houston Geological Society Bulletin, **52**, no.4, 19.

Hyodo, M. and Takasugi, S., 1995, Evaluation of the curve-fitting method and the Horner-plot method for estimation of the true formation temperature using temperature recovery logging data, Proceedings, Twentieth Workshop on Geothermal Reservoir Engineering, 1-7.

Kantor, Y. and Bergman, D. J., 1984, Improved rigorous bounds on the effective elastic moduli of a composite material, J. Mech. Phys. Solids, **32**, no.1, 41-62.

Klimchouk, A., 1996, The dissolution and conversion of gypsum and anhydrite, International Journal of Speleology, **25**, no. 3-4, 21-36.

Martinez, J. M., 2014, Elastic properties of sedimentary rocks, PhD dissertation, University of Alberta, 168-173.

McBride, B.C., *et al*, 1998, The Evolution of Allochthonous Systems, Northern Green Canyon and Ewing Bank, Northern Gulf of Mexico, AAPG Bulletin, **82**, no. 5B, 1013-1036.

McDougall, D. J., 1952, Some factors influencing fluorescence in minerals, American Mineralogist, **37**, 427-437.

Milsch, H. and Priegnitz, M., 2012, Evolution of microstructure and elastic wave velocities in dehydrated gypsum samples, Geophysical Research Letters, **39**, L24305, 1-6.

Morcote, A., et al, 2010, Dynamic elastic properties of coal, Geophysics, **75**, no.6, E227-E234.

Murata, K. J. and Smith, R. L., 1946, Manganese and lead as coactivators of red fluorescence in halite, American Mineralogist, **31**, 527-538.

Ostroff, A.G., 1964, Conversion of gypsum to anhydrite in aqueous salt solutions, Geochemica et Cosmochimica Acta, **28**, Issue 9, 1363-1372.

Peters, K. E. and Nelson, P. H., 2009, Criteria to determine borehole formation temperatures for calibration of basin and petroleum system models, Presented at AAPG Annual Convention, published as Search and Discovery Article #40463.

Pindell. J. and Kennan, L., 2007, Rift models and the salt-cored marginal wedge in the northern Gulf of Mexico: implications for deepwater Paleogene Wilcox deposition and basinwide maturation, GSSEPM Transactions, 146-186.

Robertson, E. C., et al, 1958, Physical properties of salt, anhydrite, and gypsum, USGS Trace Elements Memorandum Report 1048, pp. 1-40.

Rolnick, L. S., 1954, The stability of gypsum and anhydrite in the geologic environment, PhD dissertation, Massachusetts Institute of Technology.

Rouchy, J. M., et al, 1995, Deepwater resedimentation of anhydrite and gypsum deposits in the Middle Miocene (Belayim Formation) of the Red Sea, Egypt, Sedimentology, **42**, issue 2, 267-282.

Rowan, M. G., 1995, Structural styles and evolution of allochthonous salt, Central Louisiana outer shelf and upper slope, AAPG Memoir 65 Salt Tectonics, 199-228.

Sams, M. S. and Williamson, P. R., 1994, Backus averaging, scattering and drift, Geophysical Prospecting, **42**, 514-564.

Schlumberger Oilfield Glossary, http://www.glossary.oilfield.slb.com/en/Terms/h/hydrostatic_pressure.aspx, and http://www.glossary.oilfield.slb.com/en/Terms/b/bottomhole pressure.aspx, accessed March 20, 2017

Schmitt, D. R., 2014, Geophysical properties of the near surface Earth: Seismic Properties, Treatise on Geophysics, **11,** Chapter 3**,** 52.

Sellier, N. and Vendeville, B. C., 2010, Gravitational Salt Tectonics Triggered by Deposition of Turbiditic Lobes: a New Experimental Modeling Approach with Applications to Salt

Tongues in the U.S. Gulf of Mexico, adapted from a Presentation at 2009 AAPG Annual Convention and Exhibition, 2010 Search and Discovery Article #40478.

Shaker, S., 2010, Dirty vs. clean salt: The impact on the subsalt Wilcox deepwater exploration plays, adapted from a Presentation at the AAPG Annual Convention and Exhibition, Search and Discovery Article #40565.

Takahashi, T. and Tanaka, S., 2009, Rock physics model for interpreting elastic properties of soft sedimentary rocks, Intl. J. of the Japanese Committee for Rock Mechanics, **4**, no.2, 53-59.

Walpole, L. J., 1966, On bounds for the overall elastic moduli of inhomogeneous systems - 1, Journal of Mechanics and Physics of Solids, **14**, 151-162.

Watt, J. P. and O'Connell, R. J., 1980, An experimental investigation of the Hashin-Shtrikman bounds on two-phase aggregate elastic properties, Physics of the Earth and Planetary Interiors, **21**, issue 4, 359-370.

www.bsee.gov/Technology-and-Research/Technology-Assessment-Programs/Reports/400-499/432AB/, accessed 5 June 2014.

Wyllie, M. R. J., et al, 1956, Elastic wave velocities in heterogeneous and porous media, Geophysics, **21**, no. 1, 41-70.

Yan, F., *et al*, 2014, Seismic velocities of halite salt: anisotropy, dispersion, temperature and stress effects, 84th Annual International Meeting, SEG, Expanded Abstracts, 2782-2287.

Zong, J., et al, 2016, Elastic properties of salt: Lab measurements and Gulf of Mexico well log analysis, www.agl.uh.edu/pdf/jingjing-elasticproperties.pdf, 1-46, accessed 2 Aug 2016, accepted for publication in Geophysics, 2017.

3 A regional geological 3D velocity model in the deepwater Gulf of Mexico

3.1 INTRODUCTION

The study area is located in the deep-water drilling province of the U.S. portion of the central Gulf of Mexico; and it primarily consists of Keathley Canyon, Walker Ridge and the southeastern corner of Green Canyon. The area was chosen for its current industry interest and the availability of both suitable seismic data and ample well logs with which to create a borehole database (see Figure 3.1).

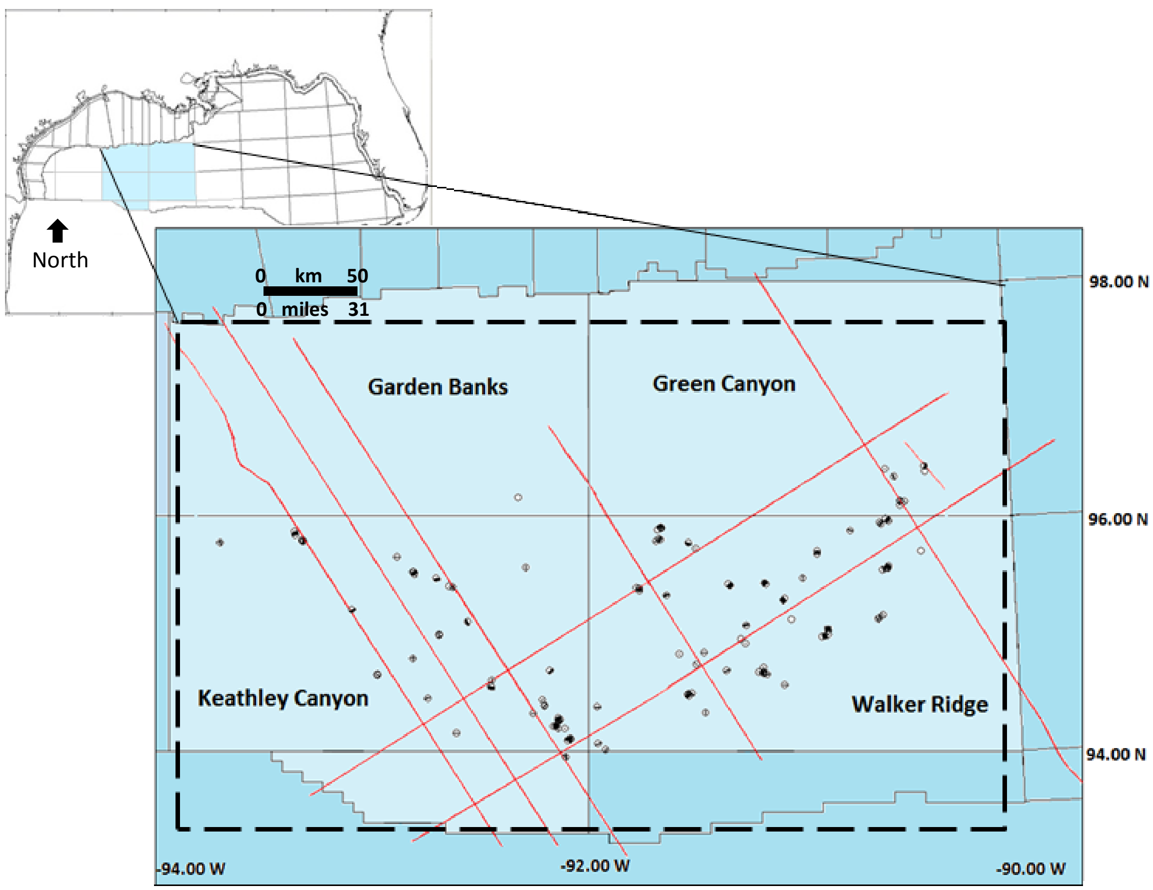

Figure 3.1. Study area basemap showing the corners of the 3D velocity model in map view outlined by the dashed black line.

There are serious issues in creating a velocity model for the deepwater part of the Gulf of Mexico: (1) the lack of well data in the upper portion of the sedimentary column, (2) how to accurately incorporate these pervasive salt-bodies with their odd shapes and rugose surfaces, and (3) how to incorporate the variability of the salt V_{int} into the velocity model. All of these issues are successfully addressed by the methodology selected to build the geologically-based 3D velocity model.

It is common for deepwater wells to not be logged with a sonic tool over the entire borehole, but only below salt, and sometimes only in the target zone. Salt interval velocities from Table 2.8 were used for the salt-body thickness portion of the borehole. To compensate for the lack of vital velocity information in the upper part of the borehole above salt, time versus depth charts were calculated using mudlogs to characterize lithology; and the gamma-ray (GR) and resistivity logs were used to help delineate fluid content. If measured log densities were available, then they were used directly in Gardner's equation (eq. (1), Gardner et al.

, 1974). If they were not available, then volume fractions of the sediment constituents (from the mudlogs) were used to calculate a composite (representative ρ) density from the clastic sections of Table 2.9 for the sediment and then this representative ρ was used in Gardner's equation to produce a compressional velocity ($V_{p)}$ for the specified lithological section in the borehole:

(1) $\rho = 0.23\ V_p\ ^{0.25}$, where V_p is in ft/s and ρ is the representative density of the section in g/cm^3. If V_p is in m/s, then equation (1) becomes equation (2):

(2) $\rho = 0.31\ V_p\ ^{0.25}$

Using the same technique for the lower part of the well in a few cases, where there were measured velocities, the calculated and measured velocities compared within 2%.

Sonic log data and cores were collected and analyzed from the sediments from just below the mudline down to 8,000 ft below mudline in wells located in Green Canyon for a study by Dutta et al., 2009. The objective was to study the compressional-wave velocity (V_p) versus depth (and the porosity versus depth) in these shallow sediments of the deepwater Gulf of Mexico. Figure 3.2 shows the results for both shales and sands. These values were used as guidelines in calculating the time versus depth charts in those instances where the mudlogs showed borehole sections to be all shale or all sand. Another source of information was (Sayers and Boer, 2011) work on the relationship between velocity and density in subsalt shales. Sometimes, the top of salt is quite deep and the shales above salt are at comparable depths to those shales studied subsalt elsewhere.

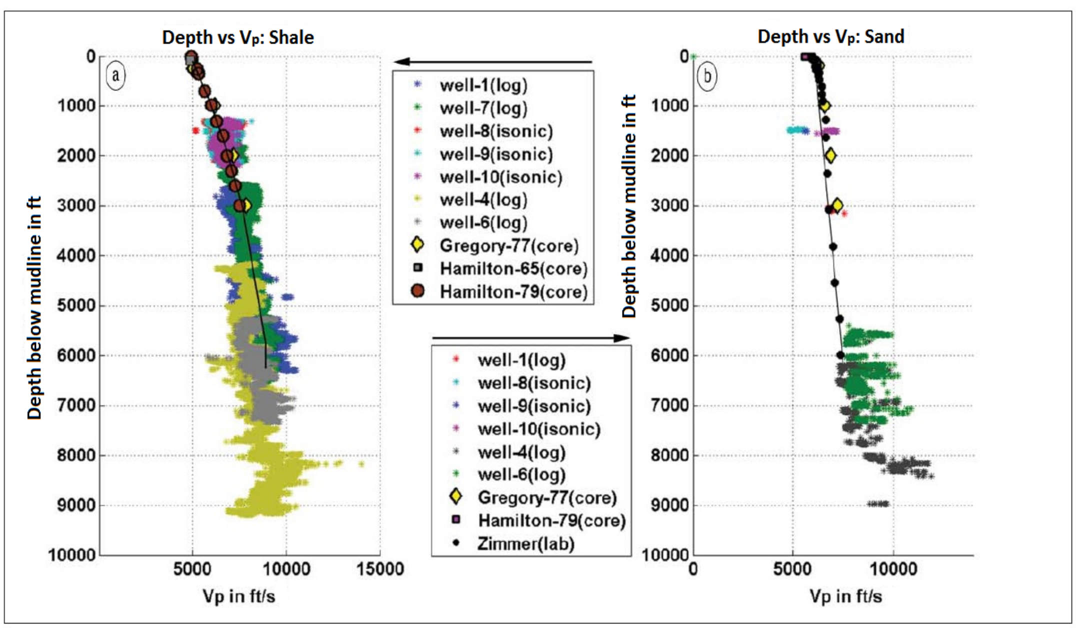

Figure 3.2. Depth below mudline (in ft) versus compressional-wave velocity V_p (in ft/s) trends in shale on the left and in clean brine sands on the right for shallow unconsolidated sediments. Measurements are from a combination of sonic logs and cores from shallow sections in the GoM (after Dutta et al., 2009).

Both seismic and well data were loaded into IHS Kingdom interpretation software application (version 9.0,) for data registration, and then exported in bulk to CGG's VelPro velocity modeling application. The VelPro application can facilitate the building of a velocity model without horizons (meaning it doesn't require 3D seismic data horizons or multiple well-based cross-sections) and accepts velocity information in a variety of formats, which can all be converted into interval velocities. Velocity models can be created in either acoustic-RMS velocities, in acoustic-average velocities, or in acoustic-interval velocities. Since this particular model was created to reprocess the seismic data used in its creation, the model was formatted in interval velocities, which has the additional benefit of conveying the stratigraphic and/or lithologic character of the subsurface geology. The workflow specific to this study is shown in Figure 3.3. The resultant 3D "cube" of interval velocities is easily exported for input into a seismic processing workflow after being trimmed to a usable portion.

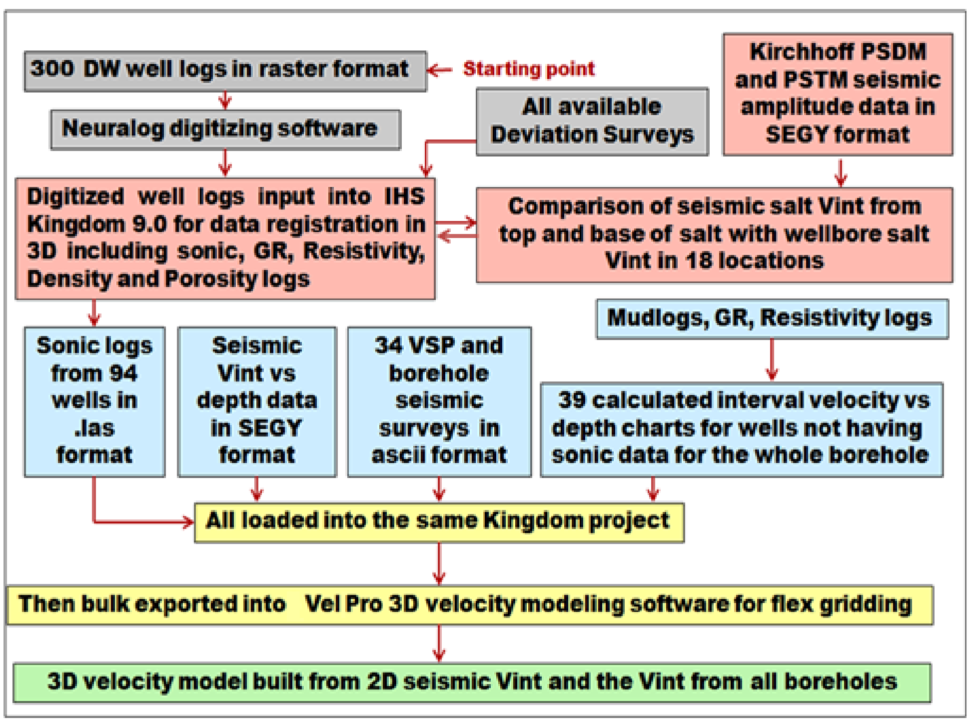

Figure 3.3. Workflow for creating a regional geological 3D velocity model with high resolution 2D seismic and extensive well data.

What is meant by a usable portion? The maximum effective area covered by the 3D velocity model is shown in Figure 3.4 and encompasses a surface area of approximately 60,000 km^2, which if I conservatively estimate that the velocity measurements are meaningful to a depth of 15 km, defines a volume that approaches 900,000 km^3. This is a truly regional model, but detailed comparisons show that it "looks" geologically reasonable and it faithfully honors the well control. Trimming to a 'usable portion' in my view eliminates areas of wide expanse that lack well control. If the objective were to reprocess just one of the 2D seismic lines, then it would be appropriate to reduce the area of the velocity model even further. There is significant variation in both the sediment and salt velocities from well to well, depending on the grain size of the sediments and presence of random sediment or mineral inclusions inside the salt, as outlined in Chapter 2, and will be documented later by illustrations from within the velocity model itself.

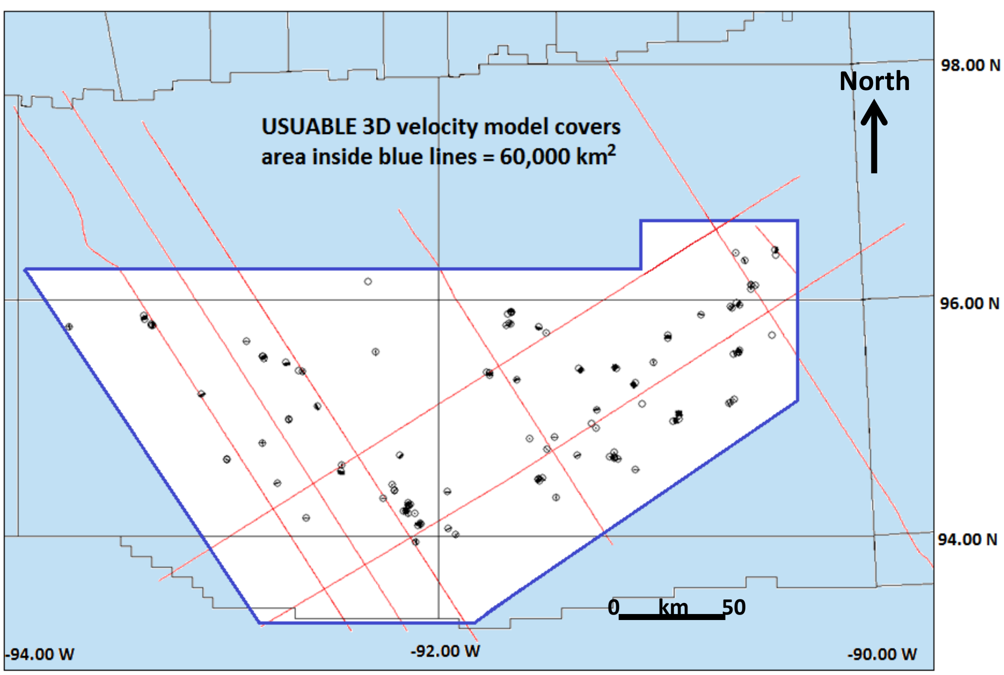

Figure 3.4. The usable portion of the velocity model for reprocessing the 2D seismic data.

3.2 WELL LOG DATABASE

Well data were acquired from the www.bsee.gov website over a 27 month period (from March, 2014 to June, 2016); and since the log curves came in a raster format, the data were digitized by hand using Neuralog software for input into the IHS Kingdom 9.0 application. This time-consuming process to digitize 265 well logs took 16 months due to the extreme depth of the boreholes and to the number of tracks per well log. Within the defined study area, all available GR, resistivity, sonic, porosity, and density logs, plus all mudlogs and deviation surveys, were acquired. Most importantly, all velocity surveys, whether VSP, walkaway seismic, or borehole seismic while drilling (SWD), were acquired. All available paleontological reports for these wells were purchased to permit the correlation of time lines through lithostratigraphically defined formations to serve as confirmation for ordinary well log correlation picks (tops). Well plans and final well reports were also included in the database where available.

The well data were input into IHS Kingdom, correctly registered in 3D space using all the available borehole deviation surveys, and utilized both the surface and bottom-hole locations where deviation surveys were not available. It was the original intention to create two velocity models using two different software packages with the same data to allow comparison of the results of each model so as to recognize software-specific artifacts, biases, or errors. An attempt was made to build such a model using Petrel software; but it was unsuccessful due to lack of horizons for input, as Petrel requires a layer-based model. The distribution of the four types of sonic velocity measurement is shown in Figure 3.5. The different types are more or less evenly distributed throughout the study area.

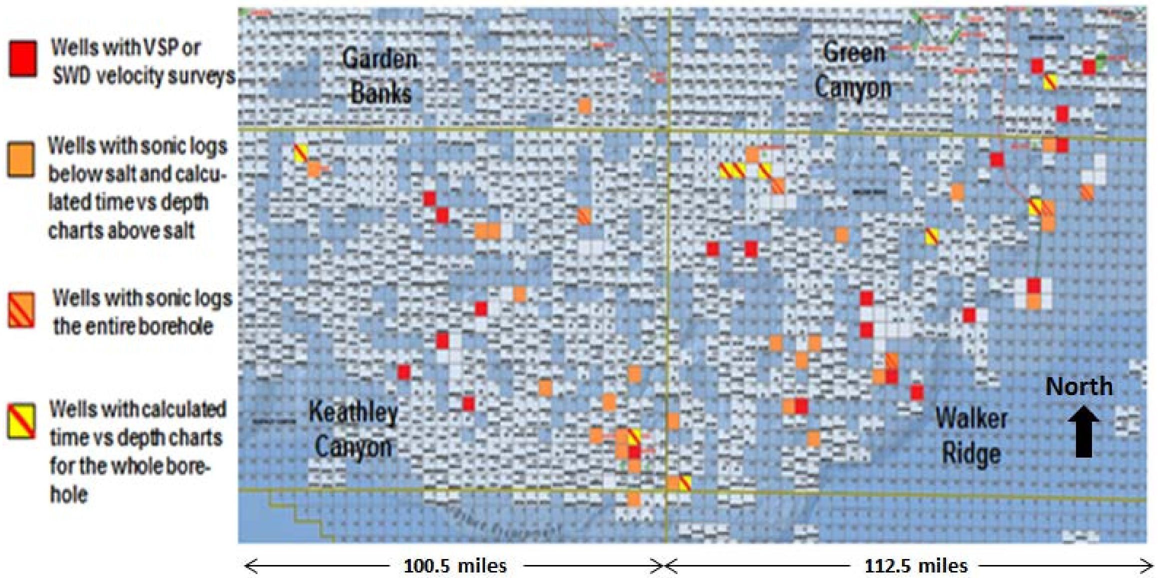

Figure 3.5. Distribution of the four types of sonic velocity measurement utilized in this study. Each lease block is 3 miles on each side, so both the horizontal and vertical scale can be determined by the number of blocks being observed.

3.3 SEISMIC DATA USED

It was not possible to obtain one or more deepwater Gulf of Mexico 3D seismic data sets of recent vintage with the requisite long offsets for use in this study. Most of these expensive seismic data sets are multi-client surveys and it is extremely difficult to obtain permission from all participants to permit academic use of the data. However, a remarkably high-resolution 2D survey shot in 2011-2012 with 15 km offsets was made available by Dynamic Data Services (DDS). This seismic survey was processed assuming a constant interval velocity (V_{int}) for salt of 4.5 km/sec (and without any well control) using Kirchhoff migrations for PSTM and PSDM. The airgun source (twice the normal volume), was towed 60 ft below sea level, and the very long stream (15 km maximum offsets) produced excellent quality data.

3.3.1 Comparison of surface-seismic salt V_{int} with borehole-measured salt V_{int}

The close agreement between the seismic-imaging velocities (derived from stacking velocities) and the velocity values from the well data are displayed in Table 3.1 (which is the same as Table 2.2). There are 18 wells in close proximity to the seismic lines and in 10 of them, the measured borehole salt V_{int} matches the seismic salt V_{int} within 2% or less. Five wells match within 4.8%, two wells show ≈6% difference and the one outlier well has a 15.43 % difference. In Chapter 2, it was shown that the reason for the differences greater than 2% is that these wells include either anhydrite, gypsum, or sylvite mineralogies within what would generally be classified as halite (rock salt). Analysis of the mudlogs documents that the presence of these other evaporite minerals correlates with variations in some of these borehole V_{int} measurements. The salt in the last borehole in the table, WR-627-001, is pure halite according to its mudlog; in this case it is believed that the high value of its seismic salt V_{int} is due in part to poor projection of the strongly deviated borehole onto the seismic line.

For these comparisons of surface-seismic V_{int} to all forms of borehole-measured V_{int}, the salt V_{int} was measured at each location where the nearby well was most closely projected into the seismic line by measuring the top and base of salt on the Kirchhoff PSTM to produce a ΔT (time) and then measuring the top and base of salt in the corresponding well to produce a ΔD (depth). Dividing ΔD by ΔT gives the salt V_{int} for that well location.

Well name	API- UVI	Seismic top of salt (sec) TWT	Well top salt (ft) SRD	Seismic base of salt (sec) TWT	Well base salt (ft) SRD	Seismic salt V_{int} (ft/s)	Seismic salt V_{int} (m/s)	Well salt V_{int} (ft/s)	Well salt V_{int} (m/s)	% Difference
Green Canyon area										
GC-821-001	608114044800	1.7709	5024	3.3502	16052	**13966**	**4257**	**14669**	**4471**	**4.79**
GC 955-001	608114027100	4.2770	13136	4.3055	13341	**14362**	**4378**	**14582**	**4445**	**1.51**
GC-955-002	608114047700	4.9628	16238	5.3296	19113	**15675**	**4778**	**18535**	**5650**	**15.43**
Keathley Canyon area										
KC-57-001-ST1	608084004101	3.0740	7934	5.5090	26264	**15055**	**4589**	**14751**	**4496**	**-2.06**
KC 102-001	608084001500	3.1090	8410	5.3220	24905	**14907**	**4544**	**14475**	**4412**	**-2.98**
KC-292-001-ST2	608084001104	3.8123	10225	5.7797	24564	**14577**	**4443**	**14586**	**4446**	**0.06**
KC-292-001-BP1	608084001101	3.8123	10225	5.7797	24564	**14577**	**4443**	**14925**	**4549**	**2.33**
KC-292-002	608084001102	3.8134	10229	5.7742	24539	**14596**	**4449**	**14586**	**4446**	**-0.07**
KC-470-001	608054001900	4.8980	14695	5.9770	22795	**15014**	**4576**	**15107**	**4605**	**0.62**
KC-470-001	608054001900	5.9600	23275	6.0452	23875	**14085**	**4293**	**14292**	**4356**	**1.45**
KC-736-001	608084002200	3.0984	7808	5.0172	21608	**14384**	**4384**	**14384**	**4384**	**0.00**
KC-872-001	608084001600	3.2622	8216	4.7376	19306	**15033**	**4582**	**14850**	**4526**	**-1.23**
Sigsbee Escarpment area										
SE-39-001-BP2	608094000102	4.4400	9607	4.7547	12236	**16707**	**5092**	**15634**	**4765**	**-6.86**
Walker Ridge area										
WR-143-003	608124008900	4.0370	11383	5.8630	25128	**15054**	**4589**	**14493**	**4418**	**-3.87**
WR-316-001	608124003700	2.7380	6858	5.4830	25946	**13989**	**4264**	**14617**	**4455**	**4.30**
WR-543-001-BP	608124004501	3.7580	9614	5.8340	24602	**14439**	**4401**	**14706**	**4482**	**1.82**
WR-544-001	608124002100	3.6676	9816	5.5061	23510	**14897**	**4541**	**14893**	**4539**	**-0.03**
WR-627-001	608124002400	3.7876	10585	5.2174	21748	**15615**	**4760**	**14731**	**4490**	**-6.00**
standard deviation		0.9192	4011	0.7032	4315	**663.6**	**311.3**	**202.3**	**94.9**	**3.22**
mean value		3.7933	10738	5.3103	21894	**14780**	**4505**	**14722**	**4487**	**-0.37**

Table 3.1. Seismic salt V_{int} compared to measured-borehole salt V_{int} and the percent differences. A positive percent difference means the borehole velocity is faster. The green color for well-salt V_{int} indicates these are borehole seismic velocity measurements, while no color indicates sonic log measurements. The outlier well (GC-955-002) was excluded in the calculations for standard deviation and mean value.

3.3.2 Seismic data image quality

Three examples of the seismic data for strike line 2800 are displayed in Figure 3.6 in the following formats: Figure 3.6a, Kirchhoff PSDM for a subset of line 2800; Figure 3.6b, an average energy display of the same Kirchhoff PSDM subset of line 2800, and Figure 3.6c, a display of seismic V_{int} (the velocities used in processing the seismic data) versus depth. In Figure 3.6c, the V_{int} ranges from 5000 to 22000 ft/s (1524 to 6706 m/s) and the depth range is from 0 to 70,000 ft (0 to 21,336 m). Line 2800 is a strike line starting in the southwestern part of the map and running to the northeastern edge of the study area. Note that this line crosses the Sigsbee

Escarpment twice as shown with the full line in Figure 3.8.   Figure 3.7 illustrates a dip line in the same format as 3.6c. All of the seismic velocity data were loaded into the VelPro application in this same format of V_{int} versus depth, so it was possible to add the well control (in the same format); and then grid both seismic and well data together to create a 3D velocity volume (i.e., a 3D velocity model).

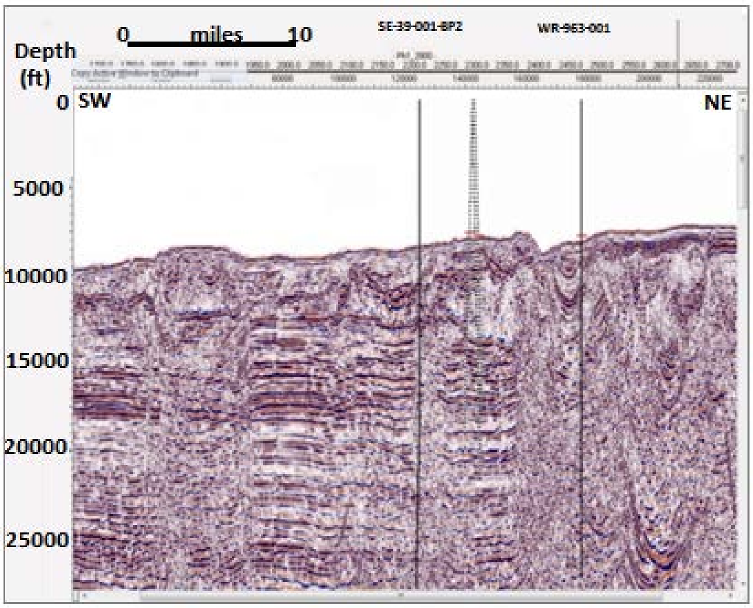

Figure 3.6a. Kirchhoff PSDM for a subset of strike line 2800.

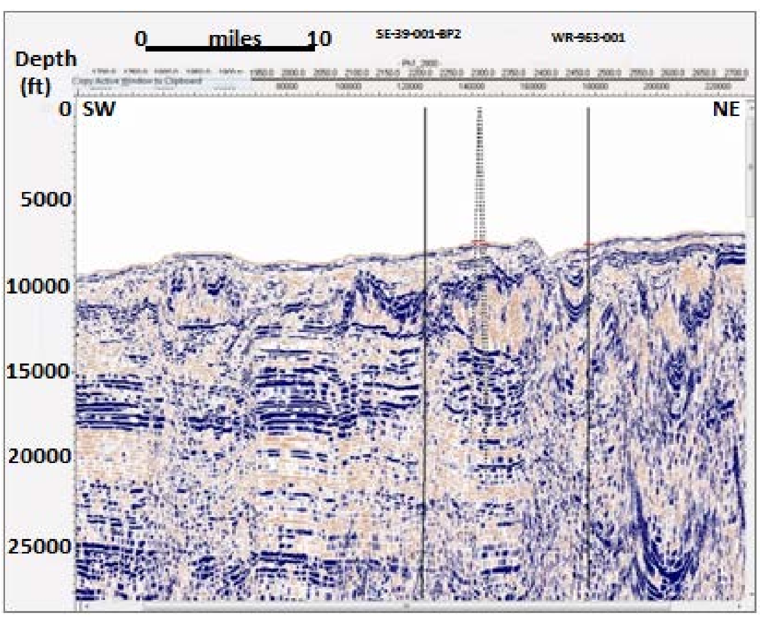

Figure 3.6b. An average energy display of the same Kirchhoff PSDM subset of strike line 2800.

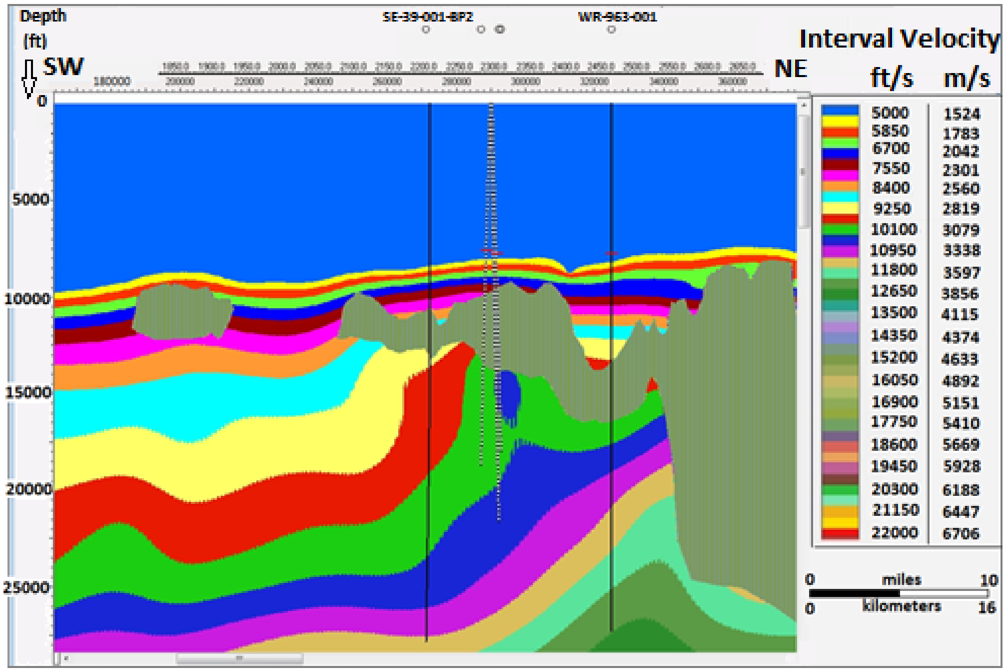

Figure 3.6c. Same section of line 2800 displayed as the seismic processing velocities vs. the same depth scale as that in Figures 3.6a and 3.6b. All three images were captured between the same shotpoints; and so they have the same vertical and horizontal scale.

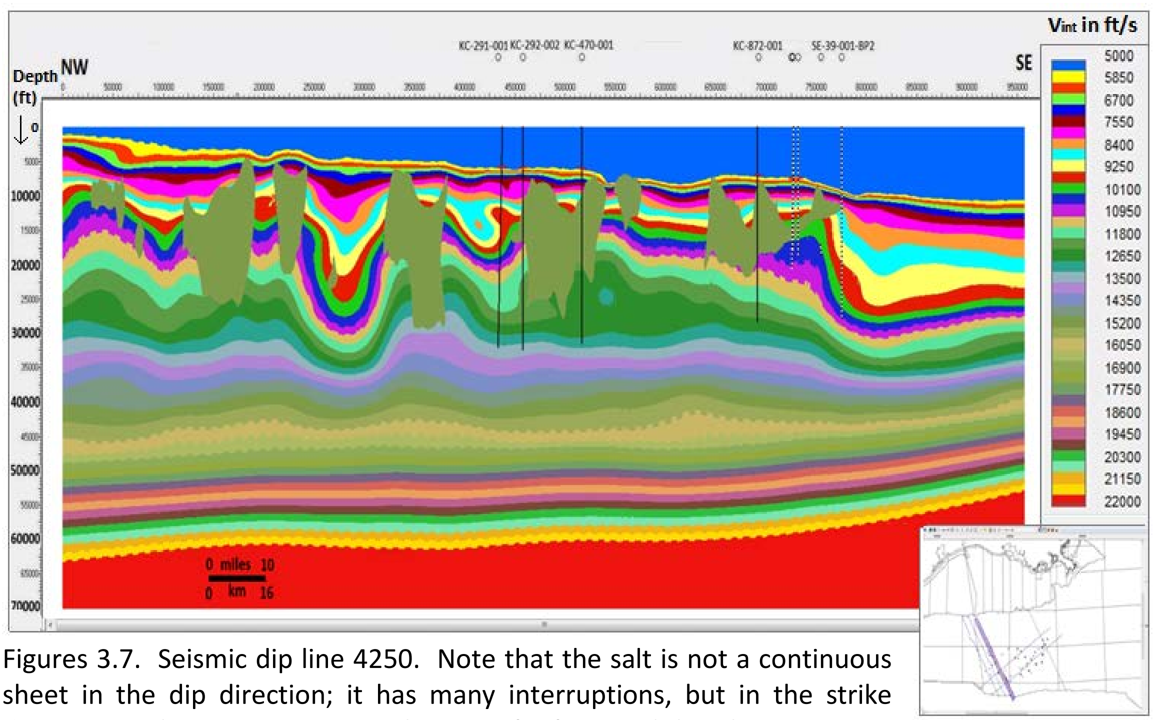

Figures 3.7. Seismic dip line 4250. Note that the salt is not a continuous sheet in the dip direction; it has many interruptions, but in the strike direction as shown in Figure 3.8, there are far fewer salt breaks.

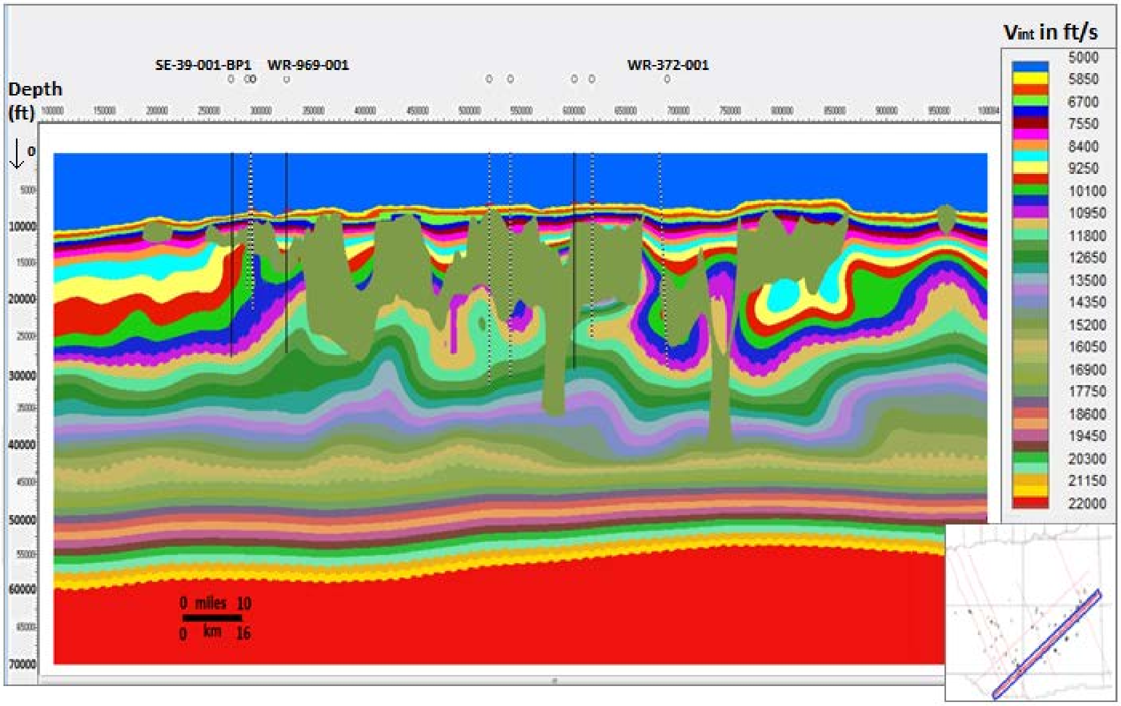

Figure 3.8. Seismic strike line 2800. This is the entirety of the line that was shown only by a small segment in Figures 3.6a-c. The vertical extent is 0 to 70,000 ft on the depth axis and the interval velocity scale is the same as displayed in Figure 3.6c.

3.3.3 Bathymetry data

Topex bathymetry data (Sandwell and Smith, 2009) was part of the culture data imported into this VelPro project and it is displayed in Figure 3.9. Originally, it was planned to incorporate the bathymetry data as a water bottom layer into the velocity model; but experimentation showed that differences between the gridded seismically-defined water-bottom horizon and the Topex-defined bathymetry data caused undesirable artifacts and so the velocity models were gridded without a bathymetric constraint.

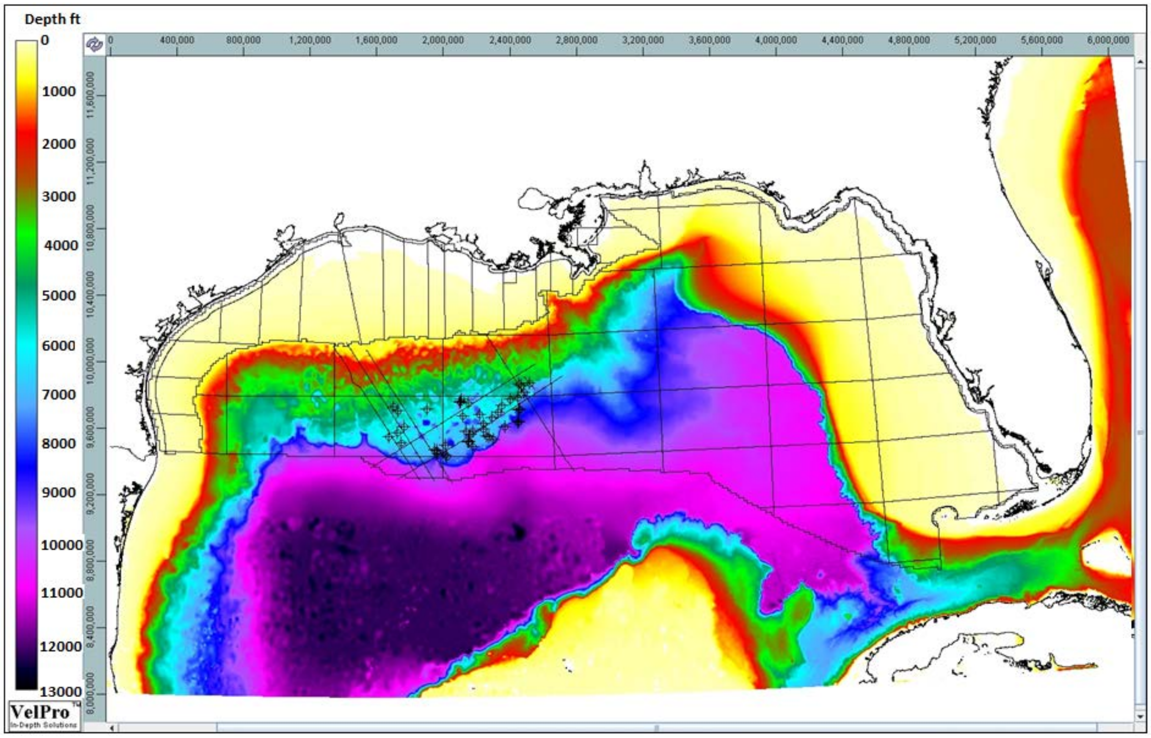

Figure 3.9. Regional Gulf of Mexico bathymetry map for the seafloor. The map has a depth range from 0 to 13,000 feet and is from Topex. Study area shows well and seismic data locations. Coordinates are in X,Y feet.

3.4 THE IMPORTANCE OF USING MUDLOG DATA

Mudlogs are an under-utilized resource in building velocity models, partly due to the unfamiliarity with these well logs by many geophysicists. The deepwater GoM has a very complex distribution of lithologies even though it is dominated by sand and shale sequences. The variety of grain sizes and specific mineralogies is considerable, and consequently, so are the velocities, and these are accurately reflected in the logged sonic velocity measurements where they are available. Subtle changes, and in some cases very large contrasts, in sonic measurements are often overlooked or ignored by geophysicists who may use log smoothing techniques to eliminate these anomalies. If the sonic log or checkshot values do not appear to make sense, it is appropriate to look at the mudlog to determine the lithology and whether or not this lithology should yield the sonic values recorded at a specific depth. Mudlogs were used in this model to generate "synthetic" or calculated time vs depth charts to fill in what would have been large gaps in the velocity control for the 3D model, both in salt and above the salt. Only 27 of the 88 wells (not counting bypasses or sidetracks) used in this study had complete borehole coverage from sonic data; but with the addition of wells with mudlog control, the number of wells for "complete" (top to bottom) velocity control was raised from 27 to 65.

3.5 THE 3D VELOCITY MODEL

Experimentation with various gridding parameters led to the selection of flex gridding with minimum tension and minimum smoothing. The IHS Kingdom 40-random color bar was selected to show the geological detail in the iso-velocity layers. The 3D velocity model was exported as a 3D seg-y file from VelPro and imported into IHS Kingdom where it was inspected in the VuPak module for 3D visualization. Animation files were created showing the 3D visualization moving from south to north (displaying a strike orientation), from west to east (displaying a dip orientation), and from the top to the bottom (map view). A view of the entire 3D velocity model from the southwest corner toward the northeast corner is shown in Figure 3.10. This is a still image captured from an animated video and other still images will be shown within this section. The color bar can be rotated to show special features in contrast to a muted background. In Figure 3.11, seismic dip line 3850 is spliced into the velocity model. The juncture is seamless except that the model has more detail in the salt. The velocity model honors all data points; and if there is a conflict, preference is given to well data.

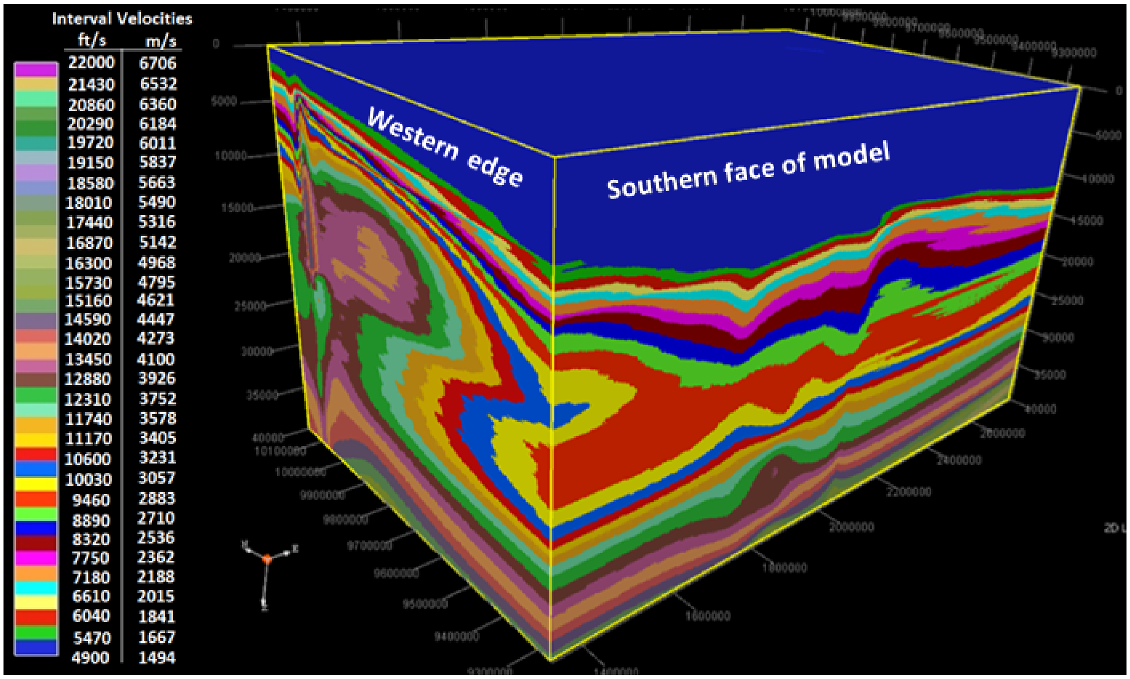

Figure 3.10. Image of 3D velocity model viewed from SW to NE with the 40-random color bar displayed to the left. Water velocity starts at 4900 ft/s (1494 m/s) and the sediment velocities range upwards to 22,000 ft/s (6706 m/s). Note that here the velocity scale is reversed with low numbers at the bottom. Vertical depth range is from 0 to 40,000 ft.

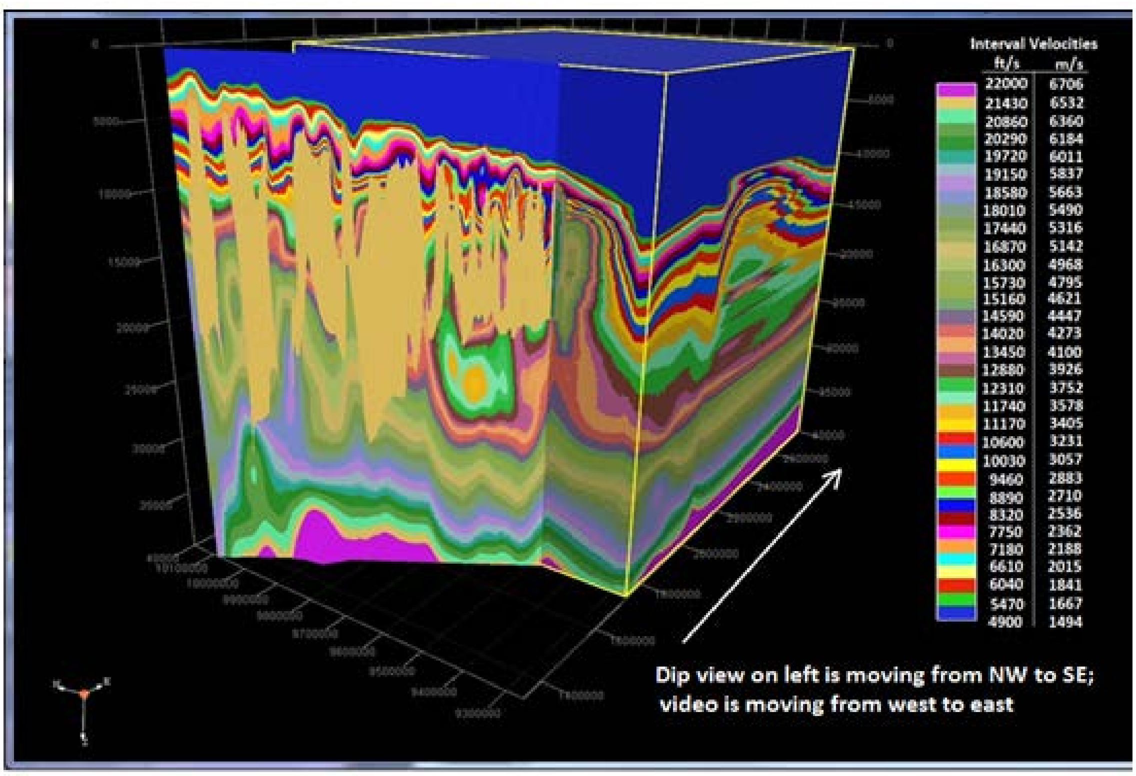

Figure 3.11. Seismic dip line 3850 spliced into the 3D velocity model

Figure 3.12 illustrates a horizontal slice at 7,500 ft (2286 m) below sea level. This video animates from top to bottom, slicing the model horizontally while displaying the model in plan view. At this depth most of Keathley Canyon is represented by sediments while most of Walker Ridge is still in water. About half of Garden Banks and the southern part of Green Canyon are already within salt. Even though the velocity model layers look stratigraphic, they represent layers of equal interval velocity and not lithology. Nevertheless, they do represent the gross architecture of the geological subsurface. Some of the strong dips shown in this image may relate to faults in the subsurface instigated either by salt movement or sediment loading over time.

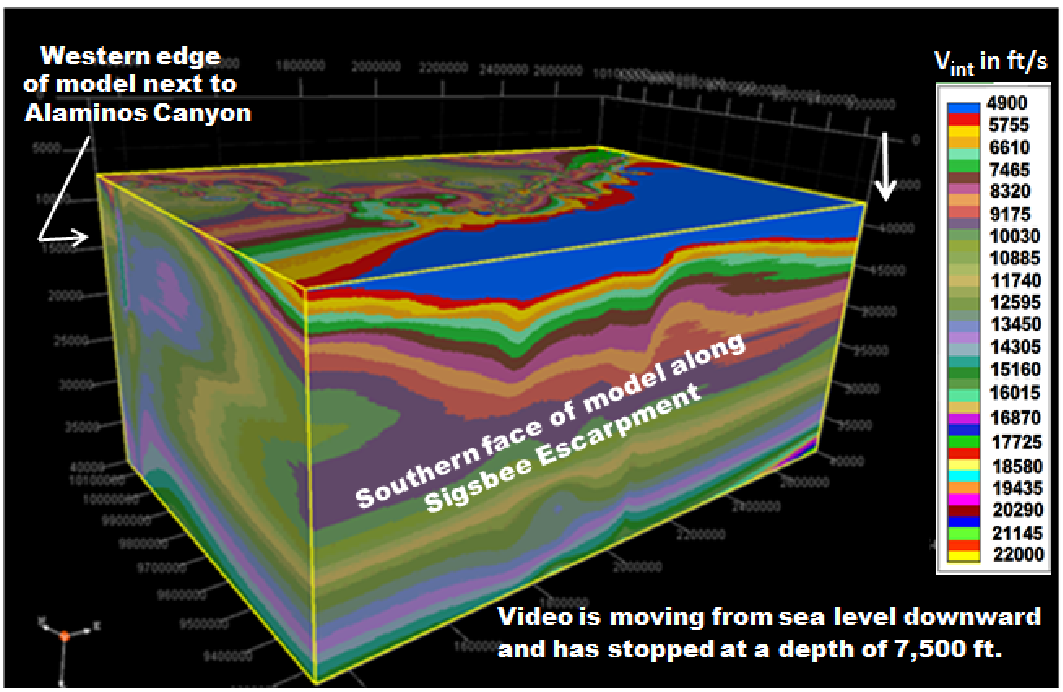

Figure 3.12. A horizontal depth slice within the velocity model shown at 7500 ft (2286 m) below sea level.

Figures 3.13a and 3.13b illustrate east-west slices through the model showing where salt has intruded into the sedimentary sections. The geographical position of the profile shown in Figure 13a is more northerly than the one shown in Figure 13b; and in it the sediments enclosed in the white oval have not yet been penetrated by salt. Slightly to the south, Figure 13b shows the salt has begun moving eastward, and is seen to cut the sediment column in half. This observation **appears** to contradict current thought which assumes that the Louann Salt is moving south to southwesterly towards the deepest part of the basin (discussed in section 2.4.2, Fort and Brun, 2012). Perhaps this observation represents a localized occurrence that is not representative of regional trends.

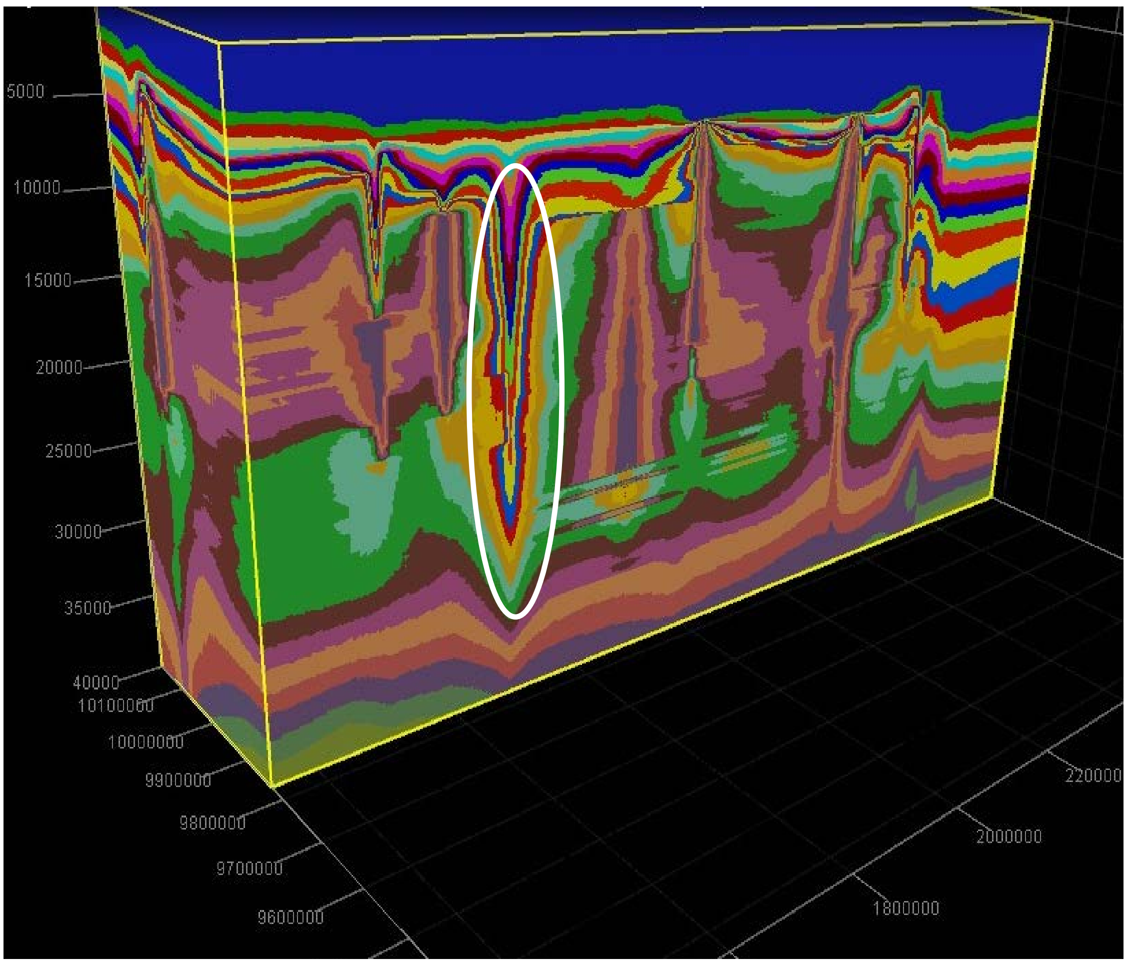

Figure 313a. Inside white oval, sediment column is undisturbed. Vertical axis is depth in feet and latitude and longitude are given by X,Y coordinates in feet.

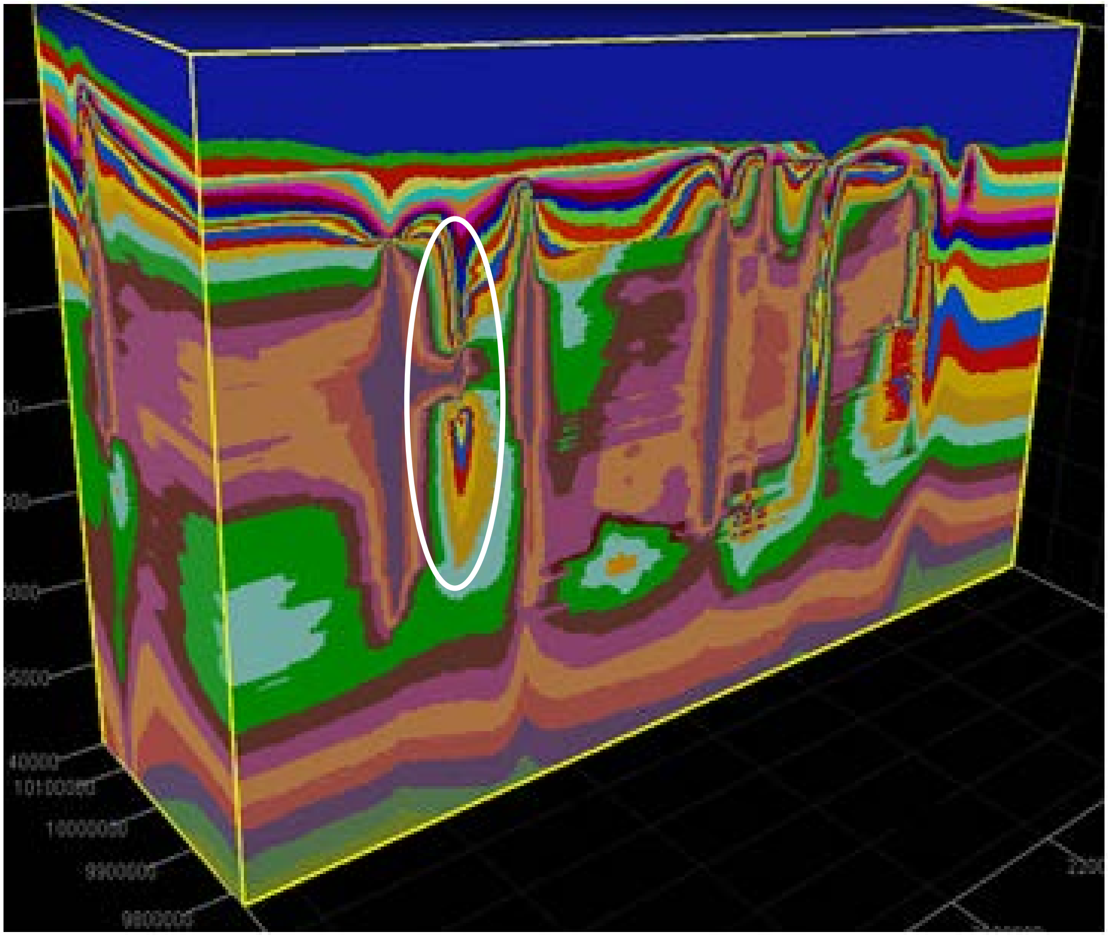

Figure 3.13b. Image is slightly to the south of Figure 3.13a and here the sediment column has been penetrated by salt from the west.

ZONES OF OVERPRESSURE EXHIBITED WITHIN THE 3D VELOCITY MODEL

Figure 3.14a shows an overpressure zone below salt in the northern central part of Walker Ridge. The overpressure is recognized by the very low-interval velocities beneath a high-velocity salt overhang and this relationship is shown by the white oval. Moving slightly to the east, in Figure 3.14b, the overpressure noticeably increases both in area and intensity, spreading into Green Canyon.

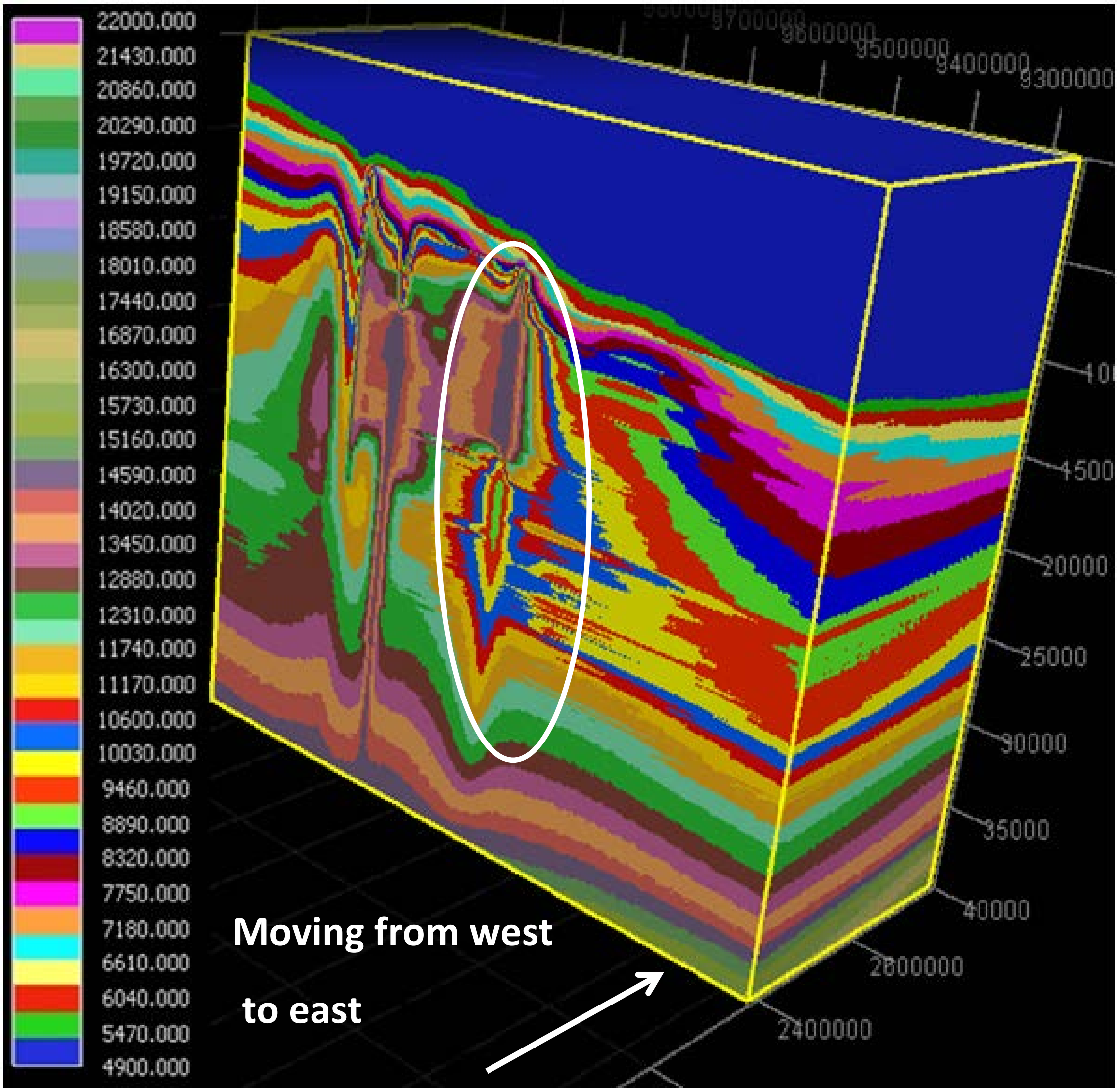

Figure 3.14a. A major overpressure zone in the northern central part of Walker Ridge that is below salt. To the left of the overpressure zone, another one is forming, just not as intense. V_{int} are given in the color bar on the left in ft/s.

Figure 3.15a shows a very large overpressured zone on the western side of Keathley Canyon, mid-way between the northern and southern boundaries of the model. As the animation of the model moves from south to north, the overpressure zone diminishes in size but its intensity increases. Figure 3.15b shows the areal extent of the overpressure increases but its areal extent

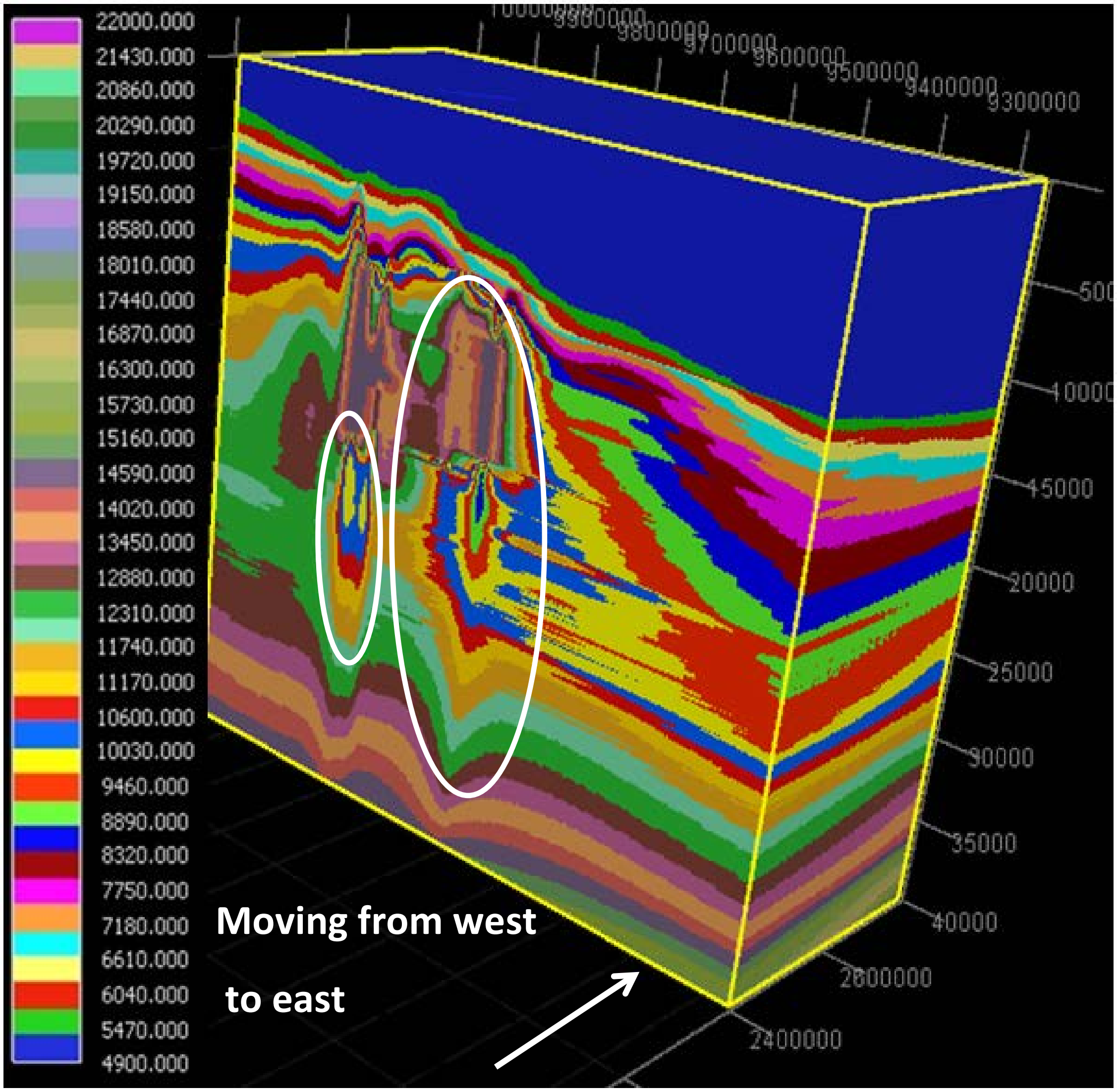

Figure 3.14b. Slightly to the east of Figure 3.14a, there are now two large overpressure zones, more or less of the same intensity. Note that the zone on the left is also below salt. V_{int} are given in the color bar on the left in ft/s.

decreases and Figure 3.15b. is south of the image in Figure 3.15a. Note that in contrast, the similarly-colored-velocity values to the right in Walker Ridge are not an overpressure zone because in that location the increases in velocity with depth are sequential, i.e., there is no inversion of velocity.

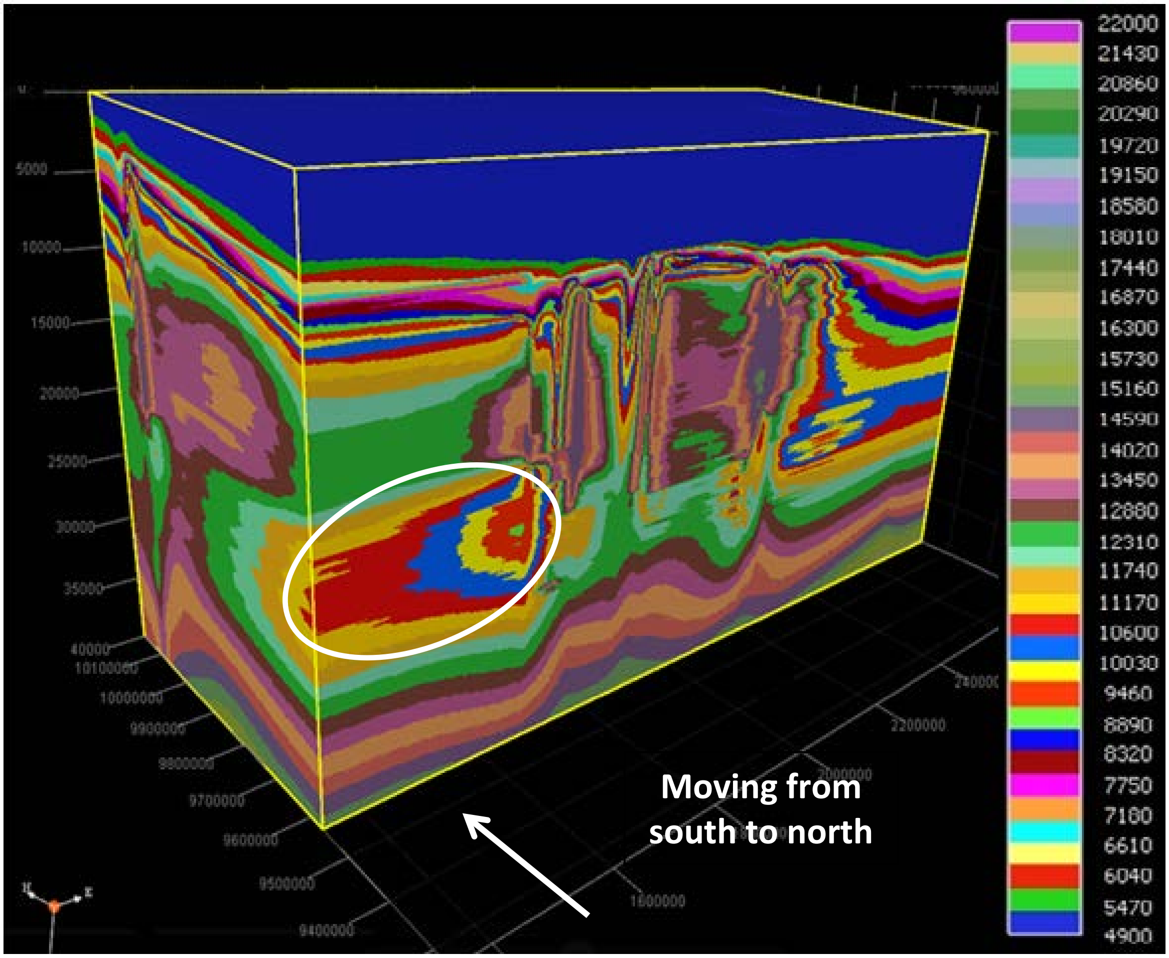

Figure 3.15a. An overpressure zone with large areal extent, only partially underneath salt.

3.6 OTHER FEATURES OF THE VELOCITY MODEL

Because of the rich details in the velocity distribution that are provided by well control, the model can fill in gaps between arbitrary lines, illustrate gradients in salt velocities where appropriate, document the presence of higher-velocity minerals or lower velocity sediments within the salt, and also call our attention to the presence of Cenozoic limestone where its volume fraction is > 60% and where it covers at least 1000 vertical ft (305 m) of borehole.

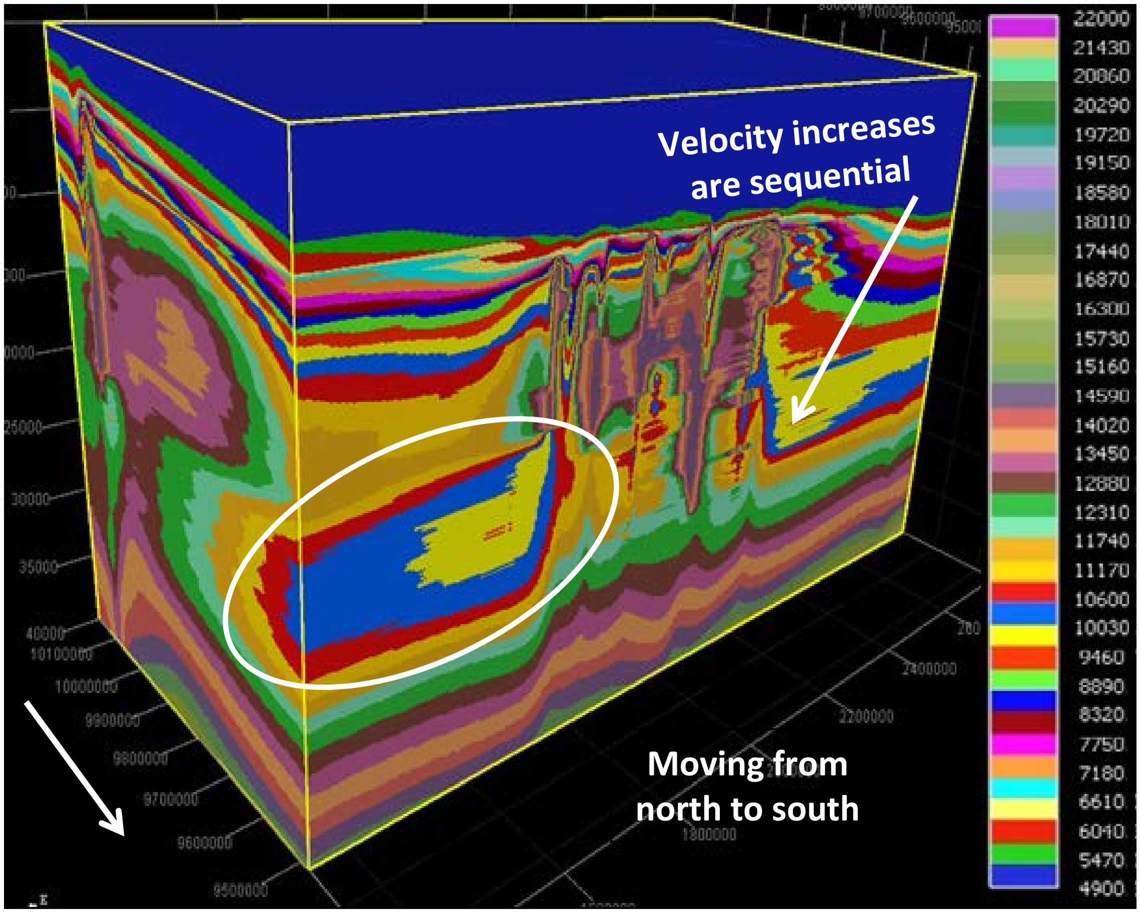

Figure 3.15b. The same overpressure zone further south. It has lost intensity but gained in areal extent. Note that in eastern section of Walker Ridge (to the right) is a similarly colored zone; however, the velocity increases in this case are sequential and so the zone is normally pressured.

3.6.1 Case A: Filling in missing gaps

Figure 3.16a shows interval velocity displays for three seismic line segments in the southwestern corner of Green Canyon. Figure 3.16b is an arbitrary line connecting those same segments extracted from the velocity model. Comparison of the two shows that the velocity model has seamlessly filled in the gaps of velocity information between the segments of seismic velocity control.

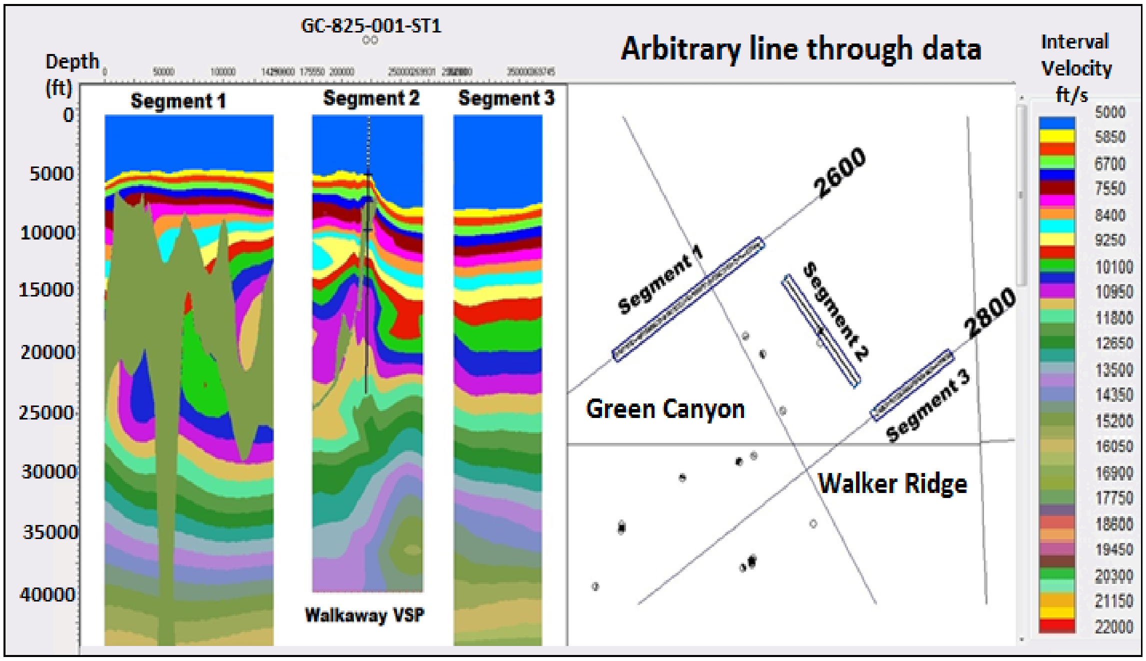

Figure 3.16a. Seismic segment 1 is from strike line 2600. Segment 2 is from the walkaway VSP associated with the GC-825-001-ST1 well. Seismic segment 3 is from strike line 2800.

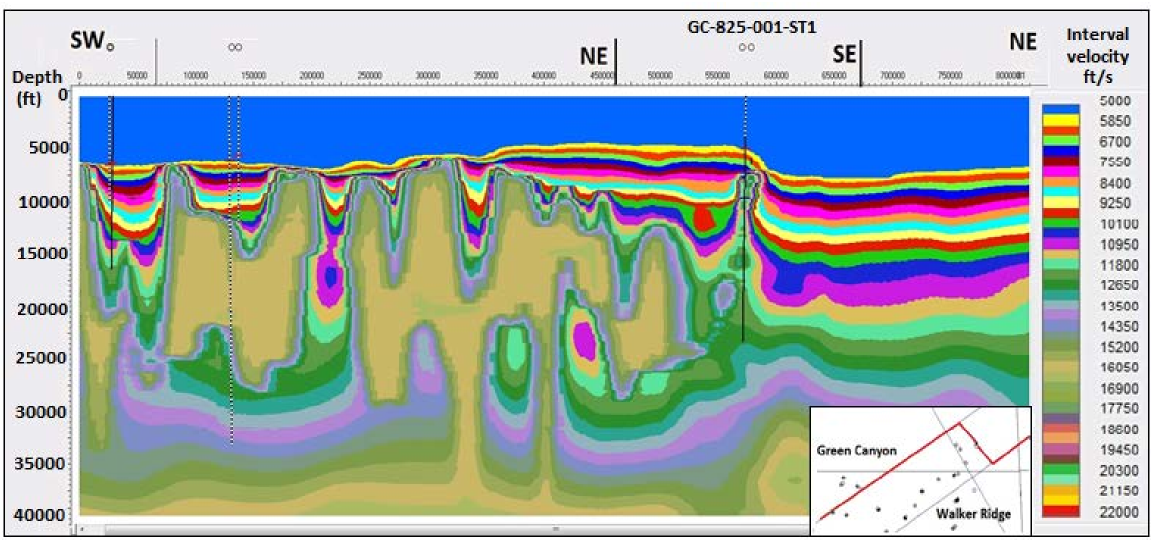

Figure 3.16b. An arbitrary line taken along the same pathway as in Figure 3.16a within the velocity model.

3.6.2. Case B: Showing anomalously high-velocity evaporites or low-velocity sediments within the salt

If the volume fractions of anomalously high-velocity evaporites (gypsum and anhydrite) are sufficient such that the salt V_{int} is noticeably different than that of pure halite, it is possible for them to be detected within the velocity model. The larger the areal extent of such minerals, the more "visible" they become sonically. For example, Figure 3.17a shows an arbitrary line through seven wells in southeastern Keathley Canyon within the model with V_{int} values from the 3D velocity model displayed in VuPak. In this illustration, an anomalously high-velocity component of the salt, shown in a dark purple color (see circle) is known to coincide with the mineral gypsum in the wellbore. This was confirmed by the mudlogs of each well. The same arbitrary line displayed within VelPro is shown in Figure 3.17b. VelPro does not have the same 3D visualization capabilities as VuPak, but it does have the advantage of being able to show each well's interval velocity profile. The "blocky" color displays within the borehole are keyed to the same colorbar as the seismic-interval velocities. Figure 3.17b also confirms the presence of gypsum on a well-by-well basis. Note the difference in the colorbars used in the different software modules.

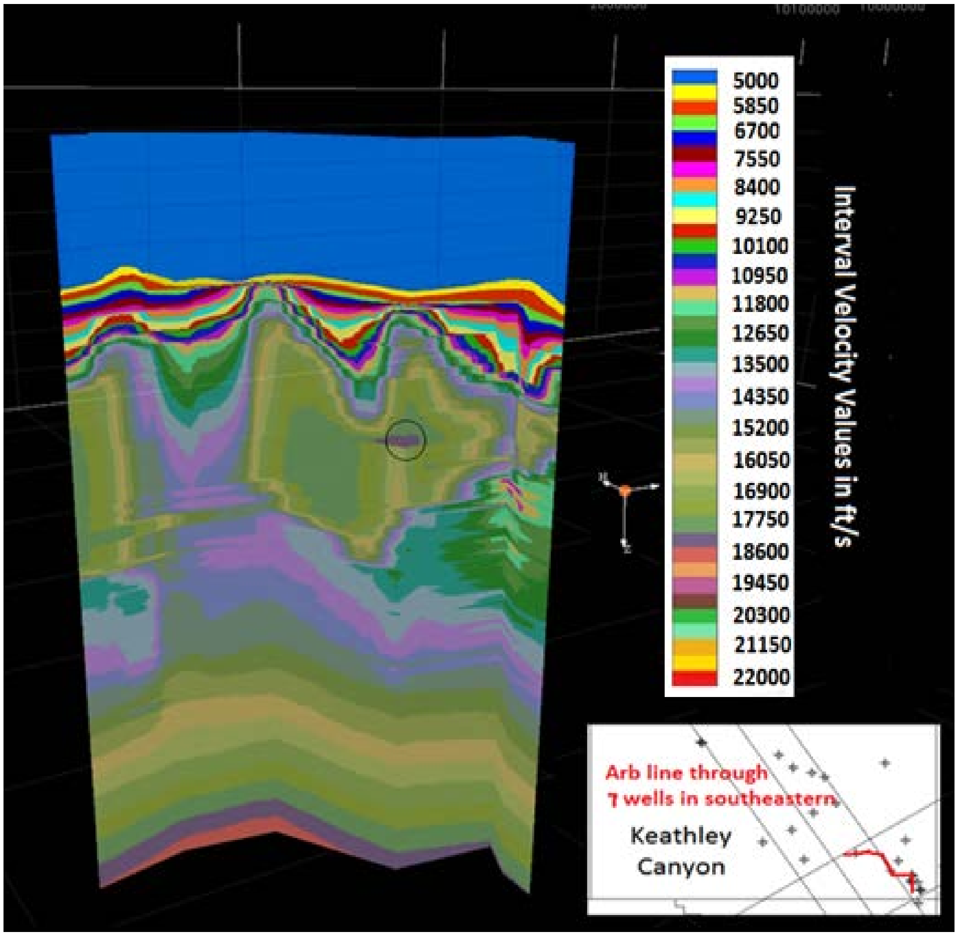

Figure 3.17a. Arbitrary line inside model drawn through 7 wells in southeastern Keathley Canyon showing presence of a high-velocity mineral within the salt (inside black circle).

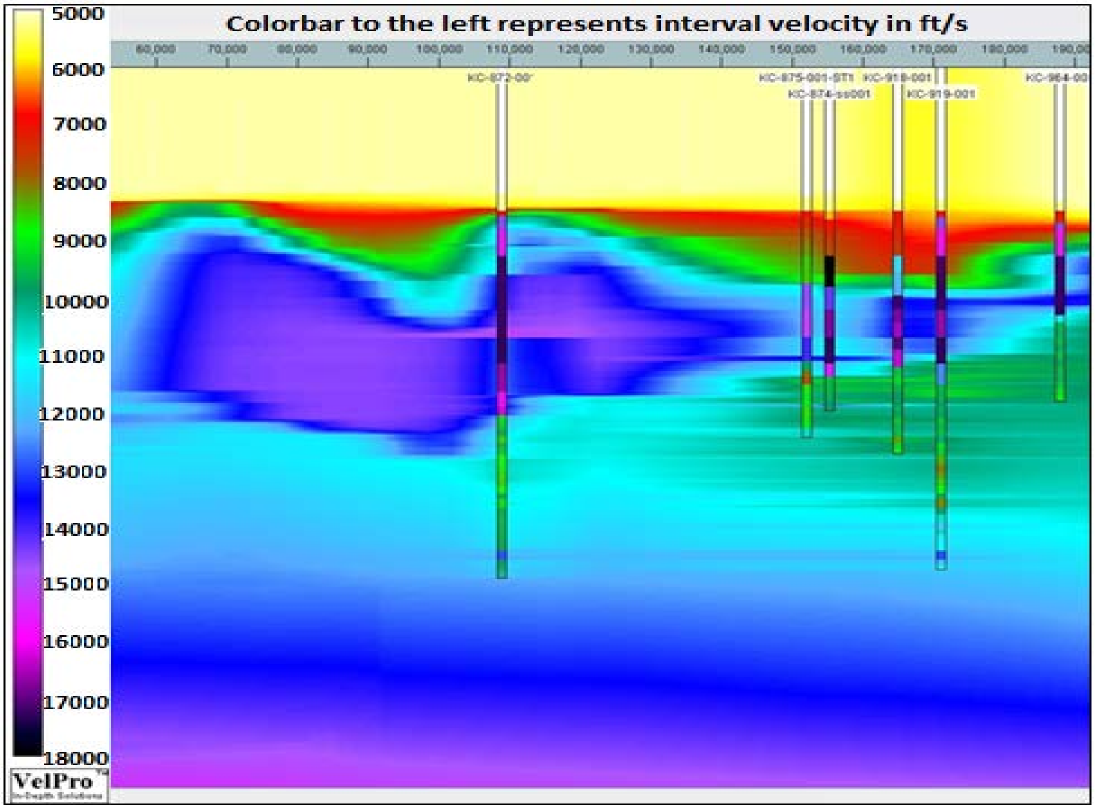

Figure 3.17b. Same arbitrary line within model as in Figure 3.17a but displayed in VelPro. The individual wells show the presence of high velocities that the mudlogs show to be gypsum. The ties between the wellbore and seismic velocities are not perfect but the trends are faithfully honored.

Figure 3.18 shows two lower-velocity sediment inclusions (or the mineral sylvite) appearing in the upper salt body with a reddish color and two higher- velocity mineral components, one in the upper salt body and one close to the base of salt appearing in a greenish color, as seen inside the white circles. The well closest to these anomalies is WR-848-001-BP1, which has a mudlog that documents the presence of gypsum around 10,850 ft (close to the top of salt) with three distinct zones of clay intrusions inside the salt (13,560-13,680 ft, 14,640-14,850 ft and 15,000 to 15,300 ft) but only a trace of gypsum towards the base of salt. These constituents could be the possible cause of these localized-velocity anomalies.

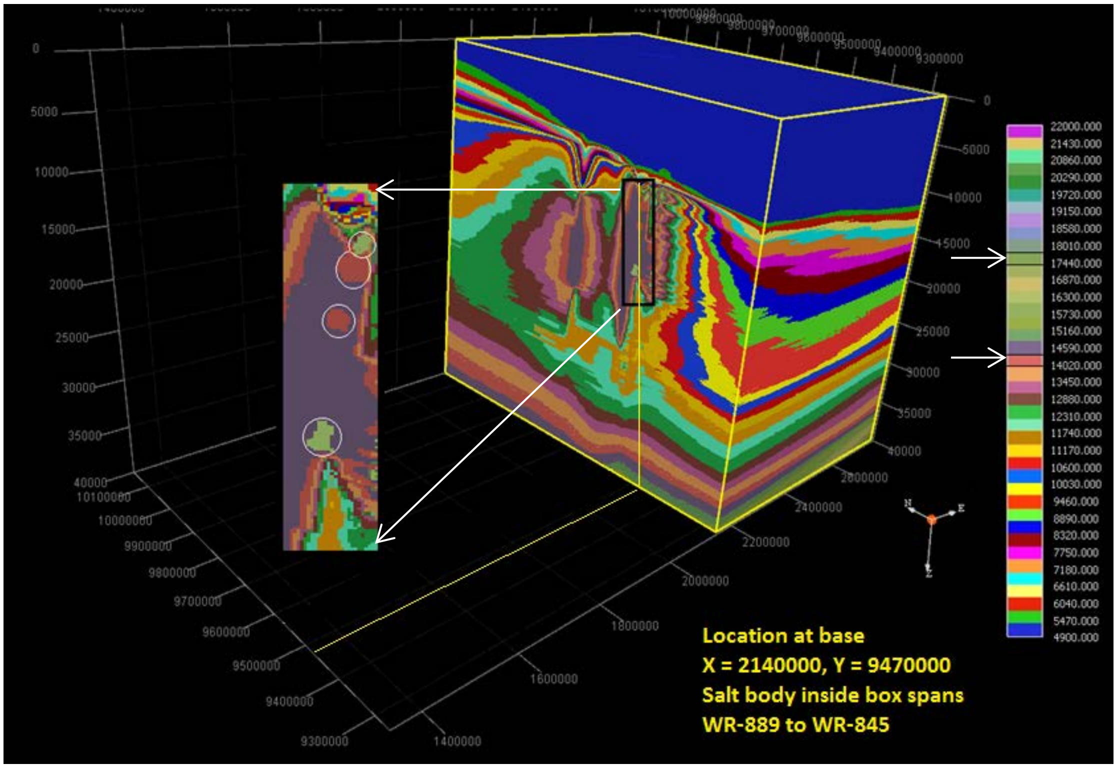

Figure 3.18. Evidence of both low- and high- velocity anomalies inside the salt.

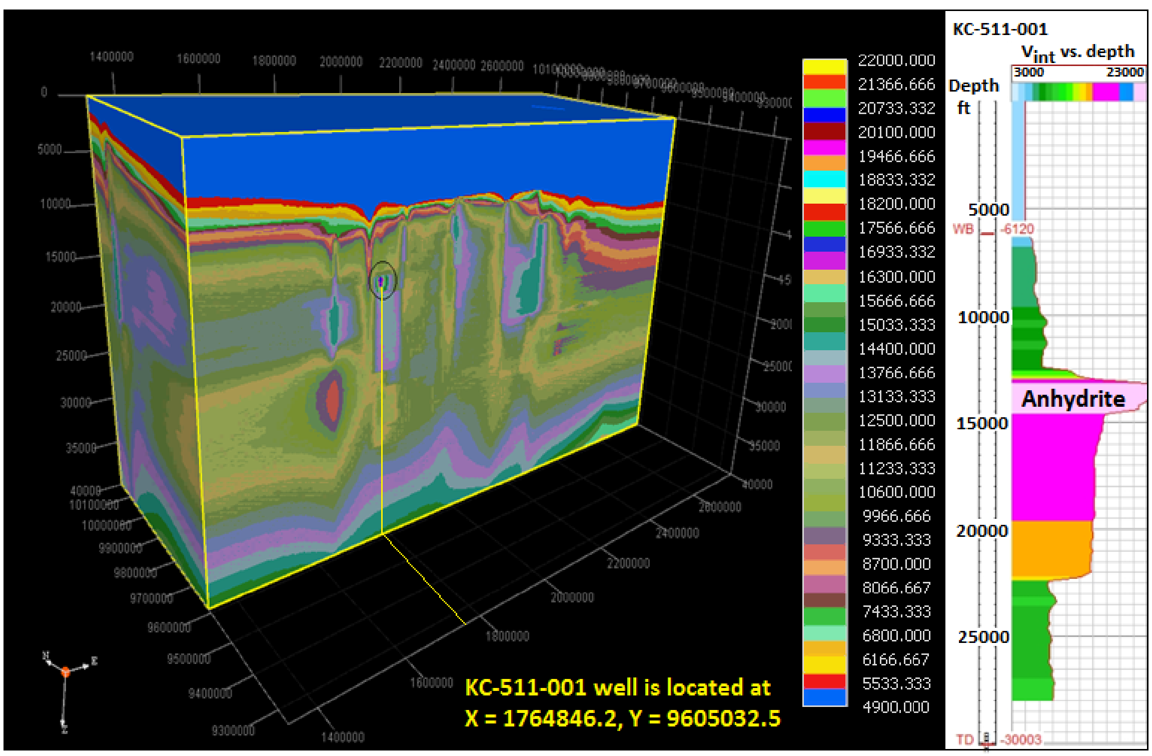

Figure 3.19. Anhydrite is visible at the top of the salt column in the Keathley Canyon well KC-511-001 both in the velocity model and in the well's V_{int} vs. depth plot.

3.6.3 Case C: Showing the presence of Cenozoic limestone either above or below salt

Cenozoic limestone of Miocene, Oligocene and Eocene ages occurs in 44 wells within the study area. It is common for all three ages to occur in most wells, but in a few wells, limestone of one or two of these ages is missing. Usually the limestone is micritic in texture, implying a shallow water back-reef lagoonal facies; and it usually occurs below salt, but above the first Wilcox Formation sands. However, in three wells, this limestone occurs above salt and may be younger in age than Miocene. I could not find relevant literature to describe these limestone formations and can only assume that since they are non-hydrocarbon bearing, they are only a geologic curiosity. Figure 3.18 shows a map of the wells in which Cenozoic limestone is present as documented in their mudlogs. Note the distribution of wells with limestone (colored blue) compared to wells without limestone. The high-velocity limestone will attract attention in the

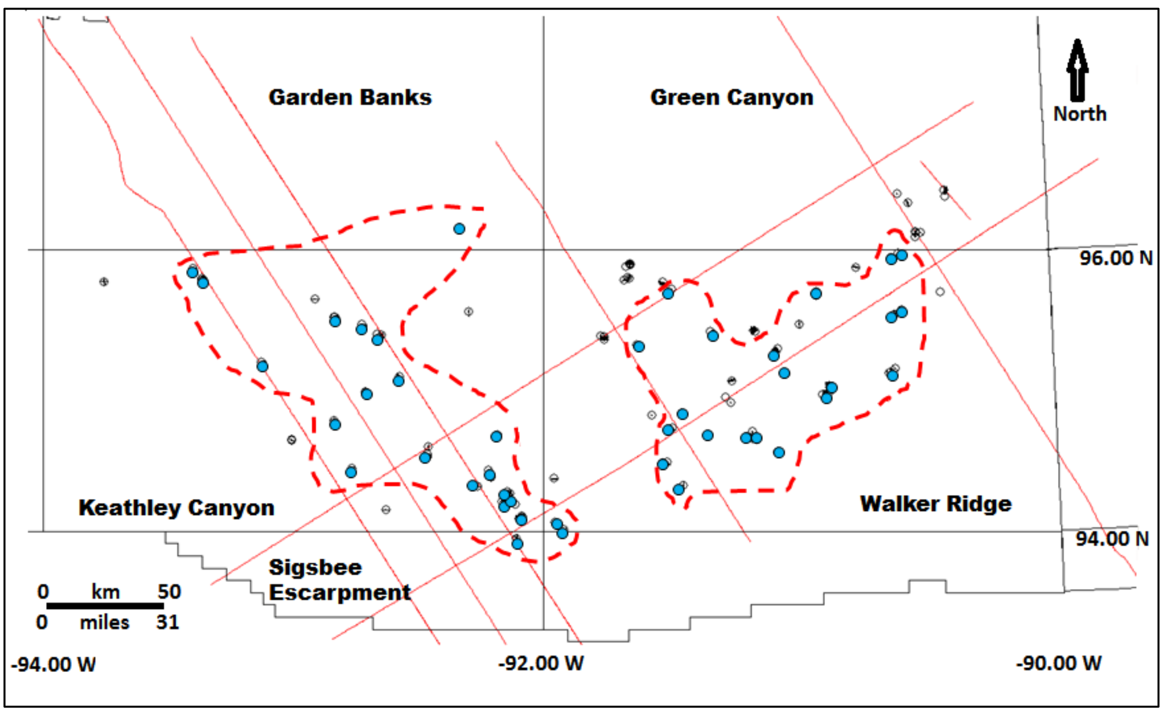

Figure 3.20. Distribution of the 44 wells in study area having at least one epoch of limestone from the three possibilities of Miocene, Oligocene and Eocene (or possibly younger in three of the wells where the limestone occurs above the salt in the well). Most wells will have all three ages in varying proportions below the salt but above the first Wilcox sand.

velocity model if it is underneath or above the salt as shown in Figure 3.19 for the Keathley Canyon well KC-785-001, if the volume fraction of limestone is 60% or greater and a minimum of 500 ft thick (sufficient to create a velocity contrast with the nearby salt). Due to the subtlety of colors, even with a 40-range color bar, it is difficult to spot this limestone feature unless you know exactly where to look for it at this scale. Modifying the scale of the colorbar might enable the ability to see other limestone deposits. There is a little over a 1000 ft of limestone in the mudlog for KC-785-001, and yet it is barely observable (the avocado green color on the colorbar separated by black lines) due to the scale of the velocity model.

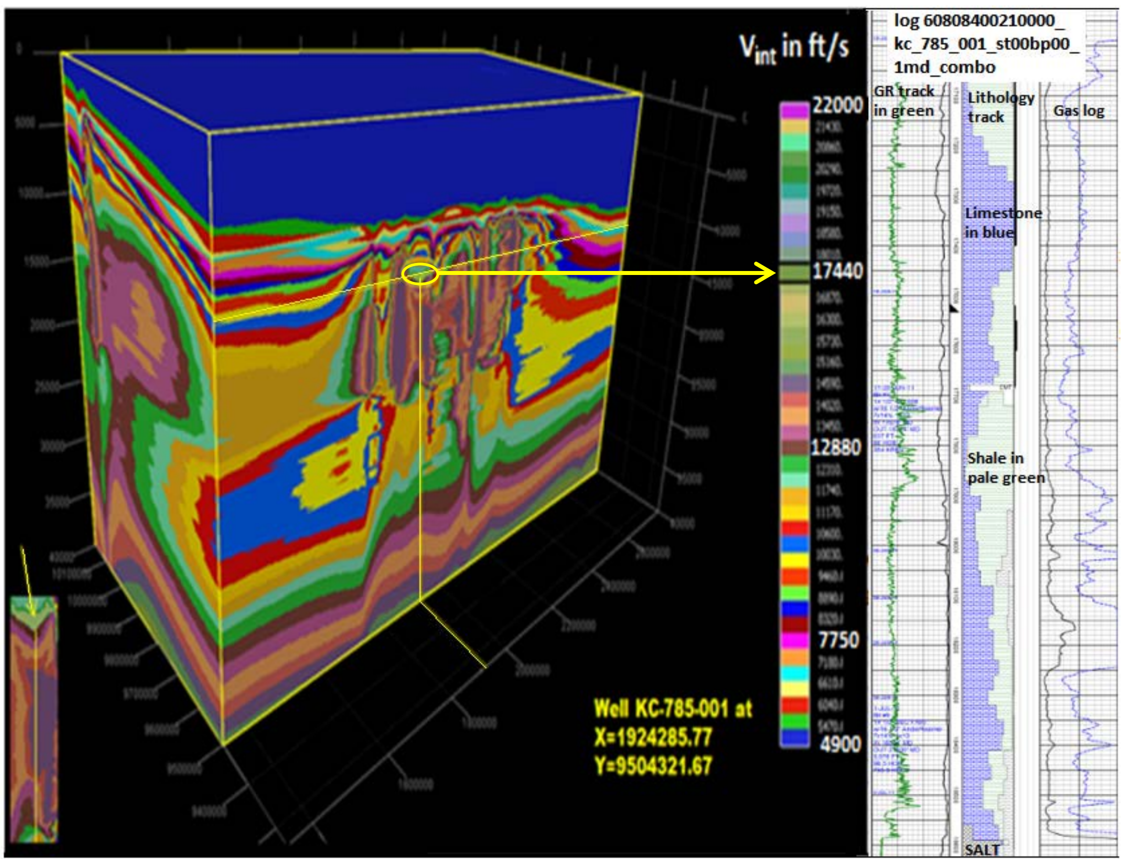

Figure 3.21. Image of a limestone deposit **above** salt inside the model at 11,000 ft depth with the corresponding mudlog from the same well showing the limestone fraction in blue in the lithology track. Interval velocity is shown to be 17,440 ft/s. Immediately below the limestone is halite. The first log track shows the GR in green, the second track is the lithology, the third track is gas chromatograph analysis in red and the fourth track is the mudlogger descriptions of the lithology.

3.7 CONCLUSIONS

The creation of this velocity model was an experiment to see what could be done without the use of 3D seismic data, which is not always available. Using high-quality 2D seismic data and all available well data within the area to build the model, this was a test as to the detail and reliability of such a velocity model. I conclude that the utility of such a regional model depends on the intended use of the model. For this study the goal was to generate a 3D velocity model to use in reprocessing the seismic data used as input; and I believe that the accuracy of this model is sufficient to do that. More importantly, the insights gained into the 3D variation of velocity throughout the deepwater GoM should be helpful to others trying to develop 3D velocity models in the same area. There is still much geology to be learned in between boreholes; but it is essential to incorporate everything one currently knows into the velocity model: the variability of salt composition, the possible presence of Cenozoic limestone, and how to create time vs. depth charts where there is missing measured velocity. This model provides a valuable starting point for illustrating basic geologic features of regional extent that may be discerned within the seismic-interval velocity volume. The model has robustly identified variations in salt interval velocities and has honored all available well data within the study area while not introducing non-geologically-meaningful velocity anomalies.

3.8 RECOMMENDATION FOR FUTURE WORK

I would like to create another 3D velocity model using the same technique but instead use a small 3D seismic survey in an area with adequate well control for direct comparison to the velocity model that was constructed with 2D seismic velocity data. It would be important to utilize an interval velocity versus depth format, the same as was utilized in the present study. The objective would be to quantify the additional resolution attained from 3D data.

3.9 REFERENCES

Cornelius, S. and Emmet, P. A., 2016, Geological 3D Velocity Model in Keathley Canyon and Walker Ridge, Gulf of Mexico, Presented at the 66th Annual Meeting, GCAGS.

Cornelius, S. and Emmet, P. A., 2016, Geological 3D Velocity Model in Keathley Canyon and Walker Ridge, Gulf of Mexico, Presented at the Fall Meeting, AGU.

Fort, X. and Brun, J.P., 2012, Kinematics of regional salt flow in the northern Gulf of Mexico, in Salt Tectonics, Sediments and Prospectivity, Geological Society of London, Special Publication 363, 265-287.

Gardner, G. H. F., Gardner, L. W., and Gregory, A. R., 1974, Formation velocity and density; the diagnostic basics for stratigraphic traps, Geophysics, **39,** 770-780.

Dutta, T., Marko, G., and Mukherjee, T., 2009, Compaction trends for shale and clean sandstone in shallow sediments, Gulf of Mexico, The Leading Edge, **28**, no. 5, 590-596.

Sandwell, D. T. and Smith, W. H. F., 2009, Global marine gravity from retracked Geosat and ERS-1 altimetry: Ridge segmentation versus spreading rate, J. Geophys. Res., **114**, B01411, 1- 18.

Sayers, C. M. and den Boer, L. D., 2011, Velocity-density relations for deepwater subsalt Gulf of Mexico shales, SEG Technical Program Expanded Abstracts, 2302-2307.